SYSTEM MODELLING AND TESTING OF A MAGNETIC SUSCEPTIBILITY DEVICE AND EFFECT OF DOWNHOLE IN-SITU TEMPERATURES ON MAGNETIC SUSCEPTIBILITY

Arfan Ali

Submitted for the
Degree of Doctor of Philosophy in
Petroleum Engineering

Heriot-Watt University
Institute of Petroleum Engineering
Edinburgh
United Kingdom

April 2009

ACADEMIC REGISTRY
Research Thesis Submission

Name*:*	Arfan Ali		
School/PGI:	Institute of Petroleum Engineering (IPE)		
Version: *(i.e. First, Resubmission, Final)*	Final	Degree Sought (Award **and** Subject area)	Ph.D

Declaration

In accordance with the appropriate regulations I hereby submit my thesis and I declare that:

1) the thesis embodies the results of my own work and has been composed by myself
2) where appropriate, I have made acknowledgement of the work of others and have made reference to work carried out in collaboration with other persons
3) the thesis is the correct version of the thesis for submission and is the same version as any electronic versions submitted*.
4) my thesis for the award referred to, deposited in the Heriot-Watt University Library, should be made available for loan or photocopying and be available via the Institutional Repository, subject to such conditions as the Librarian may require
5) I understand that as a student of the University I am required to abide by the Regulations of the University and to conform to its discipline.

* *Please note that it is the responsibility of the candidate to ensure that the correct version of the thesis is submitted.*

Signature of Candidate*:*		Date:	

Submission

Submitted By *(name in capitals):*	Arfan Ali
Signature of Individual Submitting:	
Date Submitted:	

For Completion in Academic Registry

Received in the Academic Registry by *(name in capitals):*			
Method of Submission *(Handed in to Academic Registry; posted through internal/external mail):*			
*E-thesis Submitted (**mandatory from November 2008)***			
Signature:		Date:	

Abstract

Magnetic techniques have so far been under exploited in the petroleum industry. Recently scientists have published some results on laboratory based magnetic susceptibility data for reservoir rock minerals which show strong correlations with key petrophysical parameters including permeability. However, such laboratory based experiments are not representative of in-situ reservoir conditions. Part of this thesis investigates the in-situ magnetic properties of reservoir rocks and minerals at reservoir temperatures via laboratory experiments to model downhole conditions.

The shapes of hysteresis curves at various temperatures and the shapes of temperature dependent susceptibility (TDS) curves for individual minerals (paramagnetic, diamagnetic, ferromagnetic) were used to identify the type of magnetic minerals present, their concentrations, phase transitions and changes in mineralogy. For paramagnetic minerals, magnetic susceptibility decreases with an increase in temperature, whereas diamagnetic susceptibility is shown to be independent of temperature. Ferromagnetic substances can show a variety of thermomagnetic changes depending on the type of ferromagnetic minerals present.

Changes in the domain state of ferromagnetic carriers with temperature were also observed, which either resulted from the formation of new ferromagnetic components and/or variations in grain size. Theoretical and experimental data on the thermomagnetic properties of reservoir rock minerals are also presented.

A downhole sonde capable of taking magnetic susceptibility measurements in-situ downhole has been designed and tested in this thesis. Since the laboratory based methods have demonstrated correlations between the magnetically derived mineral contents and petrophysical parameters, the downhole magnetic susceptibility sonde can potentially provide in-situ predictions of these parameters. Model boreholes were prepared in the laboratory using powder samples and by drilling through solid blocks of rock. Tests were performed on these model boreholes using the magnetic susceptibility sonde.

Dedication

To my parents Abdul Rashid and Salma Jabeen for their unfailing love; their inspirational upbringing, the sacrifices rendered to provide me with all the facilities and comfort for completing my studies up to this end.

Acknowledgements

First and foremost, I would like to thank Dr. Mark Hounslow and Dr. Shiyi Zheng for taking their time to exam my thesis and providing me with a valuable feedback.

I sincerely thank to my supervisor and colleague Professor David K. Potter for his invaluable guidance, motivation and encouragement throughout the course of this research. I really loved my time working for him since I joined Heriot-Watt in 2005, and I seriously think that we are like minded in many aspects.

I thank Scottish Enterprise for providing funds to accomplish a part of this research. I thank Heriot-Watt University library for the use of their collections. Without them, this research would have been most difficult. I also thank Alastair Housten for his assistance during visits to the electronics department (HWU) for giving me space to work in their labs and also providing me technical assistance.

I thank various oil and gas companies for the use of their reservoir samples. I thank Denis Mclaughlin for helping in preparing the downhole models of the borehole and in other bits and pieces from time to time. I also thank computer support staff for their support in installing necessary software into my PC for running the prototype downhole sonde.

I thank Dr. Oleksander Ivakhnenko for providing me a number of reservoir rock samples and in exchanging technical ideas especially in carrying out hysteresis measurements. I also thank the staff in the Department of Earth and Environmental Science of the Ludwig-Maximilian University in Munich, Germany for letting me use the Variable Field Translation Balance (VFTB).

I thank Dr. Jim Somerville for providing me information on various sandstone samples used in this thesis. I also thank Professor Patrick Corbett for providing necessary support in obtaining my Royal Society of Edinburgh (RSE) fellowship award. This helped me financially to continue working on this thesis. I am also grateful to my office colleagues Masoud Riazi and Ali Reza for sharing research related ideas.

Special thanks to my beloved brothers ‘Asad and Ali’ who have been a continuous source of inspiration in every aspect of my life. Finally, I would like to thank my wife Maleeha for her invaluable support towards the end of this thesis. She has been very considerate since I could not give her much time after marriage.

Contents

List of Tables

List of Figures

List of Illustrations

List of Abbreviations

AC	Alternating Current
AMS	Anisotropy of Magnetic Susceptibility
^{o}C	Degree Celsius
DAC	Digital-to-Analog Converter
DAQ	Data Acquisition System
DC	Direct Current
EM	Electromagnetic
F.W.H.M	Full Width Half Maximum
H	Magnetic Field Strength
Hc	Coercivity of Magnetisation (Coercive Force)
Hcr	Coercivity of Remanent Magnetisation
HPHT	High Pressure High Temperature
IC	Integrated Circuit
I/O	Input-Output
IRM	Isothermal Remanent Magnetisation
K	Kelvin, Potassium
LED	Light Emitting Diode
LTO	Low Temperature Oxidation
M	Magnetisation
MD	Multi-Domain
Mrs	Saturation Remanent Magnetisation
Ms	Saturation Magnetisation
Msp	Spontaneous Magnetisation
NI	National Instruments
NRM	Natural Remanent Magnetisation
PCB	Printed Circuit Board
ppm	Parts Per Million
PSD	Pseudo-Single Domain
SD	Single-Domain
SEM	Scanning Electron Microscope
SI	Systems International
SIRM	Saturation Isothermal Remanent Magnetisation
SNR	Signal to Noise Ratio

SP	Super-Paramagnetic
Tc	Curie Temperature
TDS	Temperature Dependent Susceptibility
T_N	Néel Temperature
USB	Universal Serial Bus
VFTB	Variable Field Translation Balance
XRD	X-ray Diffraction
χ, MS	Magnetic Susceptibility
χ_m, χ	Mass Magnetic Susceptibility
χ_v, κ	Volume (bulk) Magnetic Susceptibility
χ_o	Initial Magnetic Susceptibility
χ_{Hfld}, H_{fld} MS	High Field Magnetic Susceptibility
χ_{Lfld}, L_{fld} MS	Low Field Magnetic Susceptibility
χ_{ferro}	Ferromagnetic Susceptibility
χ_{dia}	Diamagnetic Susceptibility
χ_{para}	Paramagnetic Susceptibility
χ_M	Molar Magnetic Susceptibility
μT	Micro-Tesla
θ	paramagnetic Curie temperature
μ_r	Relative Permeability of the Specimen
μ_0	Permeability of Free Space
φ	Magnetic Flux
B	Magnetic Flux Density
$\Re$	Reluctance of the Magnetic Circuit

Chapter 1
Introduction

In all worldwide petroleum basins, shaley sand analysis has always challenged geologists, engineers and petrophysicists. The main challenge is to identify from cores or logs the degree to which the clay minerals affect the reservoir quality which is an important factor in determining the reservoir pay zones. For example, illite is an important clay mineral particularly with respect to studies of fluid flow. Small increases in its occurrence can dramatically affect the permeability and microporosity of a sample by bridging pore space and creating microporous rims. A 1-2 % increase in the content of authigenic illite can cause a decrease in permeability of about 2-3 orders of magnitude without significantly affecting the porosity (Ivakhnenko and Potter, 2006). Even though a reservoir rock looks solid to the naked eye, a microscopic examination reveals the existence of tiny openings in the rock which may help the fluid flow (Leonardon, 1961). It is possible to have a very high porosity without any permeability at all, as in the case of compacted shales. The reverse of high permeability with a low porosity might also be true, e.g., in microfractured carbonates. Therefore it is imperative to know the types of clay minerals and their relative percentages in the reservoir rock matrix.

The petrophysics group at the Institute of Petroleum Engineering Heriot-Watt University has shown strong correlations between laboratory based magnetic susceptibility data of reservoir rock minerals with key petrophysical parameters including permeability (Potter, 2005). Therefore, it will be extremely useful to develop a downhole magnetic susceptibility logging sonde which can predict the magnetic behaviour of most common reservoir clay minerals at in-situ conditions. The magnetic signal obtained downhole can then be used as an indirect indicator of fluid permeability. The testing of the downhole magnetic susceptibility sonde and modeling the magnetic behaviour of clay minerals at reservoir conditions has been the main subject of this thesis.

1.1 Importance of clay minerals in petroleum industry and their effect on various logging tools

Most of the shaley sand evaluation methods require knowledge of the amount of shales or clays present in the formation material and how they affect the measurements of various logging tools. Over the years the term ‘clays’ and ‘shales’ have been used interchangeably not because of the lack of understanding but due to different ways in which properties are measured. Clays are defined in terms of both particle size and mineralogy. In terms of size, clays refer to particle diameter sizes less than 2.4mm. Clays are often found in sandstones, siltstones, and conglomerates. The most common types of clay minerals found in sedimentary rocks are kaolinite, chlorite, illite and smectite. The scanning electron microscope (SEM) image of these four clay types is shown in Figure 1.1 (Syngaevsky, 2000). The major effects of clays in a hydrocarbon reservoir are: 1) reduction of effective porosity and permeability; 2) migration of fines whenever clay minerals turn loose; migrate and plug the pore throats that cause further reduction in permeability; 3) water sensitivity whenever clays start to hydrate and swell after contact with water (or mud filtrate) which in turn causes reduction in effective porosity and permeability; 4) acid sensitivity-whenever acid reacts with iron-bearing clays to form a gelatinous precipitate that clogs pore throat and reduce permeability.

Shales are a mixture of clay minerals and other fine grained particles deposited in very low energy environments. They can be distributed in sandstone reservoirs in three possible ways; (1) laminar shale, where shale can exist in the form of laminae between layers of clean sand; (2) structural shale, where shale can exist as grains or nodules within the formation matrix; and (3) dispersed shale, where shale can be dispersed throughout the sand, partially filling the intergranular interstices, or can be coating the sand grains. All these forms can occur simultaneously in the same formation. Each form can affect the amount of rock porosity by creating a layer of closely bound surface water on the shale particle.

The presence of clay minerals or shale affects the responses of the majority of logging tools. For example, they can generally cause a higher reading of apparent porosity indicated by density, neutron and sonic tools and a suppressed reading by resistivity tools. This is because in density tools, the presence of clay minerals lowers the apparent density, and this causes an increase in the apparent porosity of the tool. Also, there is a limitation of tool calibration whenever clay minerals are present. In neutron tools, the

higher concentration of hydrogen ions in clays translate to a higher calculated porosity; whereas in sonic tools, the interval transit time of clays is high which corresponds to a higher porosity. In electric logs, the clay minerals, because of their large surface area, absorb a large quantity of reservoir's pore water to their surface. This bound water contributes to additional electrical conductivity hence lowering the resistivity. Table 1.1 shows a list of various logging tools, their method of operation, and how their performance is affected by the presence of clay minerals.

1.2 Clay magnetism and its significance in reservoir characterization

The major constituents of many sedimentary rocks, usually quartz in sandstones or calcite in carbonates are represented by a low and negative magnetic susceptibility. I will explain the magnetic susceptibility term in Section 2.6 **Chapter 2**. On the other hand, permeability controlled by clays like illite is represented by a low and positive magnetic susceptibility. Therefore by simply looking at the magnetic susceptibility signal (positive or negative), one can tell whether there are paramagnetic clay minerals present in the reservoir rock.

And this is certainly a good guide to explaining the relative magnitudes of susceptibilities in samples of pure minerals. However, it is uncommon for a natural sample to contain only one category of magnetic minerals. For instance, the presence of iron bearing minerals also gives a high and positive magnetic susceptibility. It is therefore necessary to consider virtually all samples as a mixture of minerals often falling into two or three categories of magnetic behaviour and each having a different magnetic susceptibility value. The idea of interpreting each measurement in terms of many different minerals sounds a fairly daunting task. But in practice we can simplify matters by making some assumptions about which minerals are significant in a sample. Samples which are not contaminated by ferrous metal do not usually contain iron bearing minerals. In their absence, the susceptibility of a sample is most likely to be controlled by other paramagnetic/diamagnetic minerals.

1.3 Various magnetic techniques used in hydrocarbon industry and the magnetic susceptibility sonde

Historically the development of magnetic studies for hydrocarbon application was restricted to magnetic prospecting (Donovan et al., 1979) and petrophysical investigations for the detection of oil and gas reservoirs (Bagin et al., 1973, Bagin and

Malumyan, 1976). Magnetic techniques utilizing the Earth's magnetic field or the natural remanent magnetisation (NRM) in the reservoir rocks also played a prominent role in petroleum reservoir exploration and research. High resolution magnetic surveys (Eventov, 1997, 2000) utilize the present Earth's magnetic field. Such survey tools measure three orthogonal components of the local magnetic fields, and from these data the tool's inclination, azimuth, and toolface orientation can be calculated. Also, boreholes are commonly surveyed for drilling using the Earth's magnetic field as a north reference (Wilson and Brooks, 2001).

Palaeomagnetism together with standard magnetostratigraphy is starting to be used for correlation purposes in the petroleum industry (Gillen et al., 1999: Cioppa et al., 2001; Filippycheva et al., 2001). NRM in palaeomagnetism is a key parameter for the orientation of directional properties to geographic coordinates (Hailwood and Ding, 1995), and helping to date hydrocarbons (Symons et al., 1999). Environmental magnetism is also an important discipline for the detection of hydrocarbon seepage (Yeremin et al., 1986; Liu et al., 1996; Costanzo-Alvarez et al., 2000) and contamination (Cogoini, 1998).

A variety of techniques have been used in the past to measure the magnetic properties of minerals including: fractionation with a magnetic separator (Stradling, 1991), Frantz isodynamic separator (Nesset and Finch, 1980 and McAndrew, 1957), magnetometer (Foner and McNiff, 1968 and Lewis and Foner, 1976), SQUID (Sepulveda et al., 1994), resonant coil (Cooke and De Sa, 1981 and Isokangas, 1996) and the inductance bridge (Drobace and Maronic, 1999, Stephenson and De Sa, 1970, Foner, 1991 and Tarling and Hrouda, 1993). These techniques are generally considered laboratory methods due to the length of time required to process the samples.

The developments in instrumentation and software with time, have attracted a number of scientists towards the application of magnetic susceptibility methods in the hydrocarbon industry. They include magnetic susceptibility studies and its integration with magnetometer and other surface geophysical surveys, and with soil magnetic studies accomplished in the laboratory. However, some still think that there will be insufficient contrast in the magnetic susceptibility of sand and gravel compared to clays and other sedimentary rocks in order to differentiate those (Jeffrey et al 2007).

The development of industrial grade equipment to measure magnetic susceptibility was identified by the Julius Kruttschnitt Mineral Research Centre (JKMRC). This equipment is able to measure complex magnetic susceptibility (i.e. both phase and amplitude of the magnetic susceptibility vector) from 10 Hz to 100 kHz at infinitely adjustable field strengths (Cavanough and Holtham, 2001 and Cavanough and Holtham, 2004). The CS-2 and KLY-2 Kappabridge was used for the measurement of thermal changes of magnetic susceptibility in weakly magnetic rocks (Hrouda, 1994). Low field variation of magnetic susceptibility was used to see its effect on anisotropy of magnetic susceptibility (AMS) (Hrouda, 2002). Magnetic susceptibility and AMS together with the intensity, inclination and declination of the natural remanent magnetisation have formed the basis of high resolution rock magnetic analyses (Hall and Evans, 1995; Liu and Liu, 1999; Robin et al., 2000).

At present certain magnetic methods are becoming more recognised and applied within the petroleum industry, in particular using magnetic susceptibility measurements to predict petrophysical properties such as clay content and permeability (Potter, 2004a; Potter 2004b; Potter et al, 2004; Potter, 2005; Potter, 2007; Ivakhnenko and Potter, 2008; Potter and Ivakhnenko, 2008). However, all these methods are laboratory based and the downhole magnetic susceptibility measurements remain a relatively unexploited tool. There are no commercially available downhole magnetic susceptibility logging tools for industry diameter boreholes, as these measurements are not currently part of oil and gas industry wireline logging or measurements while drilling operations.

Therefore one of the aims of this thesis is to build a prototype magnetic susceptibility sonde capable of measuring the magnetic susceptibility of the formation downhole. The new sonde will be a modernized version of the existing electromagnetic (EM) well-logging tools. The EM tools refer to the process of acquiring information of the earth formation properties (mainly resistivity/conductivity) by taking into account the effect of eddy currents (Liu et al, 1989). In practice, the conductivity signal measured by the EM tools is also affected by the magnetic susceptibility of the formation material (Fraser, 1973). The influence of magnetic susceptibility on EM data has long been known, but very little has been done about its importance towards oil and gas explorations. In most cases magnetic susceptibility has been treated as a source of contamination in the conductivity signal and people have been trying very hard to eliminate that contamination by various techniques. In doing so, useful information

about the magnetic susceptibility is wasted and also the recovered conductivity models become less reliable. The magnetic susceptibility sonde in this thesis will suppress the conductivity signal with the help of various electronic modules such that the susceptibility signal will overshadow the conductivity signal.

1.4 Research Objectives

This dissertation has three main objectives. The first objective is the system modeling and testing of a demonstration version of the downhole sonde capable of taking raw magnetic susceptibility measurements in-situ conditions. This includes the susceptibility contributions from all the reservoir rock minerals which are present within the vicinity of the sensor coil in the sonde. The susceptibility signal will potentially aid in the interpretation of the main lithological zonations inside the borehole at high resolution. Since the petrophysics research group at HW University has demonstrated correlations between the magnetically derived mineral contents and petrophysical parameters (permeability, the cation exchange capacity per unit pore volume, and the flow zone indicator), the downhole magnetic susceptibility signal can potentially provide in-situ predictions of these parameters. The cut-offs between the different lithologies could be quantitatively more accurate than the gamma ray tool due to the higher potential resolution of the magnetic sonde. The proposed sonde would operate at oil or gas reservoir temperatures (up to at least 110° C) and pressures of around 6000 – 10000 psi (about 40 – 70 MPa). This would make downhole in-situ measurements of magnetic susceptibility as part of a wireline logging string. Possibly, it may also be incorporated in another form of downhole measurements, these being measurements while drilling (MWD).

The second objective of this dissertation is to create some model boreholes in the laboratory and to test the working of the prototype downhole sonde on these boreholes at normal conditions of temperature and pressure. The heterogeneous boreholes will contain layers of relatively clean sand, confined and dispersed clay, and some shaley material. The prototype magnetic susceptibility sonde should be able to pick up bed boundaries and to distinguish various types of layers based on their magnetic susceptibility values.

The third objective is to study the temperature dependence of magnetic susceptibility on reservoir rocks, in order to determine magnetic susceptibilities at reservoir conditions.

Thermomagnetic analyses on a number of reservoir samples is carried out (to model the in-situ conditions for the downhole sonde) to investigate the effect of increase in temperature on their low and high field magnetic susceptibilities, hysteresis parameters, domain state etc. This would help to model the effect on the output of downhole susceptibility sonde at in-situ conditions.

1.5 Organization of the Dissertation

Chapter 1 is the introductory chapter emphasizing how shaley/clay rich formations give rise to a higher magnetic susceptibility signal than clean formations. It briefly explains how shaley formations affect the performance of various logging tools and the importance of magnetic susceptibility data which is obtained as a byproduct from the conductivity tool. It also briefly outlines previous work on various magnetic techniques in the petroleum industry.

Chapter 2 describes general aspects of rock and mineral magnetism. It outlines various classes of clay minerals in terms of their magnetic behaviour. The magnetic properties like domain states and magnetic hysteresis are explained in terms of mineral grain size and magnetic phase. The main challenge in this chapter is to identify the degree to which the clay minerals affect the susceptibility signal. For this, I have compiled and presented in tabular form the magnetic susceptibility data for a range of minerals/materials from existing literature. Towards the end of this chapter, thermomagnetic analysis of the magnetic susceptibility signal is explained which forms the basis of **Chapter 5**.

Chapter 3 explains the step by step procedure for the design and modeling of the prototype magnetic susceptibility sonde system. This includes the design of the electronic circuit, coil system, the housing to hold the printed circuit board (PCB) and the coils, and the shielding system to protect the sonde from the borehole environment. This chapter also explains a detailed mathematical analysis of the sonde operation, output data formats, and the type of wireline used.

Chapter 4 explains the performance of the sonde system as a whole. It involves interaction among the sonde, various electronic modules, and the personal computer. It also demonstrates how the connections are carried out between the sonde and the data acquisition system (DAQ). The experimental setup on initial testing of the magnetic

susceptibility sonde, and the transfer and processing of the susceptibility data using LABVIEW software is also explained in this chapter.

Chapter 5 describes laboratory based thermomangetic analyses on a number of different reservoir rock samples (shoreface, shallow marine (high pressure high temperature), and turbidite). In particular, the effect of variation in grain size and magnetic mineralogy is analysed with respect to variation in temperature. Hysteresis parameters are shown to be a powerful tool for identifying multiple domain states and changes in mineralogy in a reservoir rock sample. I have used the variations of magnetic susceptibility with temperature to model the in-situ reservoir conditions. I have also performed temperature dependent susceptibility (TDS) measurements to quantify mineralogy.

The main conclusions drawn from the different sections of this thesis are reported in **Chapter 6**. All innovative aspects of the thesis and recommendations for further work are also summarised in this chapter.

Tool	Designation	Measurement	Applications	Limitations	Effect of Clays on Tool Performance
Induction logging: Dual induction	DIL	Formation resistivity in oil-based muds or air-drilled boreholes.	Determine Sw, can be used in oil based or fresh water muds. Focused to minimize the influence of the borehole.	Difficult to calibrate, lower vertical resolution, not ideal for mapping confined fractures.	Clays cause an increase in magnetic susceptibility signal which is superimposed on the conductivity signal and so tool gives a higher output.
Gamma ray	GR	Records naturally occurring gamma radiations from the formation.	Detection of radioactive minerals, estimate shale in dirty sands, shale vs. non-shale and shale content.	Not very suitable for well to well correlations and also in KCL based drilling muds.	Presence of clays causes a higher output signal from the gamma ray tool.
Sonic: Borehole compensated Long spaced sonic	BHC LSS	Measures the transit time of acoustic waves through the formation rock.	Detection of fractures, lithology, and porosity prediction.	May cause problems when tool is run at shallower depths for large diameter boreholes, doesn't detect secondary porosity.	The transit time of clays is higher. The tool gives a higher value of apparent porosity.
Compensated neutron log	CNL	Impact of neutrons on H atoms within the formation.	Determination of porosity, correlation, lithology and gas detection.	Cannot be used in gas-filled boreholes.	High concentration of hydrogen ion in clays translate to a higher calculated porosity. The tool is sensitive to shales which contain boron/rare-earth elements with a high thermal neutron capture.

Normal resistivity logs: Short normal Long normal Lateral	 SN LN LAT	Formation resistivity.	Determine Sw, porosity, severe invasion effect.	Cannot be used in non-conductive muds.	Bound water in clays reduces the resistivity signal.
Density: Compensated formation density Litho-Density tool	 FDC LDT	Impact of gamma rays on electrons in the formation.	Measurement of porosity, bulk density, seismic velocity, identification of minerals in complex lithology, nature of fluid in pores, gas detection.	Borehole size correction is required.	Clay has lower density (higher apparent porosity) than quartz.
Spontaneous potential	SP	Measures naturally occurring potentials in the well bore as a function of depth.	Detection of permeable zones, determination of formation water salinity and bed thicknesses.	Cannot be used in non-conductive or oil-based muds.	Bound water in clays contributes to additional electrical conductivity or lower resistivity.
Microresistivity logs: Microlaterolog Proximity log	 MLL PL	Resistivity of the invaded/flushed zone.	Determine Sw, identify permeable formations, can be used to correct deep resistivity measurements.	Quantitative inference of permeability is not possible, poor if thick mudcake, poor if shallow invasion.	Bound water in clays reduces the resistivity signal.

Table 1.1: Effect of clays on downhole logging tools used in hydrocarbon exploration

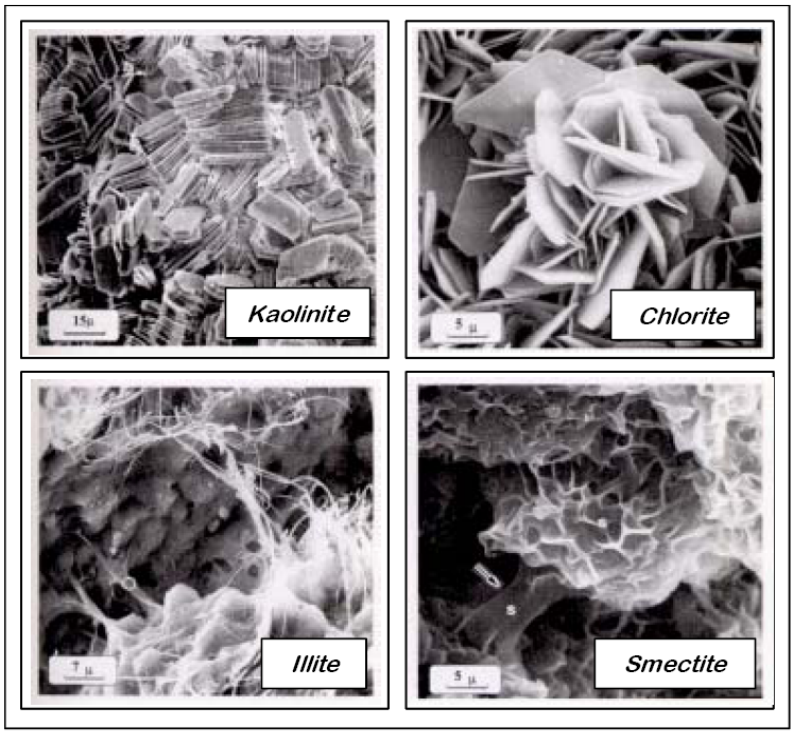

Figure 1.1: SEM image of four types of clay minerals commonly found in reservoir rocks (after Syngaevsky, 2000)

Chapter 2

Introduction to Magnetic Susceptibility of Rocks and Minerals Found in Hydrocarbon Reservoirs

2.1 Brief synopsis

This chapter provides an overview of the main magnetic properties of rocks and minerals found in hydrocarbon reservoirs and also highlights the advantages of measuring their magnetic susceptibility signal. It describes the laboratory based method for measuring the magnetic susceptibility of reservoir rocks at various temperatures and the importance of susceptibility versus temperature curves in characterizing the reservoir rock matrix. The description will lay the basis for the importance of the magnetic susceptibility sonde designed in **Chapter 3** and the thermomagnetic analysis of magnetic susceptibility explained in **Chapter 5** of this thesis. To understand the importance of magnetic susceptibility, the magnetic properties and main magnetic classes of reservoir rocks and minerals are described in relation to their applicability to the petroleum industry. The magnetic analyses covered in this chapter include magnetic susceptibility, magnetic hysteresis, and thermomagnetic measurements.

2.2 Classes of clay minerals based on their magnetic behaviour

A mineral or material is classified as magnetic if it gives rise to magnetic induction in the presence of a magnetic field. The magnetization (M) of the material is related to the applied field strength (H) by the equation

$$M = \chi H \tag{2.1}$$

where χ is the magnetic susceptibility of the material. It is a dimensionless quantity which expresses the ease with which a substance may be magnetized. Magnetic susceptibility is a very important physical parameter in exploration geophysics, and information about its distributions can be used to determine subsurface structures, and to detect mineral deposits and other natural resources. All substances universally exhibit magnetic susceptibility at temperatures above absolute zero (Tarling and Hrouda, 1993).

Magnetic susceptibility data for minerals present in sediments has been reported by a number of authors (Foex et al., 1957; Mullins, 1977; Collinson, 1983; Hunt et al., 1995, Matteson et al., 2000) although the data is by no means comprehensive. The most extensive single literature source is Hunt at al. (1995). Another useful source of relative and indirect magnetic susceptibility values is given by Rosenblum and Brownfield (1999). I therefore collected, and recalculated where necessary, all available literature data of magnetic susceptibility for relevant sediment minerals, and these values are given in Tables 2.1 and 2.2. The data shows that all minerals can be classified in terms of their magnetic behaviour falling into one of the five categories: diamagnetism, paramagnetism, ferromagnetism, ferrimagnetism and antiferromagnetism.

2.2.1 Diamagnetism

Diamagnetism is shown by the materials whose outermost shells are completely filled with electrons. On the application of an external magnetic field, the spin of the electrons and/or their orbital angular momentum changes. This makes the electrons to precess and oppose the external applied field. In other words, diamagnetic materials cause a reduction in the strength of the external applied field, the reason diamagnetic materials show negative magnetic susceptibilities. Diamagnetic susceptibility is usually very weak and only those atoms with completely filled orbits show diamagnetic effect (Butler, 1992). The susceptibility of a diamagnetic material is given by the equation (Spaldin, 2003),

$$\chi = -\frac{N\mu_0 Ze^2}{6m_e}(r^2)_{av.} \qquad (2.2)$$

where N is the number of atoms per unit volume, μ_0 is the permeability of free space (a free atom is considered), r is the orbital radius of the electrons, Z is the total number of electrons, e is the charge and m_e is the mass of electron. Also note from the equation that the susceptibility 'χ' is dimensionless and also negative and that there is no explicit temperature dependence. However, the amount of magnetization is proportional to $(r^2)_{av}$, which is very weakly temperature dependent.

The plot of magnetization (M) versus applied field (H) gives the curve shown in Figure 2.1a. Pure quartz, calcite and feldspar are examples of diamagnetic minerals and are characterized by having negative magnetic susceptibilities, in the order of -10^{-6} SI in

terms of volume susceptibility (Hrouda, 1973; and Borradaile et al., 1987 as reported by Borradaile, 1988). However, these minerals are rarely pure, as they commonly contain non-diamagnetic inclusions.

Since diamagnetic materials show negative magnetic susceptibilities whereas paramagnetic materials show positive magnetic susceptibilities, the alloys of diamagnetic and paramagnetic materials can be used in delicate magnetic measurements (Spaldin, 2003). This is due to the fact that a particular composition of diamagnetic and paramagnetic minerals can be used to have net zero magnetic susceptibility at a particular temperature.

2.2.2 Paramagnetism

In this class of materials, the atoms or ions have a net magnetic moment due to unpaired electrons in their partially filled orbits. However, the individual magnetic moments do not interact magnetically (Figure 2.1b). In transition metal salts, the cations have partially filled d shells, and the anions cause separation between cations. This weakens the magnetic moments on neighboring cations (Spaldin, 2003). The Langevin model states that each atom has a magnetic moment which is randomly oriented as a result of thermal energies (Langevin, 1905). Therefore in zero applied magnetic field, the magnetic moments point in random directions. When a field is applied, a partial alignment of the atomic magnetic moments in the direction of the field results in a net positive magnetization and positive susceptibility (Tarling, 1983). At low fields, the flux density within a paramagnetic material is directly proportional to the applied field, so the susceptibility $\chi = M/H$ is approximately constant. Unless the temperature is very low (<<100 K) or the field is very high, paramagnetic susceptibility is independent of the applied field (Moskowitz, 1991).

Most iron bearing carbonates and silicates are paramagnetic. Many salts of transition elements are also paramagnetic. At normal temperatures and in moderate fields, the paramagnetic susceptibility is small. However the strength of paramagnetic susceptibility depends on the concentration of paramagnetic minerals present in the sample. In most cases, it is larger than the diamagnetic susceptibility contribution. In samples containing ferromagnetic/ferrimagnetic minerals, the paramagnetic susceptibility contribution can only be significant if the concentration of ferromagnetic/ferrimagnetic minerals is very small. In this case, a paramagnetic

correction may be needed. For common paramagnetic rock forming minerals, the paramagnetic susceptibility generally ranges between 10-2 to 10-4 SI vol. (Dunlop and ozdemir, 1997).

2.2.3 Ferromagnetism

The atomic magnetic moments in ferromagnetic materials exhibit very strong interactions resulting in a parallel or antiparallel alignment of their magnetic moments. This produces a strong magnetization even in the absence of an applied magnetic field (Figure 2.1c). In 1907, Weiss postulated this effect by the presence of a molecular field within the ferromagnetic material. He suggested that magnetic materials consists of small regions called magnetic domains within which all the atomic magnetic moments are aligned in the same direction (domain saturation magnetisation). On the application of an external applied field, the response of these magnetic domains to the applied field determines the magnetic susceptibility of the material (Petty, 2007).

In quantum mechanics, the Heisenberg model of ferromagnetism describes the parallel alignment of magnetic moments in terms of an exchange interaction between neighboring moments (Kennedy, 1985). As opposed to paramagnetic materials, the magnetization in ferromagnetic materials is saturated in moderate magnetic fields and at high temperatures. Therefore, ferromagnetic materials are usually compared in terms of saturation magnetization (magnetization when all domains are aligned) rather than susceptibility.

There are numerous ferromagnetic materials present in reservoir rocks and the Fe-Ti oxides form the majority of them by far. Other mineral groups or minerals exhibiting ferromagnetic properties include goethite (an iron oxyhydroxide), pyrrhotite, greigite (iron sulphides), and hydrated iron sulphate which results from the hydration of pyrite and marcasite (a relatively unstable minerals when exposed to air). All these minerals have characteristically high magnetic susceptibilities (greater than paramagnetic minerals) ranging anywhere from 10^{-3} SI vol. to 100 SI vol. (Carmichael, 1982 as reported by Borradaile, 1988).

As ferromagnetic materials are heated, the thermal agitation of the atoms implies that the degree of alignment of the atomic magnetic moments decreases and hence the saturation magnetization also decreases. Eventually the thermal agitation becomes so

great that the material becomes paramagnetic. The temperature of this transition is called the Curie temperature, T_c (for iron Fe: T_c =770 °C, for cobalt Co: T_c =1131 °C and for nickel Ni: T_c =358 °C). Above the Curie temperature, the susceptibility varies according to the Curie-Weiss law. The temperature dependence of magnetic susceptibility for various types of reservoir minerals is explained in Section 2.6.2.

2.2.4 Ferrimagnetism

Ferrimagnetism is only observed in compounds, which have more complex crystal structures than pure elements. The exchange interactions enable the parallel alignment of atomic magnetic moments in some parts of the crystal and anti-parallel alignment in others (Figure 2.1d). These break down the material into magnetic domains (see Section 2.4 for detailed explanation of magnetic domains). Ferrimagnetic materials are very similar to ferromagnetic materials in terms of spontaneous magnetization, Curie temperatures, coercivity, hysteresis and remanence. After the applied magnetic field is removed ferromagnetic and ferrimagnetic materials acquire and retain remanent magnetisation. Magnetite is an example of a ferrimagnetic material.

2.2.5 Antiferromagnetism

In antiferromagnetic materials, the exchange interactions causes the antiparallel alignment of the atomic magnetic moments (Figure 2.1e). This is in contrast with ferromagnetic materials where the atomic magnetic moments are aligned in parallel. If the magnitude of atomic magnetic moments is equal and they are completely opposite in direction, this will result in a net zero spontaneous magnetization and the material is a perfectly compensated antiferromagnetic. Such materials have zero remanence, no hysteresis, and a small positive susceptibility that varies in a peculiar way with temperature. Ilmenite is such an example (O'Reilly, 1984).

If the cancelling of the magnetic moments is not complete a small net moment is observed and the system is described as imperfect antiferromagnetism. This imbalance can have a number of possible origins such as lattice defects, crystal impurities or the spin-canting when the cation-anion-cation exchange bonds are slightly tilted ($< 1^o$) or canted. Canted antiferromagnetism exhibit the typical magnetic characteristics of ferromagnetic and ferrimagnetic materials. Hematite is an example of a canted antiferromagnetic mineral (Dunlop and Ozdemir, 1997).

Unlike ferromagnetic materials which show paramagnetic behaviour above their Curie temperature, the antiferromagnetic materials show paramagnetic behaviour above Néel temperature (T_N). The paramagnetic behavoiur is indicated with a negative intercept indicating negative exchange interactions (Moskowitz, 1991). In the periodic table the only element exhibiting antiferromagnetism at room temperature is chromium (T_N =37 ºC).

For convenience in the text I will often use the term ferromagnetic to describe ferromagnetic, ferrimagnetic and canted antiferromagnetic substances in this thesis.

2.3 Common minerals found in hydrocarbon reservoir sediments

The most common clay minerals and compounds relevant for petroleum reservoirs and their initial mass magnetic susceptibilities are shown in Tables 2.1 and 2.2. The main clays are chlorite, illite (paramagnetic), kaolinite (diamagnetic) etc. While ferromagnetic minerals (magnetite, titanomagnetite, maghemite, pyrrhotite, etc.) contain large concentrations of iron (oxides and sulphides), paramagnetic minerals contain much smaller concentrations among the diamagnetic cations and anions. Therefore, a sample of rock or soil containing predominantly ferromagnetic minerals will give a much higher susceptibility than one containing, say, all paramagnetic minerals. Magnetite, for instance, is about 1000 times more magnetic than one of the strongest paramagnetic minerals (siderite for example), and about 10000 times stronger than the weakest clay minerals (illite for example). Hematite, being a canted antiferromagnetic mineral, exhibits susceptibility values close to that of strong paramagnetic minerals (siderite, Figure 2.4).

The paramagnetic minerals (a few of them are shown in Table 2.1 and Figures 2.2 and 2.4) include clay minerals (smectite, illite, montmorillonite, vermiculite, glauconite, chlorite, etc), iron and manganese carbonates (siderite, ferroan dolomite, rhodochrosite), ferromagnesian silicates (pyroxenes, amphiboles, etc.), as well as a variety of oxides and suphides of iron (ilmenite, pyrite, etc). Illite, siderite, ilmenite, chamosite, and some chlorites appear to be the most common paramagnetic minerals in sediment. (Note ilmenite is actually an antiferromagnetic mineral).

The mass magnetic susceptibilities of diamagnetic reservoir minerals possess relatively lower magnitudes compared to the paramagnetic and ferromagnetic classes (Figures 2.2,

2.3 and 2.4). They include kaolinite clay, alumino-silicate compounds (Na-Ca and K feldspars) as well as sulphates, carbonates and chlorides of diamagnetic cations. Elemental carbon has the most negative values of diamagnetic susceptibility. While minerals like graphite and kaolinite have negative mass diamagnetic susceptibilities, calcite, quartz and magnesite have significantly smaller negative susceptibilities (Table 2.1). Dolomite and gypsum exhibit susceptibilities in the mid range of these two extremes.

2.4 Magnetic domain theory and domain size

As mentioned in section 2.2.4 ferrimagnetic materials are composed of small regions, called magnetic domains, where magnetic moments are aligned either parallel or antiparallel (Kittel, 1949). The existence of domains is hinted at by the observation that some magnetic properties, in particular, coercivity and remanence vary greatly with grain size (after Dunlop 1981). The main reason for domain formation is the magnetocrystalline energy. Such energies act as a source of demagnetizing field within the crystal. In order to reduce the effect of these demagnetizing fields, the crystal divides itself into a number of domains, which are separated by Domain walls also called Bloch walls. When a strong external field is applied on the sample, it overcomes the energies required to establish the Bloch walls. As a result, the domain walls vanish and the individual magnetic moments start aligning with the external applied field. Upon removal of the field, the Bloch walls may or may not come back to their original positions, and this causes a remanent magnetization in the materials. However, if the applied field is weak, the Bloch walls return to their original positions upon removal of the applied field (Thompson and Oldfield, 1986).

Domains are small in size (0.8-100's microns), but much larger than atomic distances. The behaviour of magnetic materials can therefore be subdivided on the basis of their grain size falling into four categories: multidomain (MD), single domain (SD), pseudo-single domain (PSD), and superparamagnetic (SP).

2.4.1 Multidomain (MD)

The crystals which contain more than one domain are called multidomain (MD). In most cases, the numbers of domains in a given crystal are linked to its size. The larger the crystal, the higher the number of domains it will have. Multidomain grains tend to be magnetized easily because their domain walls can be easily translated by the

application of an external magnetic field. Therefore, such grains show low values of coercivity and remanence. Some text books state that the number of domains for a given grain size depends on the magnitudes of the exchange and magnetocrystalline energies which again are directly linked to the grain size. .

2.4.2 Single domain (SD)

Smaller crystal sizes accommodate only one domain within which all the atomic magnetic moments are aligned in parallel. Since there are no domain walls present in these grains, relatively higher external fields are required to change the direction of their atomic magnetic moments, the reason SD grains are magnetically hard and have high values of coercivity and remanence (Argyle and Dunlop, 1990). The threshold size for SD grains depend on several factors including their saturation magnetization and the shape of the grain. In most cases, the SD-MD threshold size are based on theoretical calculations. For example, for magnetite, it is about 80 nm and for hematite is about 15μm (much larger than magnetite because its saturation magnetization is about 200 times lower than for magnetite) (Butler and Banerjee, 1975).

2.4.3 Pseudo-single domain (PSD)

The crystals which contain only a few domains show magnetic properties that are a mixture of SD and MD behaviour. These grains are considered as pseudo-single domain (PSD). PSD grains are commonly found in natural rocks. For magnetite, this behaviour occurs in the size range between 0.1-20μm (Argyle and Dunlop, 1990). PSD grains are extremely stable and can hold remanent magnetisation over very long periods of time (Merrill et al., 1996).

2.4.4 Superparamagnetism (SP)

SP grains are the ultrafine ferromagnetic crystals which can no longer retain magnetic remanence. In the absence of an external magnetic field, they show no alignment of atomic magnetic moments (paramagnetic behaviour). However, in the presence of an applied magnetic field, they show very high induced magnetization, the reason they are called superparamagnetic. Table 2.3 shows the threshold sizes for some of the superparamagnetic minerals found in reservoir sediments.

2.5 Magnetic hysteresis

Magnetic hysteresis denotes the non-reversible behaviour of magnetization when the sample is cycled in an external magnetic feild. A typical hysteresis curve (a plot of the variation of magnetization 'M' with applied field 'H') is shown in Figure 2.6. It is shown that as the ferromagnetic sample goes through the hysteresis cycle, a remanent magnetization is formed and the sample is unable to return back to its original magnetization state. The full hysteresis curve is obtained when the magnetic field is gradually increased to the saturation magnetization of the sample and then cycled to a negative maximum. The area enclosed by the hysteresis loop represents the ferromagnetic energy stored by the sample (Vasudeva, 1966).

2.5.1 Magnetic hysteresis parameters

Various diagnostic magnetic parameters obtained from the hysteresis loop are saturation magnetization (Ms), saturation remanent magnetization (Mrs), coercivity (Hc), coercivity of remanence (Hcr), and low field (L_{fld}) and high field (H_{fld}) magnetic susceptibilities. In **Chapter 5**, I will show detailed experimental results on the hystereis properties of various types of rock minerals at reservoir temperatures. Here I will briefly explain these parameters. Their interpretation on the identification of magnetic mineralogy is explained in section 2.6.1.

From Figure 2.6, Ms is equivalent to the amount of magnetization produced at saturation (saturation is the point where the material cannot acquire any more magnetism with increased applied field). The field required to reach Ms is lower for ferromagnetic minerals because they are the easiest to magnetize. In cases where the sample is dominated by weaker magnetic minerals (canted antiferromagnetic, paramagnetic, and diamagnetic), extreme fields up to 3 Tesla are required to make all of their atomic magnetic moments to respond to the field (Hill, 1982). Standard laboratory instruments cannot achieve these high fields. Therefore the true saturation magnetization cannot be determined for these minerals. However, the magnetization created in the sample from the maximum field applied in the laboratory is often considered to be the saturation magnetization. Now if the magnetizing field is gradually decreased to zero, it is found that the intensity of magnetization instead of being zero has a certain value. This value of magnetization for which H=0, is called residual magnetism or remanent magnetization (Mrs). Application of a reverse field leads to a point where the overall magnetization is zero (M = 0 on hysteresis loop). The field

necessary to achieve this is called the coercivity (Hc). To arrive back at the origin (point where the sample has zero remanent magnetism), a somewhat stronger reverse field is necessary denoted by Hcr in Figure 2.6. Low-field magnetic susceptibility (χ_{Lfld}) or initial magnetic susceptibility is measured as the gradient of the magnetisation curve of its reversible part. It is observed in low fields, in the order of the magnetic field of the Earth. Similarly, the high-field magnetic susceptibility (χ_{Hfld}) is the gradient of the closed linear part of the hysteresis loop observed at high fields. Slope corrected hysteresis loops allow Ms, Mrs, Hc, and Hcr to be discriminated on the basis of individual magnetic minerals (antiferro-, ferri-, or ferro-). Such loops are called ferromagnetic hysteresis loops and are discussed in Section 5.5 (**Chapter 5**) of this thesis.

2.5.2 Effect of grain size on hysteresis loops

The shape of a hysteresis loop is determined partly by the domain state of the material. For instance, an SD grain that has its easy magnetisation axis parallel to the magnetic field can switch between equilibrium states only when the reversed applied field is strong enough to subdue the anisotropy energy barrier. That's why hysteresis loops for SD materials are typically wider than for MD materials where the anisotropy energy barrier is relatively lower. This is just a reflection of the higher coercivity and remanence in SD material. Thus, for an assembly of randomly oriented SD grains the type of curve as illustrated in Figure 2.6 is produced. However, when the field is perpendicular to the grain's easy axis there is no hysteresis observed as the equilibrium states have equal magnetisation. MD grains exhibit more complex behaviour as they may have any number of equilibrium positions which are sensitive to the previous petrological and magnetic history of the grains. Such grains in general exhibit narrower hysteresis loops than SD grains.

Plotting Hcr/Hc values versus Mrs/Ms for different grain sizes of a single ferromagnetic mineral has proven very useful in distinguishing domain states (Day et al., 1977) and is known as a Day plot. It was initially used to define possible domain states for titanomagnetite and later calibrated for magnetite (Thompson and Oldfield, 1986; Tauxe, 1993; Dunlop, 2002). In fact, Mrs/Ms is a definitive test for differentiating between SD and non-SD particles. The combination of Hcr/Hc and Mrs/Ms ratios can be used to estimate bulk domain state and average particle size for the ferromagnetic fraction. Hysteresis parameters of various SP-SD and SD-MD mixtures and the

influence of SP grains are shown in Figure 2.7 (after Geiss, 1999). From this figure it becomes clear that a plot of Mrs/Ms and Hcr/Hc can give a general idea of the sizes of the magnetic particles present, but it should be used with a close inspection of magnetic mineralogy and the original hysteresis loop.

In Day's original plot, only the discrete sizes of remanence carrying particles of titanomagnetite grains were considered, with different regions of the plot depicting multidomain (MD), pseudo-single domain (PSD) and single domain (SD) states. As the applied field is reduced to zero after reaching Ms, each SD grain rotates to the nearest easy magnetisation direction, resulting in a random dispersion of uniaxial SD particles having an Mrs/Ms value of 0.5 (Dunlop and Ozdemir, 1997). In MD grains, when a strong field is applied, domain walls are destroyed and the magnetisation reaches saturation. On removal of the magnetising field domains reform and, because of lattice imperfection and internal strains, rather than returning exactly to their initial positions, the domain walls settle only near initial positions, resulting in a small remanent magnetisation. For ideal MD grains Mrs/Ms is generally < 0.05. Hcr/Hc has less discriminating power in comparison with Mrs/Ms, however Hcr/Hc is equal to around 1 for SD grains and for ideal MD grains Hcr/Hc >~4 (Dunlop and Ozdemir, 1997).

2.5.3 Effect of various clay minerals on hysteresis loops

In **Chapter 5**, we will see that the shape of the hysteresis curve depends on the amount and type of clay minerals present in the samples. Therefore, it is essential to provide the reader a basic overview of how various combinations of diamagnetic, paramagnetic and ferromagnetic minerals affect the shape of the hysteresis loop. As mentioned in section 2.2.3, only ferromagnets can retain a memory of the applied field, and hence can generate a hysteresis loop. However, the high field slope of the hysteresis loop will tell us whether any paramagnetic or diamagnetic minerals are also present in the sample and approximately in how much concentration. Therefore, in a complex case of a high applied magnetic field well above the saturation magnetisation (Ms) of any ferromagnetic component in the sample, only the paramagnetic, diamagnetic, and antiferromagnetic matrix minerals will respond to the external field. Diamagnetic minerals are recognised by exhibiting straight lines of negative high field slope. In contrast, paramagnetic minerals exhibit straight lines with a positive slope. A mixture of a diamagnetic matrix mineral (such as quartz) and a paramagnetic clay mineral (such as illite) will have a slope that is dependent upon the content of the two minerals. Changes

in the slope of the hysteresis curves potentially allow very sensitive and subtle changes in the magnetic mineralogy to be readily recognized (Potter and Ivakhnenco, 2007). The complex multi-component hysteresis curves exhibit graphically the magnetic contribution of these components, and also numerically through the values of the high and low field magnetic susceptibilities (the slopes at high and low fields).

Figure 2.8 shows typical hysteresis loops for a ferromagnetic and paramagnetic combination (ferro+para), an antiferromagnetic and diamagnetic combination (antiferro+dia), and for relatively clean paramagnetic and diamagnetic samples. The large kink at low fields for antiferro+dia shows that there is a reasonable amount of antiferromagnetic minerals inside the sample. The negative high field slope indicates that the main matrix mineral in the sample is diamagnetic. On the other hand, a smaller kink at low fields for ferro+para shows that the sample contains only a small percentage of ferromagnetic minerals whereas the positive high field slope indicates the presence of paramagnetic component.

2.5.4 Equipment used for hysteresis and thermomagnetic measurements

The magnetic hysteresis parameters and temperature dependent susceptibility (TDS) curves shown in **Chapter 5** were measured by using the Variable Field Translation Balance (VFTB) located in the rock magnetic laboratory of the Ludwig-Maximilian University in Munich, Germany. The VFTB system (Illustration 2.1) is a one-dimensional harmonic oscillator with damping in the forced oscillation mode. It has a horizontal translation balance in which the magnetisation of the sample is measured. The measurements can be made in fields up to 1000 mT. The temperature can be controlled using an oven and liquid nitrogen within a range from -170 ^{o}C to 700 ^{o}C.

The main advantage of the VFTB is that all the apparatus is computer controlled so that once the sample is in the measuring position, many experiments can be applied to the same sample. Thus a whole range of magnetic experiments can be carried out including isothermal remanent magnetization (IRM), natural remanent magnetization (NRM), saturation isothermal remanent magnetization (SIRM) and thermomagnetic analysis. Normally a hysteresis loop measurement is followed by the thermomagnetic measurements.

The studied reservoir sample consists of powdered material or sediment chips of known mass (normally about 0.5 g) and is compacted into a non-magnetic container. The sample is very tightly packed into the container with quartz wool in order to fix the material and to avoid contamination by air (material oxidation). The sample holder slides into the sleeve at the end of the balance assembly. The obtained data is processed using a software program VFTB Analyser 1.6, which allows mass correction for each sample as well as determination of magnetic properties such as Ms, Mrs, Hc, Hcr, etc.

Illustration 2.1: The Variable Field Translation Balance (VFTB).

2.6 Magnetic susceptibility

As discussed in section 2.2, all substances are affected by the application of a magnetic field. The intensity of magnetic force lines changes which depends on the type of magnetic minerals present. Diamagnetic substances cause a reduction in the density of magnetic force lines making the applied field weaker. In contrast paramagnetic and ferromagnetic substances cause an increase in the density of magnetic force lines hence reinforcing the applied magnetic field. The analogue of such a change of magnetic field inside a substance, named magnetic induction B, is described as follows.

$$B = \mu_0(H+M) \qquad (2.3)$$

where H is the magnetic field strength, μ_0 is the permeability of free space ($4\pi\times10^{-7}$ Henry/m), and M is the intensity of magnetisation of a substance, related to unit volume. It is convenient to have the parameters in equation (2.3) independent of magnetic field strength. Thus dividing equation (2.3) by H we have:

$$\mu = B/H = \mu_0+\mu_0 M/H = \mu_0+\mu_0\chi_v \tag{2.4}$$

In this equation μ is the relative permeability, which is proportional to the dimensionless coefficient, the volume magnetic susceptibility χ_v. From equation (2.1), we can write the volume magnetic susceptibility χ_v as:

$$\chi_V = \frac{M}{H} \tag{2.5}$$

where M is the magnetization induced in the sample and H is the applied magnetic field (both in units of Am^{-1} and therefore χ_v is dimensionless). χ_v is a bulk measurement that groups all of the magnetic subpopulations present in a sample into one value. Since measurements of χ_v do not account for mass, they are sensitive to changes in the bulk density of the material being measured**.** Therefore χ_v measurements are corrected for mass to account for any bulk density differences between the samples. This allows for an accurate and easier comparison of χ_v. Mass dependent susceptibility (χ_m) is determined by:

$$\chi_m = \frac{M_m}{H} = \frac{\chi_v}{\rho} \tag{2.6}$$

where χ_m is the mass magnetic susceptibility measured in $m^3\ kg^{-1}$, M_m is the mass magnetisation, and ρ is the density of the sample.

2.6.1 Initial magnetic susceptibility at room temperature

The low field magnetic susceptibility (χ_{Lfld}) is measured normally in a low steady field ($\approx$ 1 mT). It can also be measured in a low alternating magnetic field. As detailed in Section 2.6, it is defined as the ratio of the magnetisation to the applied magnetic field.

It is also the initial gradient of the magnetisation curve in a magnetic hysteresis loop (see Section 2.5).

The magnetic susceptibility that is conventionally measured in the laboratory by the most standard equipment is the extrinsic or apparent initial magnetic susceptibility (χ_0) (Moskowitz, 1991), which is different from the intrinsic magnetic susceptibility (χ_i). The difference is due to the effects of substance self-demagnetisation. Hence, the intrinsic susceptibility is the 'true' magnetic susceptibility after removal of the effects of internal demagnetising fields in the substance. In general, unless stated otherwise, it is the low field extrinsic magnetic susceptibility that is implied by the term 'magnetic susceptibility' in the text of this thesis.

Inside a magnetic mineral the applied filed (H) is opposed due to the presence of magnetocrystalline energies within the mineral. The magnitude of the demagnetising field is N_dM, where N_d is the demagnetising factor which depends on the grain size, grain shape and its domain state, and M is the magnetisation. Consequently, inside the grain the internal magnetic field H_i is (Moskowitz, 1991)

$$H_i = H - N_dM \tag{2.7}$$

The magnetisation is given by

$$M = \chi_i H_i \tag{2.8}$$

Thus, extrinsic magnetic susceptibility has the following relationship to the intrinsic susceptibility:

$$\chi_0 = \chi_i/(1+N_d\chi_i) \tag{2.9}$$

For strong ferromagnetic and ferrimagnetic materials, such as magnetite, $N_d\chi_i$ is greater than 1. Since the magnitude of the measured susceptibility also depends on the volume concentration of the ferromagnetic minerals (C_{ferro}), it is convenient that for ferromagnetic minerals of strong susceptibility, $\chi_0 \approx 1/N_d$. Therefore in most instances the initial magnetic susceptibility is given by the following

$$\chi_0 = C_{ferro}\chi_0 \approx C_{ferro}/N_d \quad (2.10)$$

In natural samples containing magnetite with spherical grains, the demagnetisation factor is nearly 1/3. Therefore, the approximate volume fraction of magnetite can be estimated as (Thompson and Oldfield, 1986):

$$C_{ferro} \approx \chi_0/3 \quad (2.11)$$

Initial magnetic susceptibility of ferromagnetic and ferrimagnetic fractions is induced due to reversible displacement of mobile domain walls in MD grains or magnetic moment rotation in SD particles. For SD grains the low magnetic fields are not very effective in rotating SD moments. Therefore, the magnetic susceptibilities in SD and PSD particles are usually lower than MD grains.

Initial magnetic susceptibility depends not only on ferromagnetic but also on paramagnetic and diamagnetic minerals. In sediments the concentration of ferromagnetic minerals is often so low that the measured susceptibility values reflect changes in non-ferromagnetic minerals such as silicates, carbonates and clays. However such minerals may contain a varying amount of iron impurities and hence show a range of magnetic susceptibilities depending on their chemistry. Therefore Equation 2.10 has to be used with caution for reservoir sediments.

2.6.2 Magnetic susceptibility of minerals at reservoir temperatures

As mentioned in section 2.2, all minerals belong to one of the five classes of magnetic behaviour (diamagnetism, paramagnetism, ferromagnetism, ferrimagnetism and antiferromagnetism). In this section, I will discuss the effect of temperature on these five classes of minerals. These temperature-susceptibility analyses will indirectly model the behaviour of minerals at in-situ conditions.

Section 2.2.1 explains that diamagnetic susceptibility is almost independent of temperature. The paramagnetic susceptibility in most cases decreases exponentially with temperature according to the Curie law (Butler, 1992). The exceptions are Pauli paramagnets where the electrons are able to wander through the lattice (in case of paramagnetic metals) and hence the localized moment approximation is unlikely to be a

good one. In such cases, the magnetic susceptibility is more or less independent of temperature.

The temperature dependence of paramagnetic susceptibility can be explained by the Langevin localized moment model by assuming that the non-interacting magnetic moments on atomic sites are randomly oriented as a result of their thermal energy. When an external magnetic field is applied, the orientation of the atomic moments shifts slightly towards the field direction. According to Langevin model, the magnetization of a paramagnetic material is related to the temperature by the equation (Langevin, 1905)

$$M = \frac{Nm\alpha}{3} = \frac{Nm^2}{3k_B}\frac{H}{T} \tag{2.12}$$

or

$$\chi = \frac{M}{H} = \frac{Nm^2}{3k_B T} = \frac{C}{T} \tag{2.13}$$

where $C = Nm^2/3k_B$ is a constant, m and H represent the magnitudes of the magnetic moment and field vectors respectively, and k_B is Boltzmann's constant.

The above equation is called the Curie law; the susceptibility of a paramagnet is inversely proportional to the temperature. This law assumes that the localized atomic magnetic moments do not interact with each other. Instead, they are just reoriented by the applied magnetic field. Materials which obey this law contain magnetic moments which are localized at the atomic or ionic state. The hydrated salts of transition metals are examples of this type of behaviour as they are surrounded by a number of non-magnetic ions/atoms, which prevent interaction between neighboring magnetic moments.

Many paramagnetic materials do not obey the Curie law, but instead follow a more general temperature dependence, the Curie-Weiss law (Kittel 1996). Weiss explained the Curie-Weiss behaviour by postulating the existence of an internal interaction between the localized moments which he called a 'molecular field'. Weiss assumed that the intensity of the molecular field is directly proportional to the magnetization (Petty, 2007):

$$H_w = \gamma M \tag{2.14}$$

$$H_{total} = H + H_w \tag{2.15}$$

Substituting equations 2.13 and 2.14 into equation 2.15, we get

$$\frac{M}{H + \gamma M} = \frac{C}{T} \tag{2.16}$$

$$M = \frac{CH}{T - C\gamma} \tag{2.17}$$

Therefore,

$$\chi = \frac{M}{H} = \frac{C}{Tc - \theta} \tag{2.18}$$

θ is called the paramagnetic Curie temperature for a ferromagnet. When a ferromagnetic material is heated, its spontaneous magnetization disappears at the ferromagnetic Curie temperature Tc (Tc ≤ θ). The paramagnetic Curie temperature (θ) for a ferromagnetic solid is several degrees higher than the ferromagnetic Curie temperature (Tc). The gradual transition from ferromagnetic to paramagnetic behaviour is explained by persistence of the molecular field due to short-range magnetic order above Tc. At temperatures higher than the paramagnetic Curie temperature, the susceptibility χ becomes the paramagnetic susceptibility and is proportional to 1/(Tc- θ) as given by the Curie-Weiss law. Tc is a direct measure of the strength of the magnetic exchange interactions (Dunlop and Ozdemir, 1997). In brief, when θ = 0, the Curie-Weiss law equates to the Curie law (as in case of paramagnets). When θ ≠ 0, there is an interaction between neighboring magnetic moments and the material is either ferromagnetic or antiferromagntic (Petty, 2007). If θ is positive then the material is ferromagnetic below the transition temperature and the value of θ corresponds to the transition temperature Tc. If θ is negative then the material is antiferromagnetic below the transition temperature. In both cases, the material can only be paramagnetic when the temperature goes above Tc.

The spontaneous magnetisation of a single magnetic phase (Msp) has the following dependence with temperature.

$$Msp(T) \alpha (Tc - T)^{\gamma} \quad (2.19)$$

where γ is 0.5 in the molecular field approximation (Dunlop and Ozdemir, 1997). The thermomagnetic Msp(T) or Curie curve is therefore relatively simple for a single magnetic phase. A major disadvantage of high temperature measurements is the frequent occurrence of irreversible changes in magnetic mineralogy through oxidation, reduction and dehydration leading to the destruction of original minerals and the formation of new ones. Table 2.4 summarizes the major mineral transformations and shows that they may give rise to a variety of changes in susceptibility-temperature curves. In many sedimentary samples these alterations occur below Tc and the thermomagnetic curves therefore record the thermo-chemical stability of the sample rather than Tc. The degree of alteration can be also observed from the differences between the cooling and heating curves. Some of the common alteration states of thermomagnetic measurements include the inversion of maghemite to hematite, the dehydration of iron hydroxides or the conversion of iron sulphides to iron oxides. In **Chapter 5**, I have used experimental thermomagnetic results to simulate magnetic properties at reservoir temperatures.

In Table 2.5, I have calculated the variations in magnetic susceptibility at various temperatures for paramagnetic, ferromagnetic and anti-ferromagnetic minerals. I have taken room temperature magnetic susceptibility values for these materials from Tables 2.1 and 2.2 and calculated the change in magnetic susceptibility versus temperature using the Curie-Weiss law. The results are shown in two columns under each mineral (except illite which has a single susceptibility value at room temperature) showing the upper and lower limit of susceptibility values given for each of these minerals in the literature. The susceptibility versus temperature results are plotted in Figure 2.9 showing the variations in susceptibility values from low temperate (light orange colour) to high temperature (dark red colour). Figure 2.10 shows the results of Table 2.5 on a logarithmic scale. Note that for magnetite and hematite, the mass magnetic susceptibility increases with temperature (between 20-330 ^{o}C) indicating that certain minerals may have transformed into high susceptibility minerals at these temperatures.

Figure 2.11 shows the experimental thermomagnetic curves measured for hematite sample MST1. In a standard experiment the sample is heated from room temperature to a maximum temperature of 700 °C. The magnetisation is measured during the heating

and cooling runs. The sample is heated in a closed holder in order to avoid the effects of high-temperature oxidation. Figure 2.11a shows that the sample has a Curie point (Tc) equal to 675 ^{o}C. This is also evident by a large spike shown in Figure 2.11b at 675 ^{o}C which is a plot of the 2nd derivative of the magnetization values of Figure 2.11a versus applied field. It can also be seen that the shape of the cooling curve closely follows the heating curve indicating that there have been very limited oxidation effects and/or changes in mineralogy. The fact that the two curves are not identical indicates the effects of thermal delay (the time ferromagnetic minerals take to reform their magnetic domains during the cooling process).

2.7 Summary

In this chapter the main principles of magnetism, and mineral magnetic properties and techniques applicable to the petroleum industry have been discussed. The previously published magnetic susceptibility data for minerals related to reservoir matrix rocks has been summarised. The following points are worth noting from the analysis:

- According to the general classification criteria of magnetic properties, such as magnetic susceptibility and remanent magnetisation, reservoir rock matrix minerals will comprise one or more of five principal magnetic groups: diamagnetic, paramagnetic (including perfectly compensated antiferromagnetic), ferromagnetic, ferrimagnetic, and canted antiferromagnetic.

- Magnetic susceptibility is a universal and fundamental quantitative characteristic of all levels of substance, from atoms and molecules to rocks. The reservoir rock susceptibility is the magnetic susceptibility of the sum of all the minerals present.

- Diamagnetic substances (such as the major rock matrix minerals quartz and calcite) are characterised by negative magnetic susceptibility values, absence of remanent magnetisation, and independence of magnetic susceptibility with temperature.

- Paramagnetic materials (such as the permeability controlling clay illite) exhibit positive values of magnetic susceptibility, absence of remanent magnetisation, and inverse linear dependence of the magnetic susceptibility with temperature. The perfectly antiferromagnetic class is included in this group, which normally is distinguished with the presence of a Curie point (Tc). For diamagnetic and

paramagnetic substances the magnetic susceptibility at high fields is the same as that at low fields ($\chi_{Hfld}=\chi_{Lfld}$). Paramagnetic substances exhibit thermomagnetic curves for magnetic susceptibility and induced magnetisation.

- Ferromagnetic substances possess high positive values of magnetic susceptibility (significantly higher values compared to paramagnetic minerals). They acquire remanent magnetisation, and exhibit a specific dependence of this remanence on temperature with conversion to the paramagnetic state above T_C. The ferrimagnetic class belongs to this group together with the imperfect (canted) antiferromagnetic minerals, such as hematite. In addition, this group is characterised by the applied field dependent parameters of magnetic susceptibility (χ_{Lfld}, χ_{Hfld}), magnetisations (Ms), remanence (Mrs), coercivity (Hc, Hcr) and Curie point.

- The shapes of the hysteresis curves depend on the amount and type of minerals present in the samples. Diamagnetic substances are represented by straight lines with negative slope whereas paramagnetic minerals are represented by straight lines with positive slope. The characteristic "kinks" in the low field part of hysteresis loops indicate the presence of ferromagnetic minerals.

- Temperature dependent susceptibility measurements can be used to simulate in-situ reservoir conditions and to model the reservoir thermomagnetic conditions.

Minerals and compounds	**Mass magnetic susceptibility, χ_m (10^{-8} m^3 kg^{-1})**	**Density (10^3 kg m^{-3})**	**Composition**	**References**
Paramagnets and Compensated Antiferromagnets				
Arsenopyrite	50	6.05	FeAsS	te,wy
Chalcopyrite	(0.55-10)	4.2	$CuFeS_2$	bi,bl,te,wy
Chamosite	~90		$(Mg,Fe)_3Fe_3[AlSi_3O_{10}](OH)_8$	co,th
Chlorite Chlorite BVS[bo]	2.5-55.4	2.8	$(Mg,Al,Fe)_{12}[(Si,Al)_8O_{20}](OH)_{16}$	ta
Chlorite CFS	52.5			
Fe-dolomite	1.1		$(Ca,Mg,Fe)CO_3$	mu
Ferrous chlorite	145		$FeCl_2$	co
Ferrous sulphite	51.7		$FeSO_4 \cdot 7H_2O$	co
Glauconite	~41.6	2.4	$(K,Na)(Al,Fe,Mg)_2[(Al,Si)_4O_{10}](OH)_2$	de
Illite	15	2.75	$(K_{1-1.5}Al_4)[(Si_{7-6.5}Al_{1-1.5}O_{20}](OH)_4$	br,ca,co,du,th
Ilmenite	100-115		$FeTiO_3$	bl,ca,co,du,fo
Lepidocrocite	40-70	4.25	γ- FeOOH	bl,fo,th
Limonite	66-74	4.24	$FeOOH \cdot nH_2O$	bl,th
Manganese sulphate	81		$MnSO_4 \cdot 4H_2O$	co
Montmorillonite	13-14	2.5	$Na_{0.7}(Mg_{0.7}Al_{3.3}Si_8O_{20})OH_4 \cdot nH_2O$	br,ca,co,du
Muscovite	1-15	1.1	$KAl_2[(AlSi3)O_{10}](OH)_2$	mu
Nontronite	65, ~90		$Na_{0.33}Fe_2[(Al_{0.33}Si_{3.67})_4O_{10}](OH)_2 \cdot nH_2O$	co,th
Pyrite	1-100	5.02	FeS_2	bi,bl,fo,hi,to,wy
Siderite	32-270	3.96	$FeCO_3$	bi,br,hi,me,te,pa
Smectite	~3.2	7.06	$(1/2Ca,NA)_{0.7}(Al,Mg,Fe)_4[(Si,Al)_8O_{20}]\ nH_2O$	ma
Troilite	13-36	4.83	FeS	bi,bl,fo,hi
Vermiculite	15.2		$(Mg,Fe,Al)_3[(Al,Si)_4O_{10}](OH)_2 \cdot 4H_2O$	mu
Diamagnets				
Anhydrite	-0.5 - -2	2.8	$CaSO_4$	bi,br,pa,to
Calcite	-0.48	1.56	$CaCO_3$	bi,br,wy
Dolomite	~-1.2	3.16	$CaMg(CO_3)_2$	to,wy
Feldspar	-0.49 - -0.67	2.65	$(K,Na)AlSi_3O_8$ and $Ca(Na)Al_2Si_2O_8$	bl,du,mu,pe
Graphite	-3.7 - -9.3	2.16	C	bi,sh,to,wa,wy
Gypsum	-0.5 - -1.3	2.6	$CaSO_4 \cdot nH_2O$	bi,sh,wa,wy
Halite Sodium Chlorite	-0.48 - -0.75 -0.64	2.08	NaCl	bi,br,sh,wa,wy
Kaolinite	-2	2.63	$Al_4[Si_4O_{10}](OH)_8$	de
Magnesite	-0.48		$MgCO_3$	co
Quartz	-0.5 - -0.6	2.6	SiO_2	bi,br,pa,to

Table 2.1: Initial mass magnetic susceptibilities of diamagnetic, paramagnetic and compensated antiferromagnetic minerals of petroleum-bearing sediments and compounds related to the hydrocarbon industry. All magnetic susceptibilities were measured in weak fields at room temperature and at a pressure of one atmosphere. Literature values for susceptibilities were converted into SI units when necessary and from volume to mass susceptibility using appropriate values for densities.
[bi]Biot, 1962, [bl]Bleil et al, 1982, [bo]Borradaile et al, 1990, [br]Brace, 1965, [ca]Carmichael, 1989, [co]Collinson, 1983, [de]Deer et al, 1992, [do]Dortman, 1976, [du]Dunlop and Ozdemir, 1997, [fo]Foex et al, 1957, [hi]Hill, 1963, [ma]Matteson et al, 2000, [me]Melnikov, 1975, [mu]Mullins, 1977, [pa]Parasnis, 1979, [pe]Petersen, 1985, [sh]Sharma, 1986, [ta]Tarling and Hrouda, 1993, [te]Telford et al, 1990, [th]Thompson and Oldfield, 1986, [to]Torquato, 1991, [wa]Watt, 1988, [wy]Wyllie et al, 1958.

Minerals	**Magnetic order**	**Mass magnetic susceptibility, χ_m (10^{-8} m^3 kg^{-1})**	**Density (10^3 kg m^{-3})**	**Composition**	**Spontaneous magnetisation, Ms (10^3 A m^{-1})**	**References**
Iron	Ferromagnetic	50000	7.87	αFe	1715	co,du,hu,th
Magnetite	Ferrimagnetic	20000-110000	5.18	$FeFe_2O_4$	480	du,hu,th
Maghemite	Ferrimagnetic	40000-50000	4.90	λFe_2O_3	380	du,hu,th
Titano magnetite	Ferrimagnetic	2500-12000	4.98	$Fe_{3-x}Ti_xO_4$, x=0.6	125	du,hu
Titano maghemite	Ferrimagnetic	57000	4.99	$Fe_{(3-x)R}Ti_{xR\cdot 3(1-R)}O_4$, R=8/[8+z(1+x)]		co,hu
Greigite	Ferrimagnetic			Fe_3S_4	~125	du
Pyrrhotite	Ferrimagnetic	10-30000	4.62	$Fe_{1-x}S$	~80	du,hu
Hematite	Canted AFM	10-760	5.26	Fe_2O_3	~2.5	du,hu,mu
Goethite	AFM, weak FM	26-280	4.27	$\alpha FeOOH$	~2, <1	du,hu,th
Hydrated iron (II) sulphate	Ferrimagnetic	0.5-100	4.13	$FeSO_4.7H_2O$		ha

Table 2.2: Initial mass magnetic susceptibilities of ferromagnetic, ferrimagnetic and canted antiferromagnetic minerals of petroleum-bearing sediments and compounds related to the hydrocarbon industry. All magnetic susceptibilities were measured in weak fields at room temperature and at a pressure of one atmosphere. Literature values for susceptibilities were converted into SI units when necessary, and from volume to mass susceptibility using appropriate values for densities. FM: Ferromagnetic; AFM: Antiferromagnetic.
[co]Collinson, 1983, [du]Dunlop, Ozdemir, 1997, [ha]Hanson and Sauchuk, 1991, [hu]Hunt et al., 1995, [mu]Mullins, 1977, [th]Thompson and Oldfield, 1986.

Mineral	**Superparamagnetic threshold size (μm)**	**Single domain threshold size (μm)**
Maghemite	0.02-0.027[12]	0.03-0.11[15]
Magnetite	0.025-0.03[6,7,11]	0.05-0.08[1,5,8]
Hematite	0.025-0.03[2,3]	15[3]
Greigite	0.05[10]	0.8[10]
Titanomagnetite (TM 60)	0.08[4]	0.6[4,13]
Pyrrhotite		1-2[14]
Goethite		10-50[15]

Table 2.3: Single domain-multidomain and superparamagnetic-single domain threshold sizes of ferrimagnetic and ferromagnetic minerals. Argyle & Dunlop; 1984[1]; Bando et al, 1965[2]; Banerjee, 1971[3]; Butler and Banerjee, 1975[4]; Dunlop, 1973a[5]; Dunlop, 1973b[6]; Dunlop and Bina[7], 1977; Enkin and Williams, 1994[8]; Geiss and Heider, 1996[9]; Hoffmann, 1992[10]; McNab et al, 1968[11]; Moskowitz et al, 1997[12]; Soffel, 1971[13]; Soffel, 1977[14]; Soffel, 1991[15].

Minerals	**Curie or Neel temperature T_c/T_N (^oC)**	**Common high temperature mineral transformation**	**Effect on magnetic susceptibility**	**References**
Curie temperature (Tc) (ferro-para)				
Iron	765-780			co,du,hu,th
Magnetite	575-585			du,hu,th
Maghemite	590-675	Changes to haematite at ~300 ^oC	Decreases	du,hu,th
Titano-magnetite	480-580	Oxidises to titanomaghemite	Increases	hu
Titano-maghemite	280-400	Changes to magnetite	Increases	hu
Greigite	~330			du
Pyrrhotite	320			du,hu
Neel temperature (T_N) (antiferro-para)				
Hematite	675			du,hu,mu
Goethite	120	Dehydrates to haematite at 300-400 ^oC	A tiny change	du,hu,th
Lepidocrocite	-196	Changes to maghemite at 250-350 ^oC	Increases	
Titanohaematites		Changes to hematite at 675 ^oC	Increases	
Antiferro-para	Reduction/oxidation to magnetite/maghemite on cooling from ~600 ^oC		Increases	

Table 2.4: Curie/Neel temperatures and common high temperature mineral transformations of ferromagnetic, ferrimagnetic and canted antiferrimagnetic minerals of petroleum-bearing sediments and compounds related to hydrocarbon industry.
[co]Collinson, 1983, [du]Dunlop and Ozdemir, 1997, [hu]Hunt et al., 1995, [mu]Mullins, 1977, [th]Thompson and Oldfield, 1986.

	Illite	**Biotite**	**Siderite**	**Pyrite**	**Hematite**	**Magnetite**
Temp. (°C)	Mass MS, χ_m (10^{-6} m^3 kg^{-1}) χ_m = 0.15	Mass MS, χ_m (10^{-6} m^3 kg^{-1}) χ_m = 0.52-0.98	Mass MS, χ_m (10^{-6} m^3 kg^{-1}) χ_m = 0.32-2.7	Mass MS, χ_m (10^{-6} m^3 kg^{-1}) χ_m = 0.01-1.0	Mass MS, χ_m (10^{-6} m^3 kg^{-1}) χ_m = 0.1-7.6	Mass MS, χ_m (10^{-6} m^3 kg^{-1}) χ_m = 200-1100
20	0.1500	0.5200 - 0.9800	0.3200 - 2.7000	0.0100 - 1.0000	0.1000 - 7.6000	200.0000 - 1100.0000
30	0.1000	0.3467 - 0.6533	0.2133 - 1.8000	0.0067 - 0.6667	0.1016 - 7.7178	203.6364 - 1120.0000
50	0.0600	0.2080 - 0.3920	0.1280 - 1.0800	0.0040 - 0.4000	0.1048 - 7.9648	211.3208 - 1162.2642
70	0.0429	0.1486 - 0.2800	0.0914 - 0.7714	0.0029 - 0.2857	0.1083 - 8.2281	219.6078 - 1207.8431
90	0.0333	0.1156 - 0.2178	0.0711 - 0.6000	0.0022 - 0.2222	0.1120 - 8.5094	228.5714 - 1257.1429
110	0.0273	0.0945 - 0.1782	0.0582 - 0.4909	0.0018 - 0.1818	0.1159 - 8.8106	238.2979 - 1310.6383
130	0.0231	0.0800 - 0.1508	0.0492 - 0.4154	0.0015 - 0.1538	0.1202 - 9.1339	248.8889 - 1368.8889
150	0.0200	0.0693 - 0.1307	0.0427 - 0.3600	0.0013 - 0.1333	0.1248 - 9.4819	260.4651 - 1432.5581
170	0.0176	0.0612 - 0.1153	0.0376 - 0.3176	0.0012 - 0.1176	0.1297 - 9.8574	273.1707 - 1502.4390
190	0.0158	0.0547 - 0.1032	0.0337 - 0.2842	0.0011 - 0.1053	0.1351 - 10.2639	287.1795 - 1579.4872
210	0.0143	0.0495 - 0.0933	0.0305 - 0.2571	0.0010 - 0.0952	0.1409 - 10.7054	302.7027 - 1664.8649
230	0.0130	0.0452 - 0.0852	0.0278 - 0.2348	0.0009 - 0.0870	0.1472 - 11.1865	320.0000 - 1760.0000
250	0.0120	0.0416 - 0.0784	0.0256 - 0.2160	0.0008 - 0.0800	0.1541 - 11.7129	339.3939 - 1866.6667
270	0.0111	0.0385 - 0.0726	0.0237 - 0.2000	0.0007 - 0.0741	0.1617 - 12.2914	361.2903 - 1987.0968
290	0.0103	0.0359 - 0.0676	0.0221 - 0.1862	0.0007 - 0.0690	0.1701 - 12.9299	386.2069 - 2124.1379
310	0.0097	0.0335 - 0.0632	0.0206 - 0.1742	0.0006 - 0.0645	0.1795 - 13.6384	414.8148 - 2281.4815
330	0.0091	0.0315 - 0.0594	0.0194 - 0.1636	0.0006 - 0.0606	0.1899 - 14.4290	448.0000 - 2464.0000

Table 2.5: Calculated mass magnetic susceptibility (χ_m) values for common clay minerals (para, ferri and anti-ferro) at various reservoir temperatures using the Curie-Weiss law. The room temperature magnetic susceptibility values are taken from Tables 1 and 2. For illite there is a single χ_m value (0.15, hence shown in a single column); whereas for the other minerals, there is a range of χ_m values found in different literature. MS: Magnetic susceptibility.

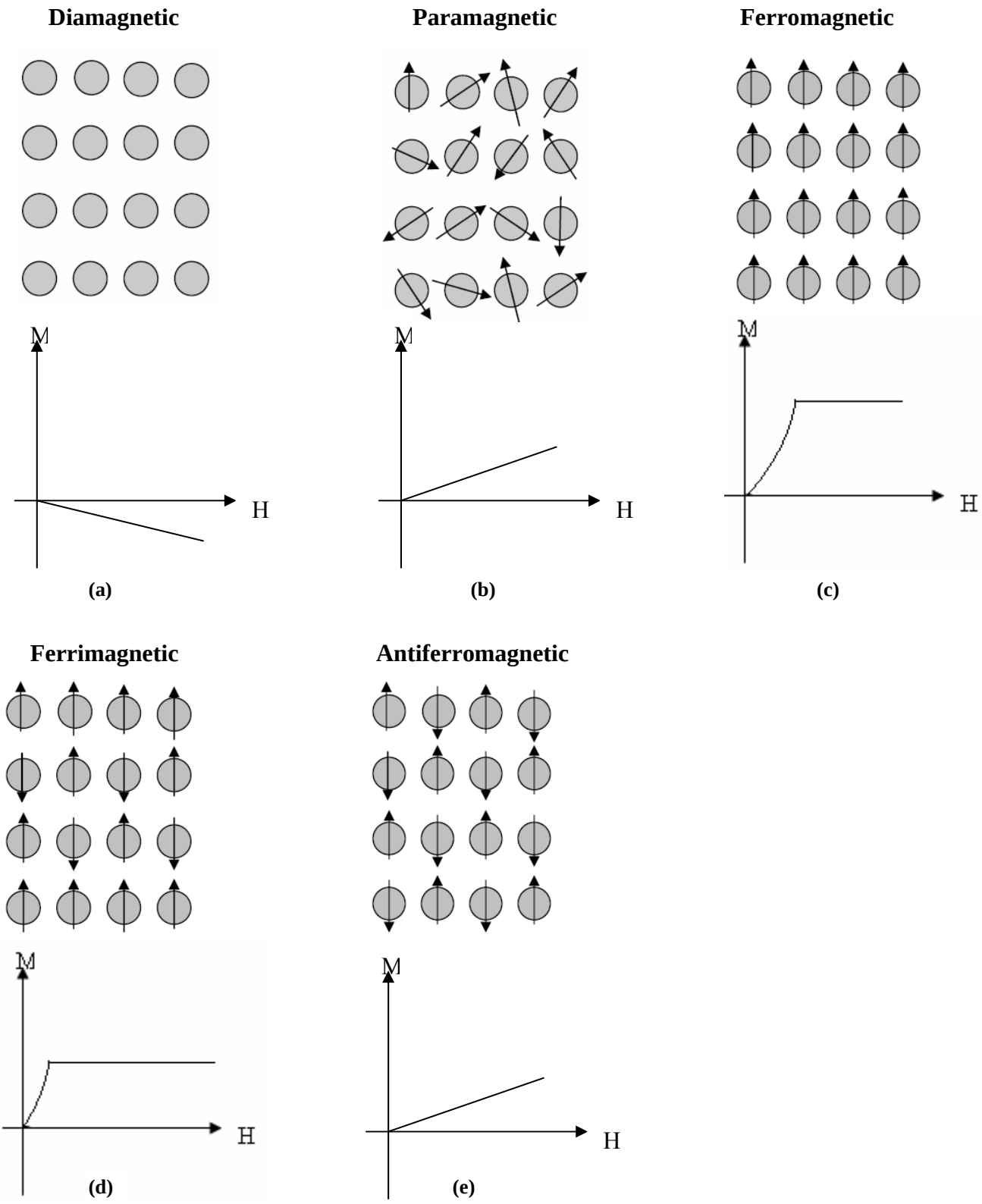

Figure 2.1: Atomic/magnetic behaviour of diamagnetic, paramagnetic, ferromagnetic, antiferromagnetic and ferrimagnetic classes of substances. Under each category, magnetization (M) is shown against the applied magnetic field (H); modified after Mee and Daniel (1988).

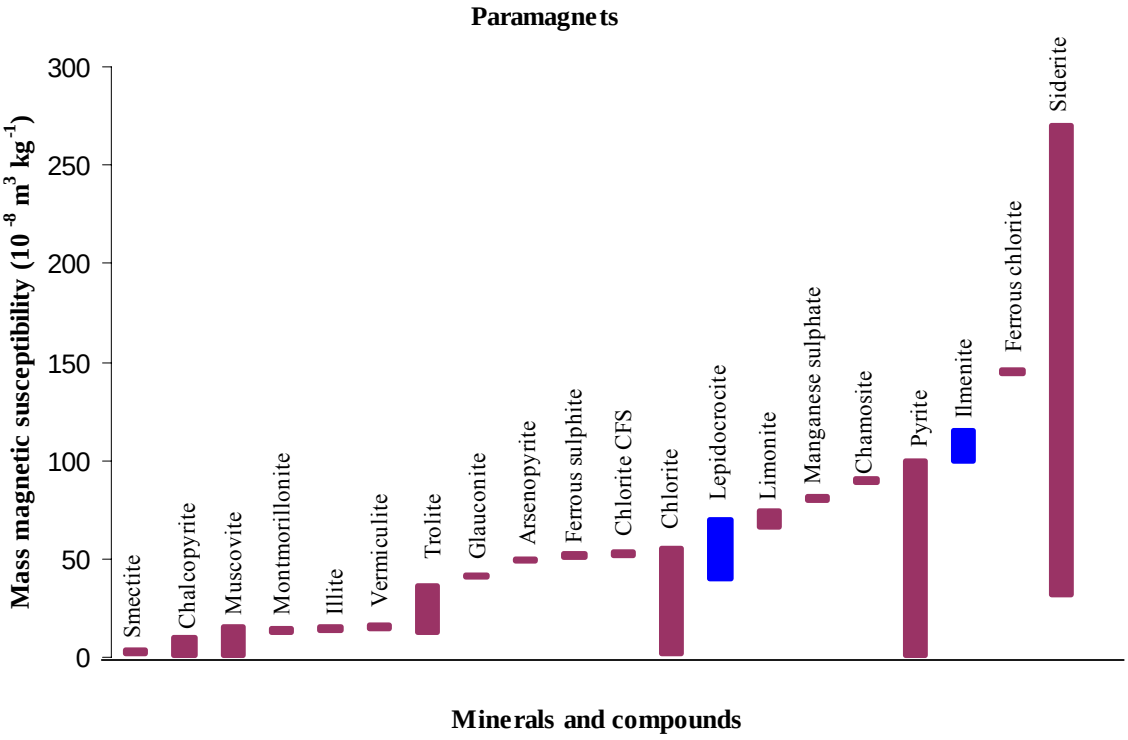

Figure 2.2: The range of initial mass magnetic susceptibility values (quoted by various authors) for paramagnetic and compensated antiferromagnetic minerals related to hydrocarbon reservoirs and their sediment environment. Lepidocrocite and ilmenite are antiferromagnetic minerals. The values for the minerals were taken from Table 2.1.

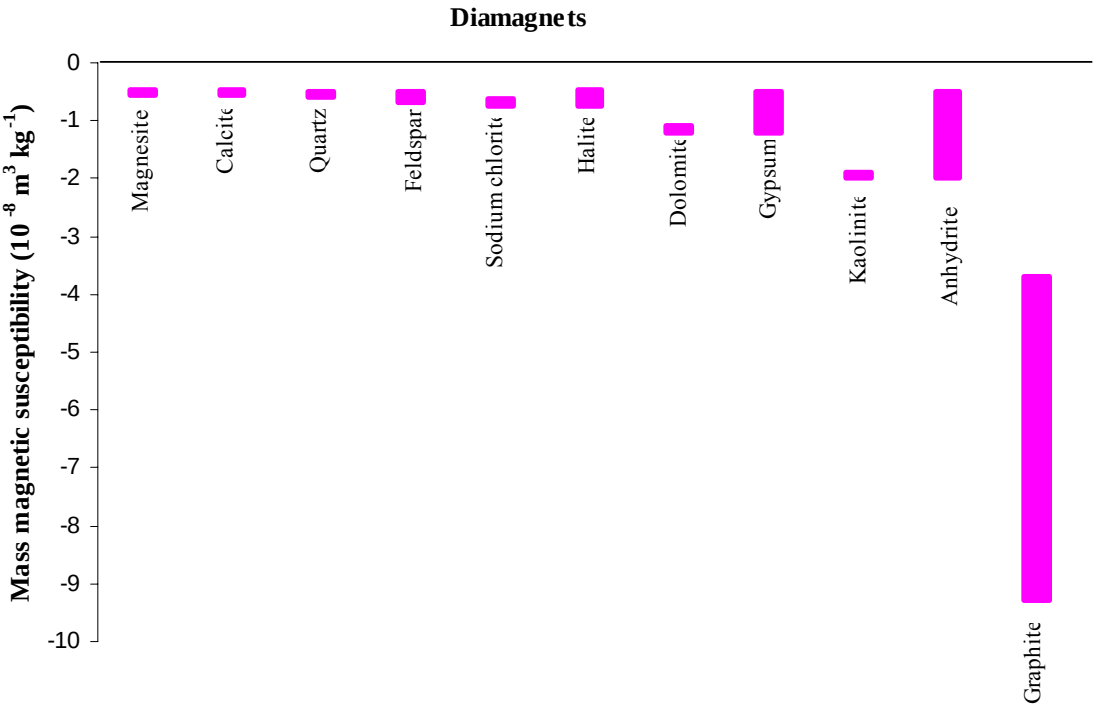

Figure 2.3: The range of initial mass magnetic susceptibility values (quoted by various authors) for diamagnetic minerals related to hydrocarbon reservoirs and their sediment environment. The values for the minerals were taken from Table 2.1.

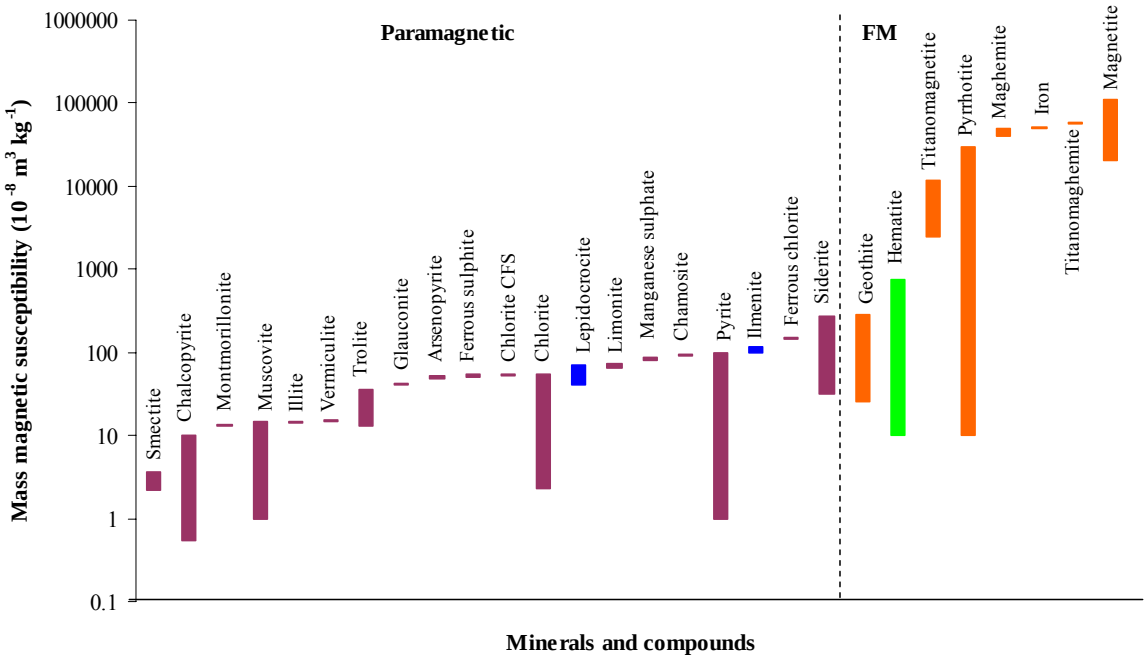

Figure 2.4: The range of initial mass magnetic susceptibility values (quoted by various authors) for ferromagnetic and canted antiferromagnetic minerals related to hydrocarbon reservoirs and their sediment environment. Hematite is a canted antiferromagnetic mineral. The values for the minerals were taken from Tables 2.1 and 2.3, and Mullins (1977), Collinson (1983), Thompson and Oldfield (1986), Hunt et al (1995).

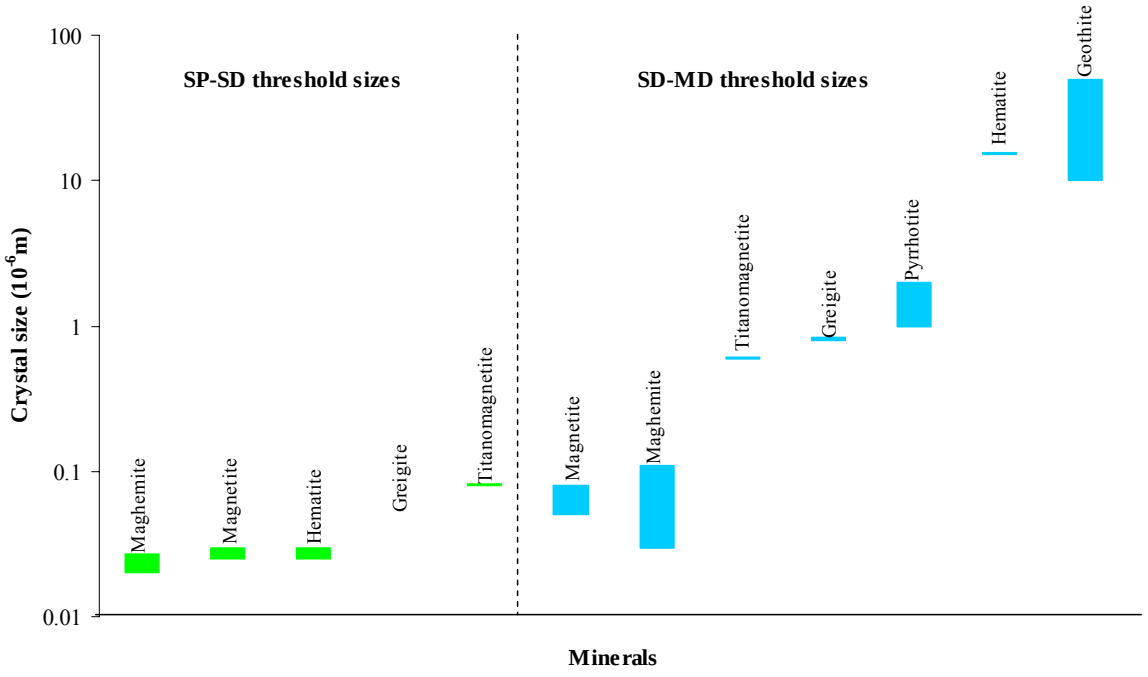

Figure 2.5: SP-SD and SD-MD threshold sizes of ferrimagnetic and canted antiferromagnetic minerals.

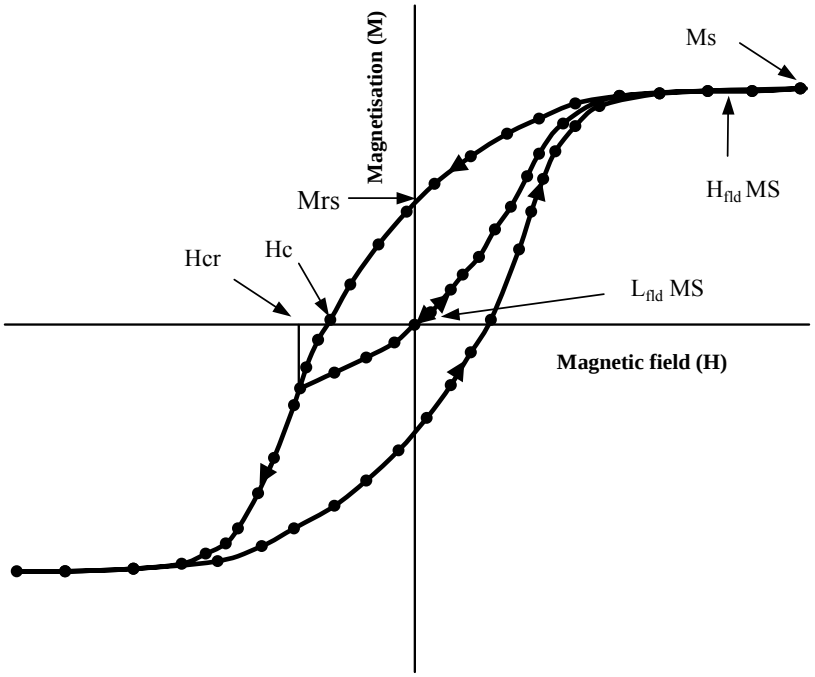

Figure 2.6: Magnetic hysteresis curve of an assemblage of randomly oriented multidomain or single domain ferromagnetic minerals.

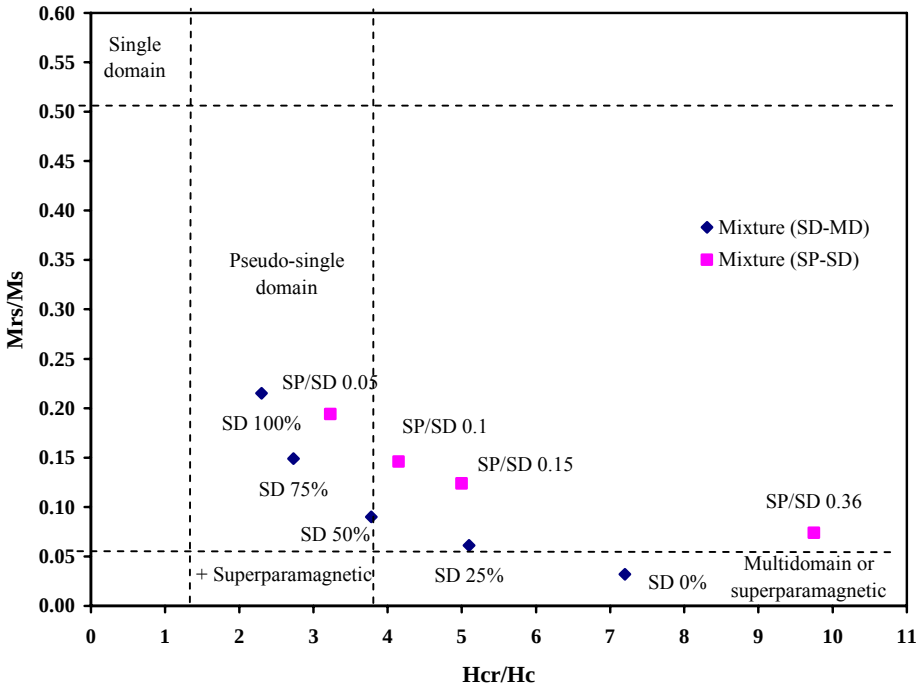

Figure 2.7: Comparison of coercivity (Hcr/Hc) and magnetisation (Mrs/Ms) ratios changes in the domain state of ferromagnetic minerals (after Geiss, 1999). Originally the plot with domain state fields indicated by the dashed lines was used for titanomagnetite samples by Day et al. (1977). In Figure 2.7 various mixtures of single domain (SD) and multidomain (MD), or super-paramagnetic (SP) and SD grains are shown for magnetite.

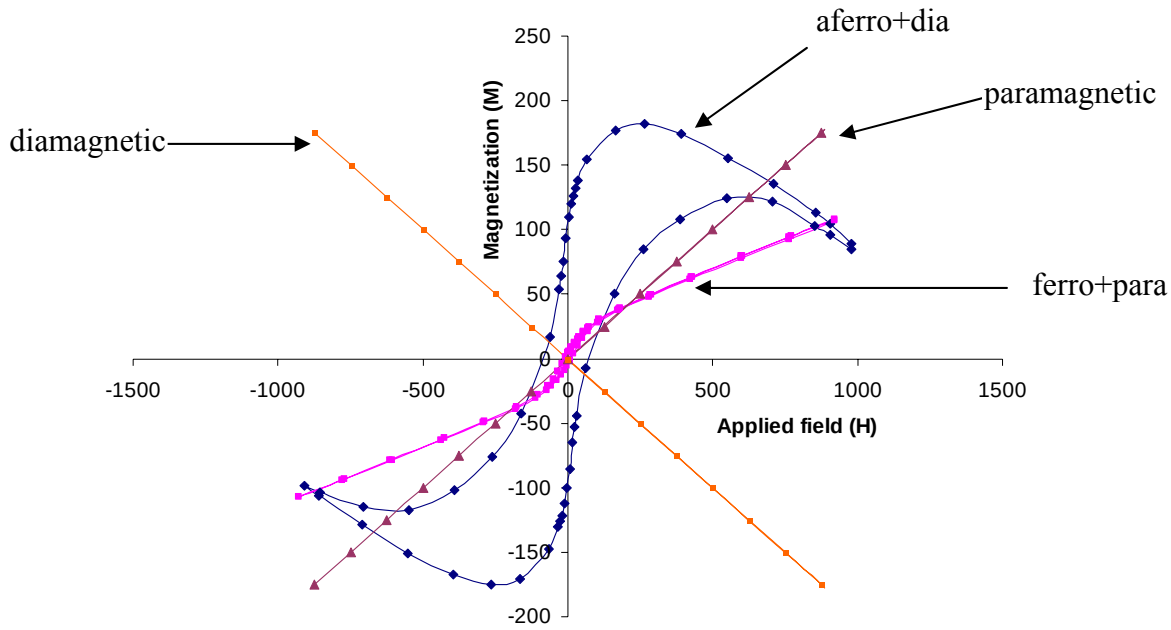

Figure 2.8: Typical hysteresis loops for samples containing combinations of ferromagnetic and paramagnetic minerals (ferro+para), antiferromagnetic and diamagnetic minerals (aferro+dia), and for relatively cleaner paramagnetic and diamagnetic samples.

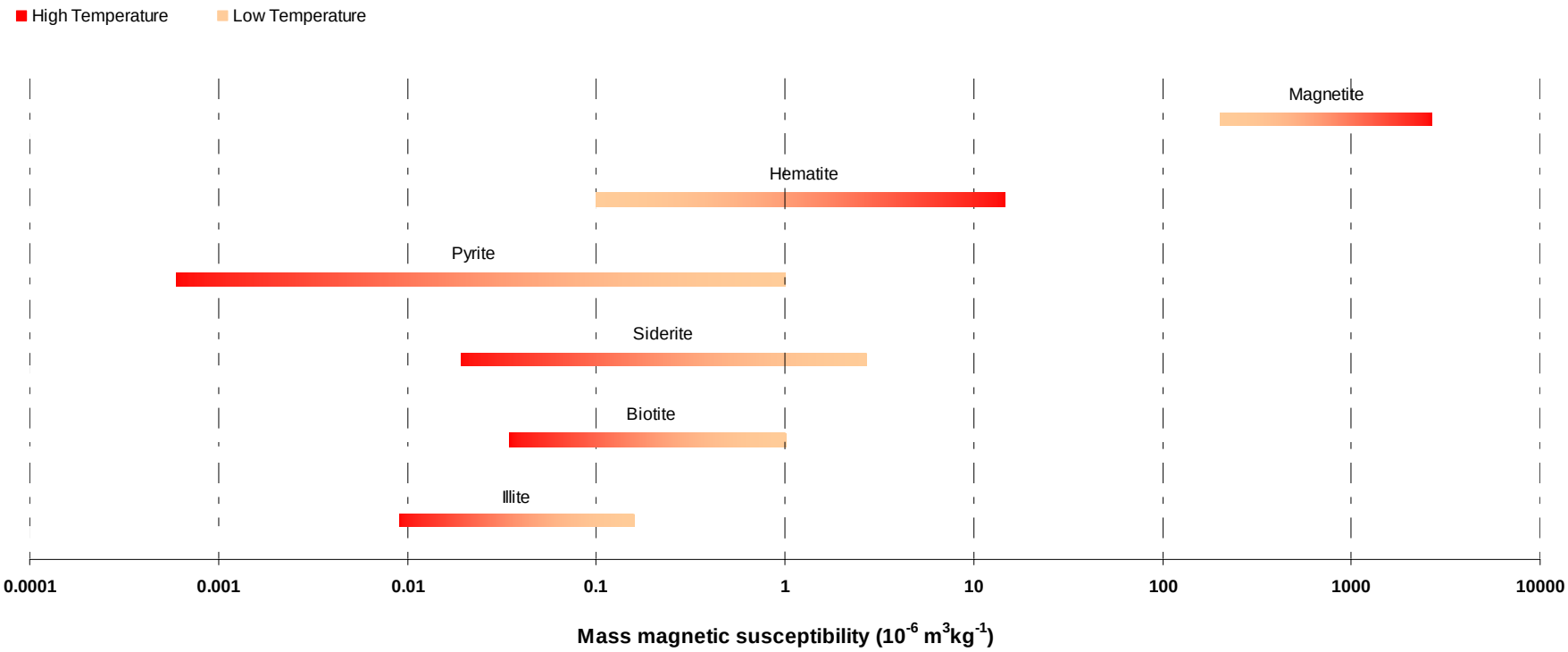

Figure 2.9: Theoretically calculated magnetic susceptibility values for different reservoir minerals at temperatures 20-330 ^{o}C using Curie-Weiss law. Room temperature magnetic susceptibility values are taken from Tables 2.1 and 2.2. The high temperature susceptibility values are given in Table 2.5.

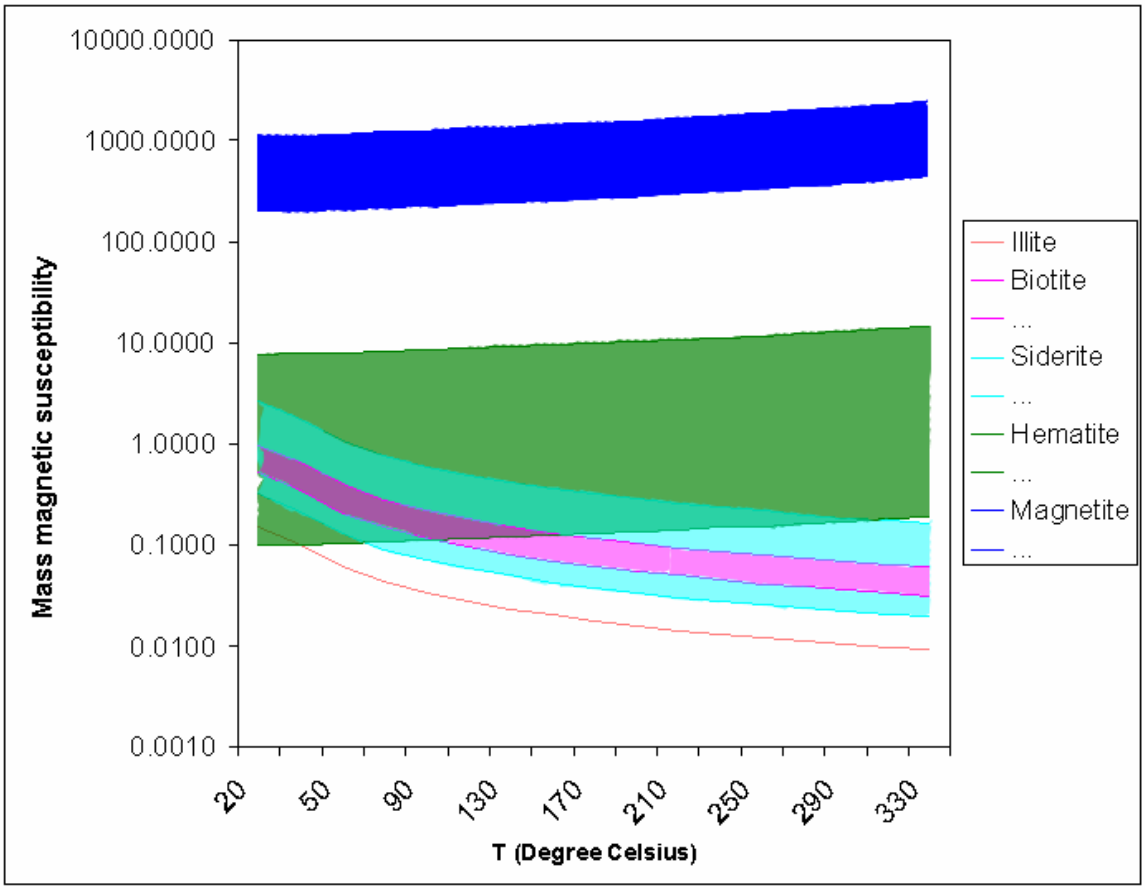

Figure 2.10: Temperature-susceptibility values of Table 2.5 on a logarithmic scale. Mass magnetic susceptibility initially increases with an increase in temperature for hematite and magnetite indicating that these minerals are antiferromagnetic and ferromagnetic respectively. The susceptibility however decreases for paramagnetic minerals like illite, biotite and siderite.

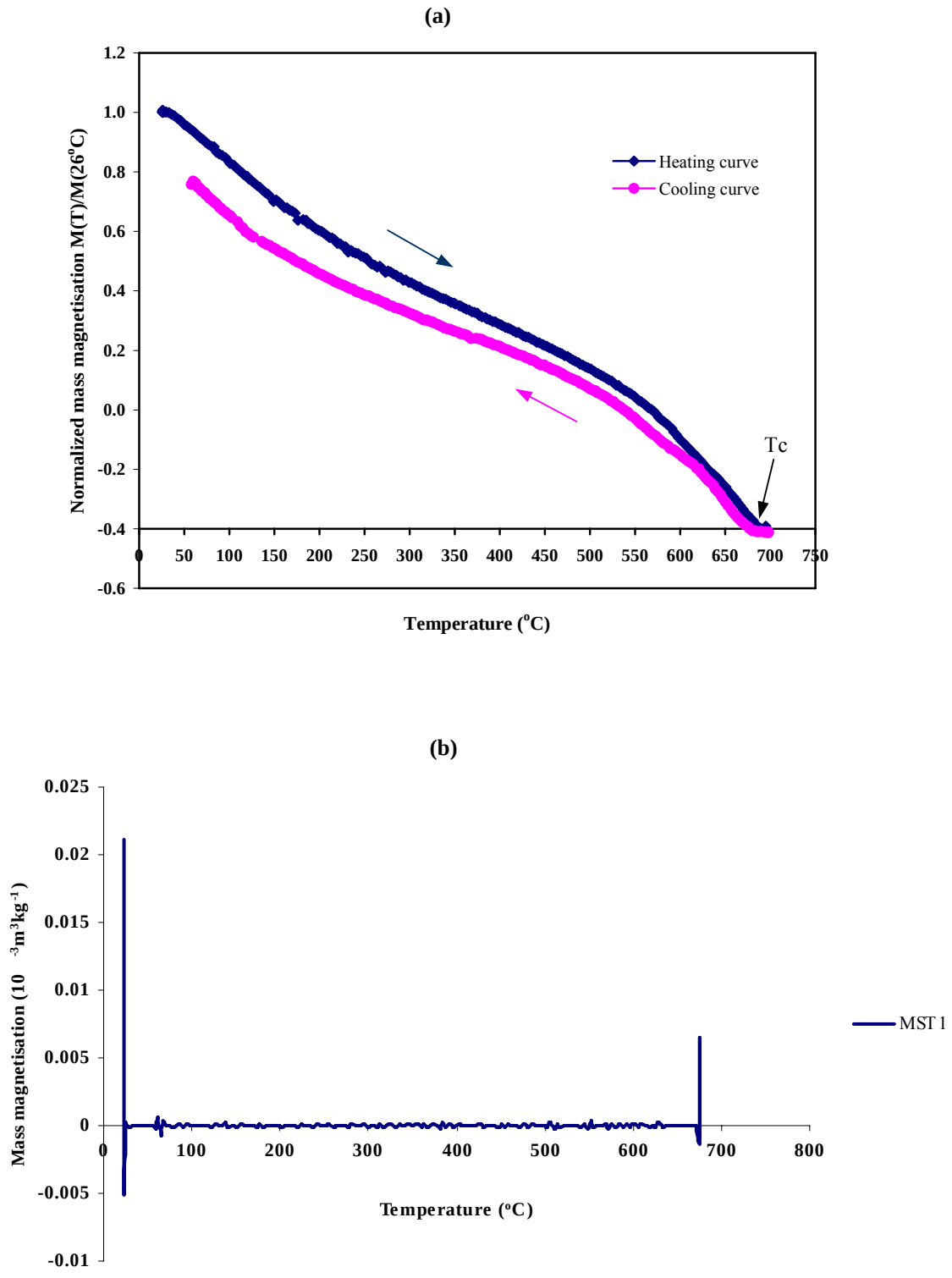

Figure 2.11: Experimental thermomagnetic curves measured for hematite sample MST1. (a) Shows the magnetisation measured during heating and cooling runs. (b) Plot of the 2nd derivative of the magnetization values of Figure 2.11(a) versus applied field.

Chapter 3

System Modelling and Testing of the Downhole Magnetic Susceptibility Measurement System

3.1 Introduction

This chapter focuses on the system modelling and testing of a prototype magnetic susceptibility sonde system for wireline logging applications. The working principle of the sonde is explained with the help of mathematical equations in this chapter. A detailed mathematical analysis is also carried out to understand the variations in magnetic susceptibility within the formation material, and how these subtle variations are picked up by the magnetic susceptibility sonde. Further on, the design aspects of various parts of the sonde are explained in this chapter. It involves the mechanical system design, electronic circuit design, coil system design, and shielding the measurement system from the borehole environment. The type of output interface and the format of the output signal are also explained. The new susceptibility sonde promises to increase the competitive advantage over existing logging tools and to open new business markets and opportunities.

3.2 Literature review

Majority of the magnetic susceptibility measuring systems developed to date are laboratory based. For simplicity, I divide these systems into three main groups. The most prevalent methods are the Gouy balance, Evans balance and the Faraday method (Vulfson, 1998). The second group of methods is based on induction principles. These involve measurements of the electromotive force produced by a vibrating sample, or the inductance of a coil after the sample is inserted into it. Methods based on the analysis of chemical shift in nuclear magnetic resonance (NMR) belong to the third group. The details of each method can be found in the literature (Selwood, 1956; Collinson, 1983; Ergin, 1983; Vulfson, 1998).

There have been developments over time where companies have produced magnetic susceptibility measuring tools for downhole logging operations. Such systems induce a very low intensity magnetic field into the formation material which causes the magnetic minerals (if any) within the formation to respond. This gives the value of total

magnetic susceptibility for that particular piece of rock. These systems have so far been used in mineral exploration, in particular detecting the presence of magnetite in earth ores.

The prototype magnetic susceptibility logging system designed by Simplec faced problems like low amplitude system drift in terms of borehole diameter and coil temperature variations (David et al 1981). A redesign of the Simplec system faced high frequency noise issues (James et al 1981). One of the limitations of such tools is that they have much smaller diameter and hence cannot be used in bigger diameter boreholes used in hydrocarbon exploration. They are also less sensitive to low susceptibility paramagnetic/diamagnetic minerals and are mainly used for identifying the presence of ferromagnetic minerals.

Therefore one of the main aims of this chapter is to detail the system modeling and testing of the prototype magnetic susceptibility sonde for taking susceptibility measurements in-situ downhole. It should have potential to be scaled up for use in larger diameter boreholes. It should also be sensitive enough to detect the presence of low susceptibility paramagnetic and negative susceptibility diamagnetic minerals in the formation material.

3.3 Operating principle of the new magnetic susceptibility sonde

Rewriting the permeability equation 2.4, we get

$$\mu_r = \mu_0 + \mu_0 \chi \tag{3.1}$$

where

μ_r (or B/H) is the relative permeability of the specimen (dimensionless)

χ (or M/H) is the magnetic susceptibility of the specimen (dimensionless)

Further re-arrangement, we get

$$\mu_0 \chi = \mu_r - \mu_0 \tag{3.2}$$

The schematic of the prototype magnetic susceptibility sonde is shown in Figure 3.1. It consists of a field generating or transmitter coil and a compensated pick-up coil. The

sonde uses a very high thermal stability oscillator which excites the transmitter coil. The oscillator is embedded on to the printed circuit board (PCB). The flux is induced in the pick-up coil as a result of transmitter energisation. The frequency of the induced signal represents the susceptibility of the sample surrounding the coil section of the sonde. We will see in Section 3.3.1 (mathematically modeling of the sonde system) that when the sonde is placed inside a borehole, the frequency of the output signal changes as a result of a change in permeability of the material surrounding the sonde. The reference signal of the sonde is noted when held in air. In this case, the permeability of air (μ_0) determines the susceptibility signal. The electronic circuitry used in the sonde computes the difference ($\mu - \mu_0$), digitizes it and passes it to the personal computer on the surface for interpretation purposes. Any voltage off sets as a result of an increase in temperature are compensated out by the sonde electronics.

As mentioned in Section 1.3 **Chapter 1**, the output from the pick-up coil consists of a composite signal: a primary voltage induced by the primary magnetic field as a result of direct coupling between the transmitter and the pick-up coils; and a secondary voltage induced by the secondary magnetic field which is a combination of the magnetic susceptibility of the formation material and the formation eddy currents. The primary voltage is at 0^0 in phase whilst the secondary voltage is at 90^0 (quadrature phase component) out of phase with respect to the primary magnetic field. The received signal is therefore separated into these two components. The in-phase component is often being cancelled out by the use of compensated coil system. The quadrature phase component is a function of both the electrical conductivity σ (representative of eddy currents) and magnetic susceptibility χ of the formation. The electronics designed and embedded inside the susceptibility sonde filters out the magnetic susceptibility signal by suppressing the conductivity signal.

3.3.1 A detailed mathematical analysis of the susceptibility measurement system

Whilst carrying out magnetic susceptibility measurements downhole, the sonde makes a closed magnetic path among the coils, the formation material located in the immediate vicinity of the coils, and the air gap between the coils and the formation. According to Ampere's law, the magnetizing force H of a closed magnetic path is given by the following equation.

$$H \times l = Ni \tag{3.3}$$

where ' H ' is the magnetizing force, 'l' is the length of the closed magnetic path, ' N ' is the number of turns on the core and 'i' is the amount of current flowing through the core windings. For the sonde system, the above equation will become as

$$H_c l_c + H_f l_f + H_g l_g = Ni \tag{3.4}$$

where subscript 'c' represents the core on which the coils are wound, 'f' represents the formation and 'g' represents the air gap.

According to Ampere's law, the relationship between the magnetic flux density 'B' and the magnetising force ' H ' is given by the formula

$$B = \mu H \tag{3.5}$$

where

$$\mu = \mu_m \mu_0 \tag{3.6}$$

μ_m represents the permeability of the core material and μ_0 represents the permeability of free space. Substituting equation 3.6 into equation 3.5, we get

$$B = \mu_m \mu_0 H \tag{3.7}$$

The relationship between the magnetic flux 'φ' and the magnetic flux density 'B' is given by the formula,

$$\varphi = BA \tag{3.8}$$

where A is the area of the closed magnetic path between the transmitter and receiver coils, and the formation material. Equation 3.8 can also be written as,

$$B = \frac{\varphi}{A}$$

Substituting this into equation 3.7, we get

$$\frac{\varphi}{A} = \mu_m \mu_0 H$$

or

$$H = \frac{\varphi}{\mu_m \mu_0 A} \tag{3.9}$$

Equation 3.9 shows another form of equation 3.5 and can be rewritten separately for each of the core, the formation material and the air gap. For example, for the core it will become as

$$H_c = \frac{\varphi_c}{\mu_c \mu_0 A_c} \tag{3.10}$$

where,

H_c is the magnetic field intensity of the core material

φ_c is the amount of flux passing through the core

A_c is the area of the core

μ_c is the permeability of the core and

μ_0 is the permeability of free space

Similarly, for the formation and air-gap, equation 3.9 will take the form as

$$H_f = \frac{\varphi_f}{\mu_f \mu_0 A_f} \tag{3.11}$$

$$H_g = \frac{\varphi_g}{\mu_g \mu_0 A_g} \tag{3.12}$$

Since the sonde makes a closed magnetic path, a uniform magnetic flux 'φ' will flow through the path. That is

$$\varphi_c = \varphi_f = \varphi_g = \varphi$$

Substituting these values into equations 3.10, 3.11 and 3.12, we get

$$H_c = \frac{\varphi}{\mu_c \mu_0 A_c} \tag{3.13}$$

$$H_f = \frac{\varphi}{\mu_f \mu_0 A_f} \tag{3.14}$$

$$H_g = \frac{\varphi}{\mu_0 A_g} \quad (\mu_g = 1 \text{ i.e. permeability of air}) \tag{3.15}$$

Substituting equations 3.13-3.15 into equation 3.4, we get

$$(\frac{\varphi}{\mu_c \mu_0 A_c}) l_c + (\frac{\varphi}{\mu_f \mu_0 A_f}) l_f + (\frac{\varphi}{\mu_0 A_g}) l_g = Ni$$

or

$$\varphi \left[\frac{l_c}{\mu_c \mu_0 A_c} + \frac{l_f}{\mu_f \mu_0 A_f} + \frac{l_g}{\mu_0 A_g}\right] = Ni \tag{3.16}$$

where

$$\frac{l_c}{\mu_c \mu_0 A_c} = \Re_c \tag{3.17}$$

$$\frac{l_f}{\mu_f \mu_0 A_f} = \Re_f \tag{3.18}$$

$$\frac{l_g}{\mu_0 A_g} = \Re_g \tag{3.19}$$

$\Re_c, \Re_f$ and $\Re_g$ represent the reluctances of the core, the formation and the air-gap respectively. Therefore, equation 3.16 will take the form as

$$\varphi \left[\Re_c + \Re_f + \Re_g \right] = Ni \tag{3.20}$$

We know that an increase in resistance in electrical circuits reduces the amount of current flowing through the circuit. Similarly, an increase in reluctance in the magnetic circuits reduces the amount of flux through them. The area (A_c) and path length (l_c) of the core material will be constant. For the air gap, A_g and l_g will also stay the same unless there are some washouts in the borehole. However any washouts can be easily picked up by a large spike in the magnetic signal; and/or from a caliper log. This will make $\Re_c$ and $\Re_g$ constant in normal conditions of sonde operation. However, any

presence of paramagnetic and/or ferromagnetic minerals in the formation will change the permeability of the formation material (μ_f) and hence $\Re_f$ will change. A change in reluctance $\Re_f$ will change the amount of flux flowing through the formation material thus affecting the magnetic coupling between the transmitter and the pickup coils. This change in magnetic coupling directly corresponds to the magnetic susceptibility (χ) of the formation material.

Another potential use of the mathematical model is that it can provide an approximate indication of the type of minerals present in the formation. For instance, the susceptibility signal of the sonde provides us the amount of flux flowing through the formation material and in turn the permeability of the formation. Provided the formation contains only one type of paramagnetic/ferromagnetic minerals, the permeability derived from the susceptibility signal can provide an indication of the type of minerals present in the formation material.

It is also worth noting that the majority of the reservoir fluids (i.e formation/drilling fluids) are diamagnetic. They posses very low values of magnetic susceptibilities and hence do not have much impact on sonde output (Ergin et al 1975). Likewise, the short-term changes in earth's magnetic field and/or the magnetic field of the drill string are too small to affect the sonde output (Ergin and Yarulin, 1979).

3.4 Design aspects of the magnetic susceptibility sonde

The schematic of the prototype magnetic susceptibility sonde showing the sonde mechanics and the connections among various electronic modules is shown in Figure 3.1. From the figure, the prototype sonde consists of an aluminium cylinder containing the printed circuit board (PCB). The coil section is placed inside a non-magnetic polyvinylchloride (PVC) tube. The coil terminals are passed to the PCB for electrical connection between the coils and the PCB. A custom made adapter shown in Figure 3.1 and by illustration 3.1 is used to connect the sonde to the wireline.

I have used silicon oil in the sonde which surrounds the coil section in order to reduce the thermal effects on output voltage drift. The silicon oil acts the same way as used for pressure equalization in aeroplanes. To keep the pressure and temperature at normal conditions inside the planes, the pressure on the inner walls of the planes is exerted such that it becomes equal to the outside air pressure. The silicon oil in the sonde behaves the

same way. When the sonde travels downhole, the silicon oil expands volumetrically with an increase in the temperature until the pressure on the inner walls of the sonde and the outside formation pressure is equalized.

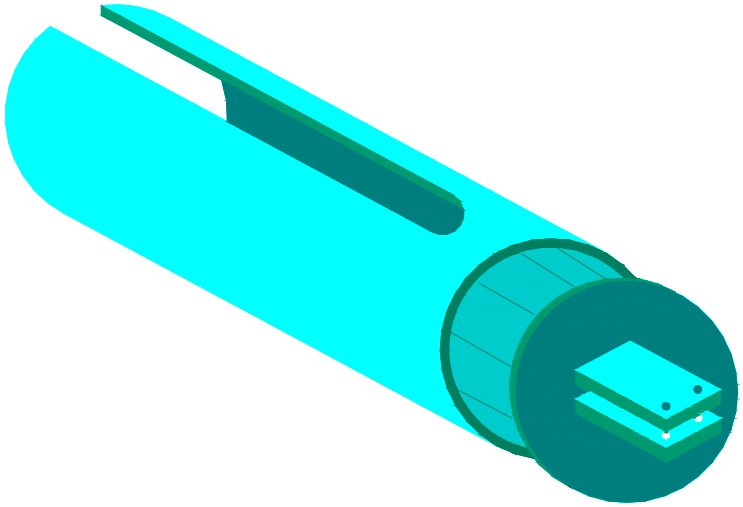

Illustration 3.1: CAD diagram of the custom made hollow adaptor used to connect the sonde to the wireline.

The finished prototype of the magnetic susceptibility sonde is shown in Figure 3.2. The sonde has a 43 mm external diameter and can be used to depths of around 4000 meters. The operating frequency of the sonde is kept quite low to reduce the effect of eddy currents which are produced as a result of formation conductivity. The coil section has a vertical full-width-half-maximum (F.W.H.M) response of 140 mm and the logging is carried out at a rate of 5 per second giving a theoretical maximum logging rate of 140 × 5 mm per second (0.7 m per second). The sonde is calibrated for operation in 44.5 mm diameter boreholes. However the prototype is being modified for use in larger diameter boreholes.

3.4.1 Coil system design

There is a vast range of techniques which can be used to design the coil system for the magnetic susceptibility sonde and can be based on either:

- Detecting the magnetic flux change caused by the sample by measuring the voltage induced in the pick-up coil.

- Measuring the dipole field of a magnetized specimen or the corresponding flux changes by using superconducting quantum interference device (SQUID).
- Measuring the forces exerted on a magnetized sample in an inhomogeneous (or gradient) magnetic field.
- Measuring the torque exerted by a magnetized sample in a homogeneous magnetic field.

While these methods are fairly straightforward to implement in stationary fields, difficulties arise in case of time varying fields. This is because severe restrictions are posed by the experimental boundary conditions, the most critical of which is the poor signal to noise (S/N) ratio. Taking these factors into consideration, the most convenient and appropriate method for use in the sonde system is by using a pick-up coil system.

In Figure 3.1, a transmitter coil and a compensated pick-up coil are wound on a hollow non-magnetic cylinder with an inner diameter of 39 mm and outer diameter of 41 mm. The compensated pick-up coil can take the form of axial, radial and coaxial types. The compensation of the latter two can be implemented either in the usual form (i.e. a transmitter coil and a compensation coil) or by winding the turns alternatively in opposite directions. For the system shown in Figure 3.1, I have used an axial pick-up coil made up of turns of thin wire wound in opposite directions. The length of the solenoid is around 35 mm for each of the transmitter and pick-up coils. This makes the sensor coil section of the sonde around 100 mm long (there is a 30 mm spacing between the coils). The coil's response in the sonde system is exactly described by the considerations of mathematical equations mentioned in Section 3.3.1; as well as feed through wires to transmit the signal to the recording device (a personal computer in this case).

The compensated coil system is based on a very common principle: measuring the voltage in a pick-up coil induced by a transmitter coil in a varying magnetic field. The transmitter coil of the prototype magnetic susceptibility sonde generates a magnetic field of around 10 mT. The pick-up coil, in principle, measures the time derivative of the enclosed flux using the equation

$$\Phi = \int_F B dF \tag{3.21}$$

Assuming a location-independent time dependence, the following equation

$$U_{ind}(t) = -\frac{d\Phi}{dt} = \tilde{\alpha}\frac{dB(t)}{dt} = \tilde{\beta}\left(\frac{dM(t)}{dt}\right) + \tilde{\gamma}\left(\frac{dH(t)}{dt}\right) \tag{3.22}$$

holds true for the induced voltage $U_{ind}(t)$. The coefficients $\tilde{\beta}$ and $\tilde{\gamma}$ describe the coupling of the flux of sample ($\leftrightarrow$M(r)) and field ($\leftrightarrow$H(r)) respectively to the pick-up coil. Knowing the coefficients $\tilde{\beta}$, $\tilde{\gamma}$ and dH/dt, the magnetization M (which essentially represents the magnetic susceptibility of the sample under test), can be determined from the induced voltage $U_{ind}(t)$ in the pick-up coil. Since one is only interested in the magnetization signal, which is often small compared to that of the primary field, it is advantageous to have coils with $\tilde{\gamma} << \tilde{\beta}$, or preferably $\tilde{\gamma} = 0$. This is realized by the compensated coil system where the flux of the transmitter coil is just cancelled out, i.e. $\tilde{\gamma} = 0$.

Although the flux of the transmitting field is cancelled out, the existing field gradients may still lead to a non-compensated net flux. Therefore this type of coil system acts as a gradiometer probing the gradient of the background field along a particular direction. And of course, a more detailed analysis of these coils can be extended with respect to higher order derivatives of the field. However, in our case, the application of this compensated coil permits to obtain sufficiently well resolved magnetization data in order to achieve the required dynamic range and resolution for the sonde. Also, the subsequent subtraction of the component related to the exciting field introduces always an error. Assuming $\tilde{\gamma} = 0$ for well-compensated pick-up coils, the magnetization is then given by the expression

$$M(t) = \frac{1}{\tilde{\beta}}\int_{t_0}^{t} U_{ind}(t')dt' + M_0 \tag{3.23}$$

Where M_0 is the initial magnetization at t_0. The results for magnetization M are obtained by subtracting signals obtained with and without sample.

3.4.1.1 Operating frequency and coil spacing

The sonde resolution and its depth of investigation (how deep the sonde looks into the formation) depends on the operating frequency of the oscillator and on the spacing between the transmitter and the pick-up coils. The larger the spacing between the coils, the higher will be the depth of investigation (also called skin depth). Since frequency is inversely proportional to skin depth (S), the operating frequency of the transmitter will also have to be kept low in order to achieve these higher depths of investigation. The lower frequency would also help generate less eddy currents within the formation material and therefore would aid the susceptibility signal to overcome on conductivity effects.

Immunity to errors arising due to conductivity ($1/\rho$) can be demonstrated by reference to skin depth, which is also defined as the depth of penetration of the alternating magnetic field for which the flux is attenuated to $1/e = (0.37)$.

$$S = \sqrt{2\rho/\omega\mu} \tag{3.24}$$

where ω is the operating frequency of the sonde. I have used an operating frequency of 1.4 kHz for our sonde system shown in Figure 3.1.

On the other hand, a smaller spacing between the transmitter and pick-up coils would mean lower depth of investigation but higher resolution. The oscillator frequency will have to be increased accordingly due to a smaller spacing between the coils. The spacing between the coils should however be greater than half the wavelength of the oscillator frequency ($\lambda/2$), otherwise the pick-up coil will not see much of the flux induced by the transmitter coil and the formation material. The higher frequency means more eddy currents are generated within the formation material. Therefore there should be a trade off between the depth of investigation and the resolution of the sonde. I have created a 30 mm spacing between the coils which gives sufficient depth of investigation (approx. 35mm) without compromising much on the resolution itself. This is because the higher resolution is one of the key advantages of the magnetic susceptibility sonde over existing logging tools.

The aspect ratio (w/d) between axial width w and inner diameter d of the coils is chosen to reach both, a reasonable high current density and a low inductance at the same time.

The current density increases with decreasing axial width, whereas the inductance diminishes with increasing axial width. Since both aims cannot be achieved at the same time, a compromise has to be made so that the aspect ratio is generally on the order of 1. A minimum acceptable value will be fixed by demands on the field homogeneity. The coils used in the sonde system have an aspect ratio of w/d = 1:1.

3.4.2 Design of sonde electronics

In this section, I provide a step by step design of the electronic circuit for the magnetic susceptibility sonde system (Figures 3.3 - 3.5). The transmitter coil and its associated electronics are shown in Figure 3.3. The transmitter is energized by a simple crystal oscillator circuit oscillating at a frequency of 1.4 kHz. When the switch S1 is closed, an instantaneous voltage is built-up across the transmitter windings. This causes the current to flow through the transmitter whose magnitude is limited by the resistance of the transmitter coil. Inductors (such as the transmitter coil) resist changes in the current flowing through them. Any change in current generates a voltage across the coil which opposes the change. Now if the switch S1 is opened, the current flowing through the transmitter will drop. To oppose the drop in current, the transmitter coil will generate an instantaneous voltage (sometimes in the form of large voltage spikes) across its windings. Such instantaneous voltage can damage the electronic components. To resolve this, a diode D1 is connected across the transmitter in reverse-biased mode as shown in Figure 3.3. The diode used in this way is called a flywheel diode. The reverse breakdown voltage of the diode is 50V. When the switch is opened, the current in the transmitter coil flows through the diode thus safely reducing the instantaneous voltage. It is important to note that I have also used a parallel combination of resistors r1 & r2 to limit the amount of current flowing through the transmitter coil.

The compensated pick-up coil along with its associated electronics is shown in Figure 3.5a. The coil picks up the induced voltage from the transmitter, amplifies it and converts it into a variable frequency pulse signal for the implanted electronics. The design procedure for the transmitter and pick-up coil system is already discussed in Section 3.4.1. Here I will mainly concentrate on the processing of the magnetic susceptibility signal.

3.4.2.1 Voltage regulators

In Figure 3.5a, a +15V regulated dc power supply is used to supply power to the sonde. The voltage is stepped down to +5V and +12V by the use of voltage regulator IC's (IC5 and IC6). The two regulator IC's have been used to separately supply power to the amplifier circuit and to the signal processing circuit. If a single power supply is used, its output is destabilized during magnetic induction within the receiver coil. This happens due to the transient flow of current through the receiver coil. The voltage regulators solve this problem. In this particular case, the signal amplifier circuit is supplied power from IC6 whereas IC5 supplies power to the rest of the surface mount components.

3.4.2.2 Signal amplification and filtering

At the pick-up coil, the amplitude of the output signal is not large enough to be processed by the electronic circuitry. To record the output, very high first stage gains are required with a good signal to noise ratio (SNR). Cascading amplifiers are not optimum since the signal will soon saturate due to various voltage drifts, offsets, and errors, including non-linearities and gain errors. Further accumulated error artifacts can have much larger amplitude than the signal itself. Hence, the maximum attainable gain and the SNR will depend on the real time control accuracy that we have over the offset and gain correction to prevent signal saturation.

For signal amplification, I have introduced an operational amplifier shown by IC1 in Figure 3.5a. This is an independent high gain dual BiCMOS operational amplifier optimized and fully specified for +3V and +5V operation. Nevertheless, in extremely difficult input conditions causing excessive baseline drifts or offsets (e. g. extremely high input impedance electrodes with bad contacts or frictions with the skin), ac coupling will be required prior to the instrumentation amplifiers. This is to avoid saturation problems and to be capable to use a higher pre-amplification value without causing saturation, and hence maximizing the signal to noise ratio. The amplified sinusoidal output is fed to the signal processing stage.

A programmable band pass filter shown in Figure 3.4 is used at the output of the signal amplification IC1 in Figure 3.5a. Band pass filtering is performed to remove high frequency noise produced during transmitter magnetizations; and also to remove DC offset as early as possible since the following high gain amplifier (IC22) may add offset

which can lead into channel saturation. For simplicity, the filtering circuit of Figure 3.4 is not shown inside Figure 3.5a.

The general form of a band pass filter is shown in Figure 3.4a. It is a 3-pole Bessel filter with a relatively steeper roll-off. The poles of a filter determine the amount of roll-off in the filter. The roll-off gets steeper and steeper as the number of poles is increased. However, an increase in the number of poles would mean an increase in the size of the filter circuit. I have tested the filter output with various number of poles and finally decided to use a 3-pole filter based on the available space on the circuit board and the required output.

From Figure 3.4a, we can write

$$R = 2 - \frac{1}{\mathrm{Q}} \tag{3.25}$$

$$R1 = R2 = R_{old} = 1\Omega$$

$$C1 = C2 = C_{old} = 1F$$

R_{old} and C_{old} represent the existing values of the resistors and capacitors. Q is called the quality factor of the filter. It provides a certain amount of gain at the filter output. As the resistance R depends on the quality factor Q, its value can simply be changed by changing the value of Q.

The 1Ω resistor is too small to be used in the electronic circuit. It gives high off-set values with temperature variations resulting in an unstable output. Similarly, $1F$ capacitor is too big to be used in a filter to remove high frequency noise. Such capacitors are usually used for low frequency signals (e.g 50 Hz AC signal). To scale the values of resistors and capacitors into realistic component values, the following equations have been used for a 3-pole Bessel filter.

$$R_{new} = K_m R_{old} \tag{3.26}$$

$$C_{new} = \frac{1}{K_m K_f} C_{old} \tag{3.27}$$

where K_m and K_f are called the magnitude scaling and frequency scaling factors of the filter. The factor K_f can be calculated by the following equation.

$$K_f = \frac{\omega_0}{\sigma} \tag{3.28}$$

where ω_0 is the reciprocal of the time constant τ and σ represents the real part of the complex frequency variable of the filter. It gives the location of the 3rd pole on the real axis.

Figure 3.4b shows the band pass Bessel filter with realistic component values. I have taken Q=1 ($R = 0$) to provide a unity gain at the filter output. This is due to the reason that a certain amount of gain has already been provided by IC1 in Figure 3.5a. With $R = 0$, the filter acts as a voltage follower thus providing a unity gain at its output. This filter allows low frequency components (below cut-off frequency f_c) to pass and stops the high frequency noise components (above f_c). The cut-off frequency f_c for the circuit in Figure 3.4b is calculated by the following formula,

$$f_c = \frac{1}{2\pi RC} \tag{3.29}$$

$$= \frac{1}{2 \times 3.14 \times 1 \times 10^3 \times 47 \times 10^{-9}}$$
$$= 3.38 kH_z$$

This frequency is high enough to pass all the valuable signal information through the filter. The noise frequencies are usually in the range of multiples of kHz and hence will be easily stopped by the filter. Due to extremely high input impedance and the absence of leakage current at the inputs, no saturation is expected to occur at the filter output. The baseline drifts, if any, will typically be removed efficiently with the band pass filter following the first amplification stage. This configuration maintains a maximum Common Mode Rejection Ratio (CMRR) level which is one of the most critical characteristics required to maintain signal integrity.

3.4.2.3 Signal processing

The signal processing stage consists of four IC's: IC2A, IC2B, IC3 and IC4A. IC2A, IC2B and IC4A are retriggerable resettable monostable multivibrators which produce a fixed duration pulse at their output. The duration of the output pulse can be calculated using the formula 0.7 × Rt × Ct and depends on the values of the resistors and capacitors connected to pins 14&15 or 1&2 of these IC's. IC2A is triggered on the positive edge of the input sinusoidal wave coming from the output of the signal amplification stage. It gives the output pulses of width 91μsec with a time period (T) of 0.73msec at test point 2 (TP2) in the circuit. A schematic of the output pulse train (also called clock signal) is shown in illustration 3.2. Although the pulse width is constant, the time period 0.73msec (reciprocal of frequency) is variable which depends on the change in frequency of the pick up coil which ultimately corresponds to the magnetic susceptibility of the sample being analysed.

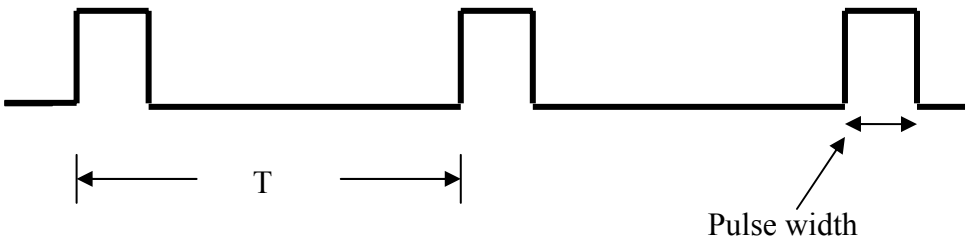

Illustration 3.2: Schematic diagram showing the output pulses from monostable multivibrators and are representative of the magnetic susceptibility signal.

The output from IC2A is fed to IC3 which is a 12-stage high speed binary counter. This device is incremented on the falling edge of the input clock, and all its outputs are reset to a low level by applying logic high on its reset input. The 1.4 kHz pulses are fed to the counter at pin10 whereas pin2 generates an output pulse after counting 32 pulses at its input. This means the counter will generate an output pulse every 32×0.73 msec = 23.36 msec. The counter output stays ON for another 23.36 msec which makes the time period of the output pulses as 46.72 msec (21 Hz). In other words, the counter acts as a divider by 2^6. The division is performed to stabilize the data output coming from the IC2A. This is because at 1.4 kHz frequency, it is very difficult to measure the change in phase, frequency or even the time period of the sample at the output of the pick-up coil. Therefore at test point 3 (TP3), I get pulses of width 23.36 msec and at a frequency of 21 Hz. The remaining two multivibrators (IC2B and IC4A) cut the pulse width down to

0.5 μs at TP4 and to 0.1 μs at TP5 respectively whilst maintaining 46.72 msec time period. TP4 is used to load the data into the shift registers whereas TP5 is used to reset the binary counters explained in the next sub-section.

3.4.2.4 Fixed length timer

IC7 is a low power crystal controlled oscillator that can be externally programmed to operate up to 10 MHz. It has a built-in 32.7 kHz clock at pin5 which is connected to the dual 4-input NAND gate (IC8A). The output of the NAND gate is fed to the counter IC's (IC9 and IC10) which act as dividers for the input 32.7 kHz signal and produce a 47.5 msec impulse signal at the input of IC14. The purpose of the D-type flip flop (IC11) is to divide the output of IC14 by 2 so that I get equally spaced pulses (not impulses) at the output of the flip flop with half the frequency to that of the impulses. The output of the flip-flop goes into the counter IC's (IC12 and IC13) which starts counting these pulses upon receiving the load signal from TP4.

3.4.2.5 Protection diodes

The purpose of the diodes D1, D2, D3 and D4 (Figures 3.5a and 3.5b) is to protect the circuit from any excessive currents. If the signal is between 0 and +5V, there will be no conduction through the diodes. If the voltage goes negative, there will be conduction from the +5V supply to ground. Similarly if the voltage goes beyond +5V, there will be conduction from the circuit terminals to ground. Therefore the diodes will clamp the voltage one diode drop below zero and one diode drop above +5V which is the maximum signal that can flow through these lines, as long as the current flow doesn't damage these diodes. I have put the resistors R13, R14, R15 and R19 in series with diode pairs to protect them against high currents.

3.4.3 Digital and pulse rate output

The sonde provides an output in the form of six wires. The red wire is connected to a +15V power supply and the brown wire is connected to the ground terminal. The three wires (blue, yellow and grey) provide the digital output which is sent to the computer for processing.

3.4.3.1 Digital output

To explain how I get susceptibility data out from the sonde, I summarize below the incidents happening at all the test points (TP's).

TP1: receives 1.4 kHz sine wave coming out from the receiver coil. When the sonde comes across a piece of rock having paramagnetic/ferromagnetic minerals, the induced flux in the pick up coil changes, due to which the frequency of the sine wave changes. This change in frequency is proportional to the magnetic susceptibility of that piece of rock.

TP2: converts the incoming sine wave into 100 μsec duration of fixed width pulses with a variable time period of around 0.73 msec. The time period varies with a variation in the frequency of the sine wave.

TP3: drops the frequency of the input signal down to 21 Hz (47.5 msec). This is done to make the signal more stable and readable in the presence of noise.

TP4: uses pulses of 0.5 μsec width to load the D-type flip flop (IC11). The flip flop passes its data to the counter IC's (IC12 and IC13). These IC's make a 24 bit binary counter, the output of which goes into the shift register IC (IC15). The counter IC's keep counting the input pulses until TP5 sends a reset signal to these IC's. Therefore the data in the counter IC's (and in the shift register) depends on the time period of 0.5 μs pulses. Their time period varies with a variation in the frequency of the input sinusoid. Therefore, the number of pulses in the shift register depends on the frequency of the input sinusoid (a typical value of 1.4 kHz is shown in the circuit of Figure 3.5a). Any variation in the frequency corresponds directly to the magnetic susceptibility signal.

TP5: receives pulses of 0.1 μsec width which reset the binary counter IC's (IC9, IC10, IC12 and IC13). The resetting is performed after the data has been shifted to the shift register.

In summary, pulses at TP4 continue loading up the data into the shift register whereas pulses at TP5 continue resetting the counters. The data in the shift register is transferred out of the sonde at DATA OUT (point 4) in the form of 24-bit binary. However, to transfer this data out, I need to apply an external clock pulse to the shift register at CLK IN (point 3). The READY signal at point 5 indicates at the output that the data is ready to be shifted out and the clock signal at point 3 shifts the data out of the shift register respectively.

3.4.3.2 Pulse rate output

Figure 3.5b shows the remaining electronic circuitry for the sonde which provides the pulse rate output. The point when 0.5 μsec pulse at TP4 loads the data from counter IC's into the shift register, data is also loaded from the counter IC's into IC16 which is a 14-bit CMOS (complimentary metal oxide semiconductor) digital-to-analog converter (DAC). The DAC produces two complementary outputs IOUTA and IOUTB which may be configured for single-end or differential operation. IOUTB is connected to ground whereas IOUTA is fed to the comparator IC (IC20) via load resistor R24. The reference signal at pin17 of the DAC is fed to the amplifier IC19 which acts as a voltage follower. The output of this amplifier is fed to the second input terminal (pin3) of the comparator IC which provides the magnetic susceptibility output in the form of pulses. This type of output is useful in the sense that one can simply attach a frequency meter or a rate meter at the sonde output to determine the magnetic susceptibility. However, in the borehole environment, the surface telemetry system will require 24-bit binary output signal for data interpretation.

3.5 Shielding of the measurement system

When devising a complete measurement system, three strategies may be pursued to achieve a good signal to noise ratio (SNR) and to enable sensitive measurements at all. The first one is to construct the field generator (transmitter coil system in this case) in such a way that any possible or unwanted interference to the measurement system is avoided by shielding the transmitter coil. The second strategy consists in shielding the measurement system (compensated pick-up coils) in such a way that it becomes unsusceptible to any unwanted external interference; and the third is to shield the whole system from temperature and pressure induced stresses. In general, four main mechanisms of interference can be distinguished to any electromagnetic system [Sch91]:

- Galvanic coupling (wiring)
- Capacitive coupling (E-field)
- Magnetic coupling (H-field)
- Radiation coupling (E/H-field)

By means of operating the system freely floating, galvanic coupling to any other system can be safely avoided. However, galvanic coupling within the measurement system may

still occur. The strength of the latter three mechanisms depends much on the actual conditions. Owing to the operating conditions of the sonde with low voltages and low currents, it is unlikely that capacitive and radiation coupling will occur. Also, due to a small amount of magnetic field produced by the transmitter coil, it is less probable that magnetic coupling will play any major role in terms of magnetic interference within the measurement system.

3.6 Conclusions

- The new magnetic susceptibility sonde system modelled and tested in this chapter makes an indirect measurement of the formation permeability by taking into account the magnetic susceptibility signal of the formation material. It can infer key petrophysical parameters at in-situ reservoir temperatures and pressures.

- The sonde induces a time-varying magnetic field (also called primary magnetic field) into the formation material. The strength of the applied magnetic field is increased in the presence of paramagnetic and ferromagnetic minerals, and is decreased in the presence of diamagnetic minerals. Therefore the resulting magnetic field at the pick up coil determines the magnetic susceptibility of the formation material; and to some extent identifies the mineralogy.

- The sonde presents several advantages over conventional wireline logging tools in terms of its resolution, speed of measurement, analysis time etc. It can aid interpretation of image logs and standard wireline gamma ray logs. It also overcomes many limitations present day logging tools have, in particular in shaley formations.

- If used with the gamma ray tool, the susceptibility sonde can be used to provide more accurate information on mineral contents and petrophysical parameters. This is achieved by comparing the magnetic susceptibility signal with the data from the gamma ray tool.

- The sonde would operate at oil or gas reservoir temperatures (up to at least 110 °C) and pressures of around 6000-10000 psi (about 40-70 MPa). It might also be

incorporated in another form of downhole measurements, these being measurements while drilling (MWD) or logging while drilling (LWD).

- Since the laboratory based magnetic susceptibility measurements by other authors have shown strong correlations with fluid permeability (k), the cation exchange capacity per unit pore volume (Q_v), and the flow zone indicator (FZI), this makes downhole in-situ measurements of magnetic susceptibility a strong candidate to become a routine part of a wireline logging string.

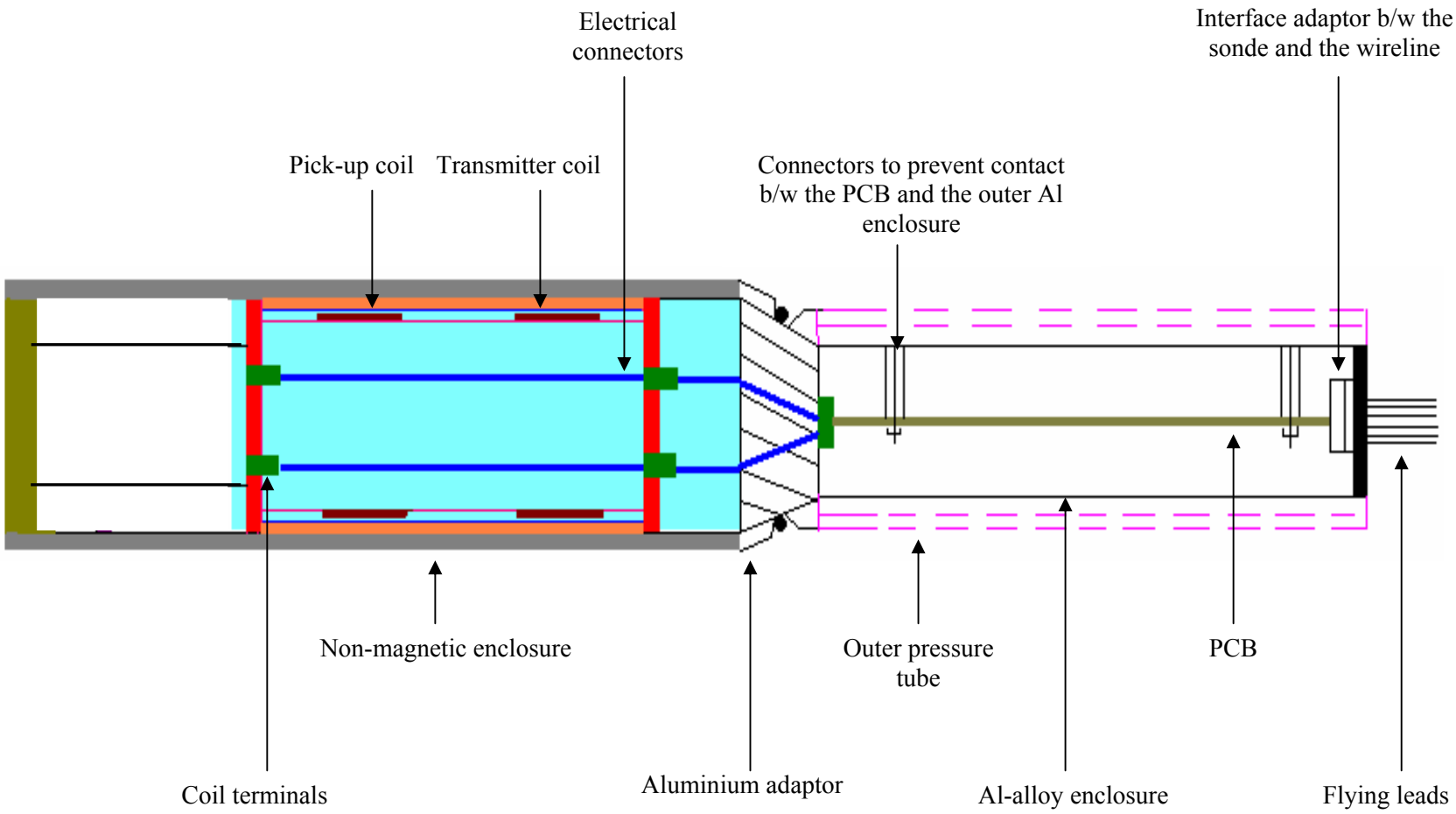

Figure 3.1: A schematic view of the downhole magnetic susceptibility sonde.

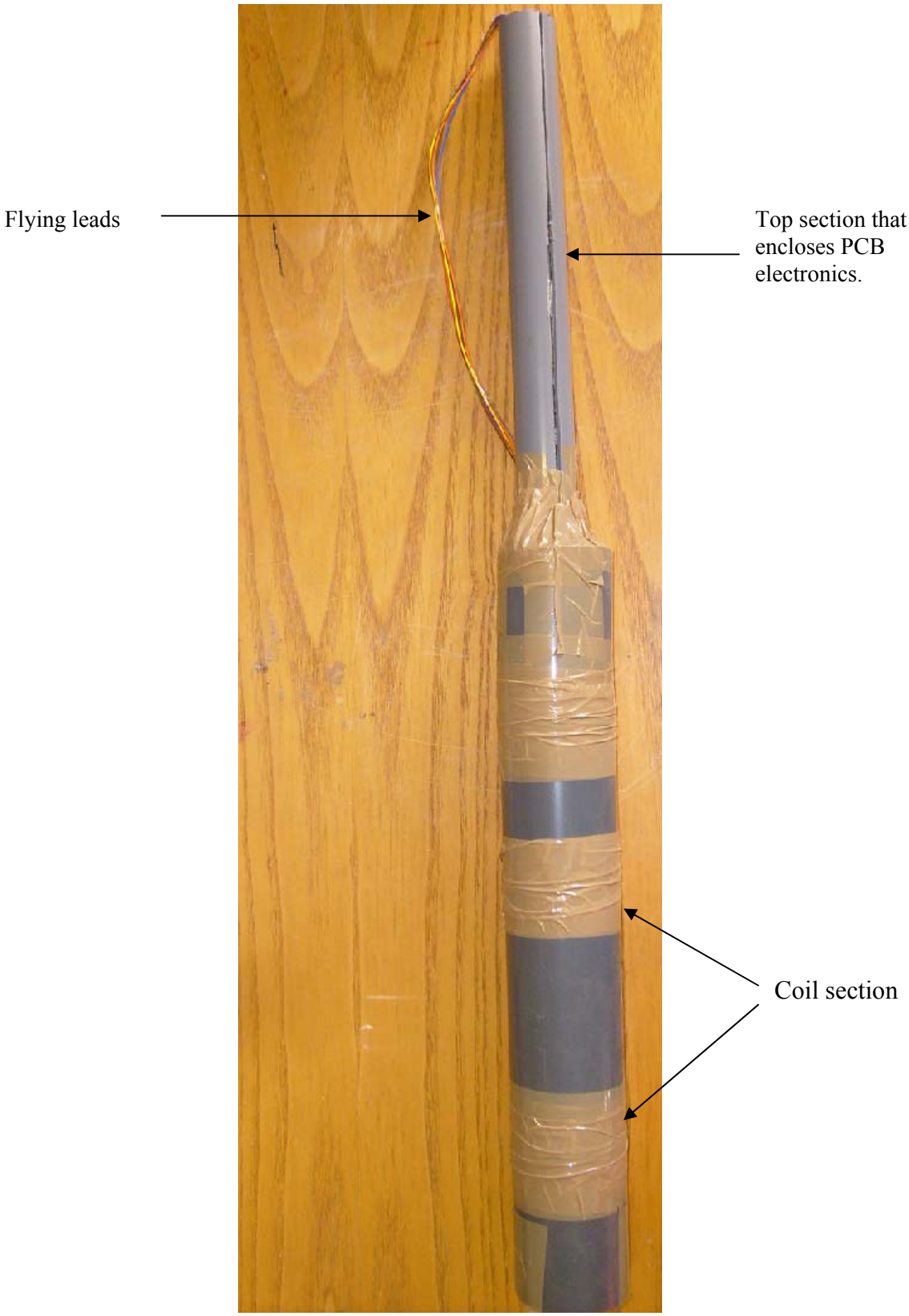

Figure 3.2: Photograph of the prototype magnetic susceptibility sonde.

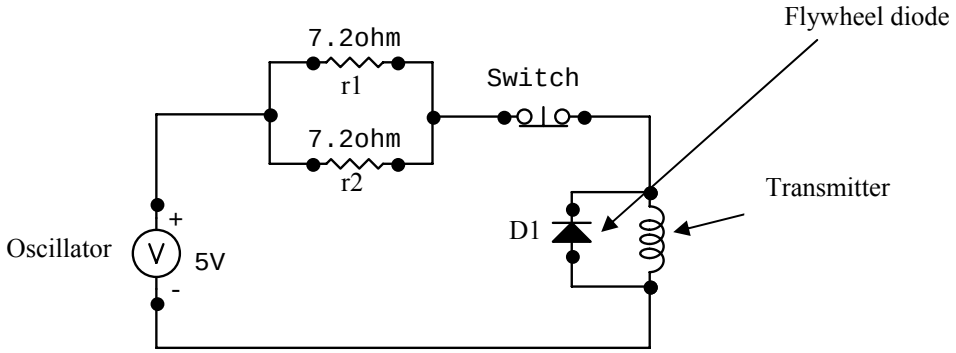

Figure 3.3 Core Drive Circuit with Manual Switching

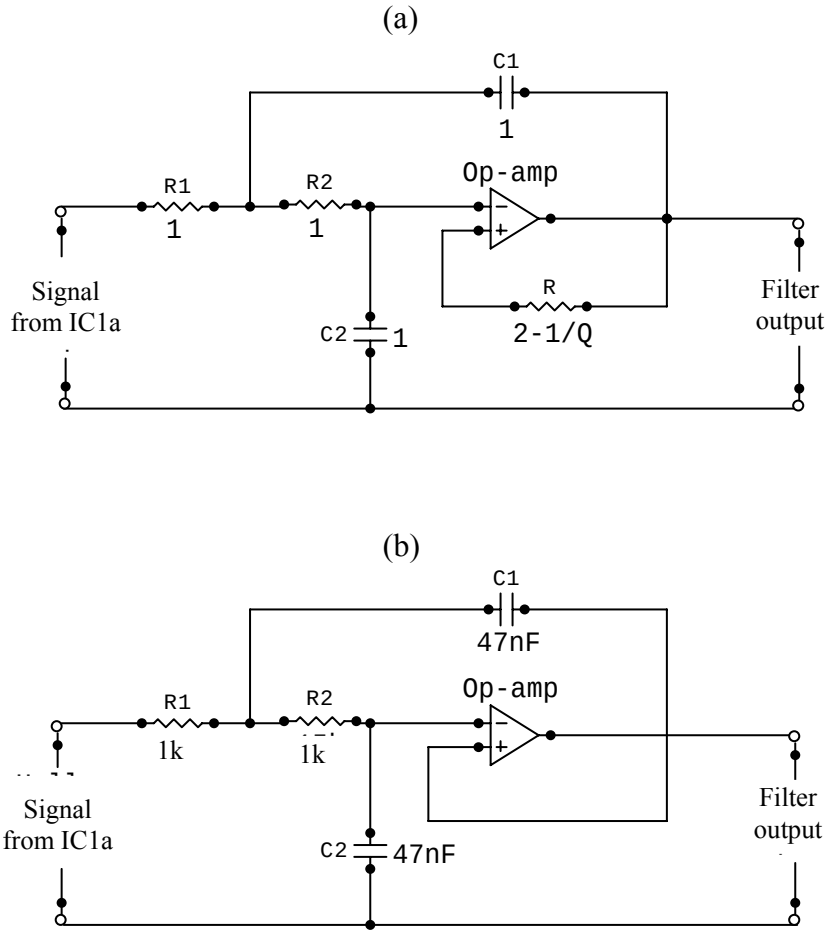

Figure 3.4: (a) General form of a 3-pole Bessel filter (b) Bessel filter with real component values.

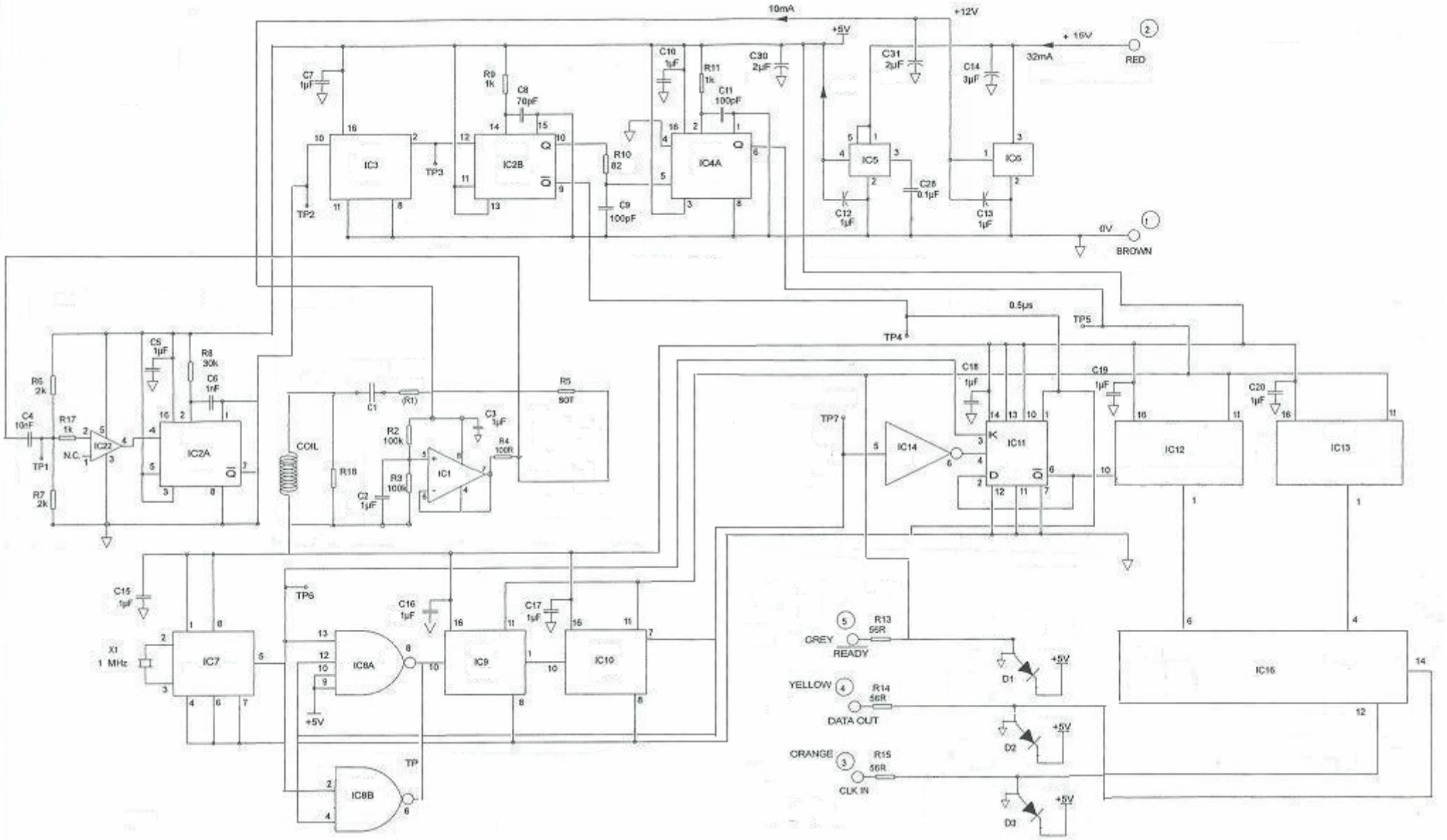

Figure 3.5a: The electronic circuitry for the magnetic susceptibility sonde system for providing binary output.

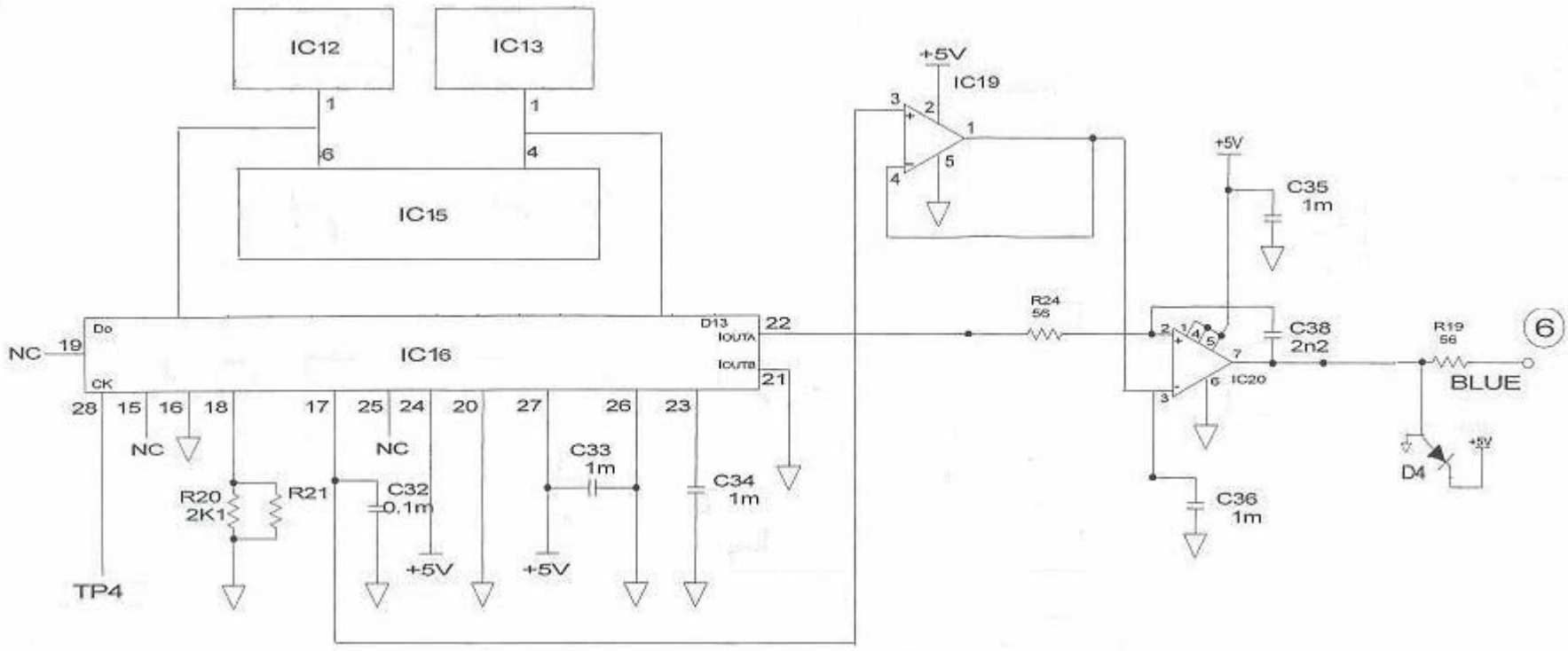

Figure 3.5b: The remaining part of the electronic circuit which provides pulse rate output from the magnetic susceptibility sonde system.

CHAPTER 4

Experimental Setup and Initial Testing of the Sonde

4.1 Introduction

Although many aspects and components of the magnetic susceptibility sonde have been described separately in the previous chapter, the testing of the system as a whole was not documented. Throughout this chapter, various system modules are shown with block diagrams to provide the reader with an idea of how various parts of the susceptibility system (the sonde, the personal computer, and various electronic modules) interact with each other and the complexity involved in the implementation of such systems. The reader will easily understand that the whole operation and interactions among the electronic modules were not easy to simulate. For instance, it would be difficult to determine the impact of modular and intermodular noise on the accuracy achieved in the borehole environment. The impact of such noise will be minor though compared to the amplitude of the susceptibility signal of reservoir minerals.

In this chapter, a list of critical design criteria was compiled for the sonde system, which includes environmental conditions, space constraints, and preferred performance requirements based on the current and future business needs. However, in order to test the performance of the whole system, reference measurements under genuine reservoir conditions should be carried out. This is also the only practicable way to test the electromagnetic shielding as well as the degree of compensation realized under dynamic conditions. In **Chapter 5**, I have carried out magnetic susceptibility measurements on reservoir samples at various reservoir temperatures to model the in-situ downhole conditions.

As an introduction, Section 4.2 detail the connections and test set up between the sonde and other system modules. It also explains how the data is transferred from the sonde to the personal computer. It is followed by Section 4.3 which deals with operating considerations and field calibration of the sonde. Section 4.4 explains various prototype performance experiments carried out in this chapter. Section 4.5 describes the materials used in such experiments. Section 4.6 explains the step by step procedure for making various diameter model boreholes in the laboratory and Section 4.7 detail the prototype performance during experiments on these laboratory made boreholes. Section 4.

shows the effect of an increase in borehole diameter on sonde performance whereas the results are discussed in Section 4.9.

4.2 Connections and test set-up

Figure 4.1 shows the connections amongst various electronic modules of the magnetic susceptibility sonde system. It consists of the sonde iteself, a dc power source, a data acquisition system (DAQ), an input-output (I/O) module, a universal serial bus (USB) to link between the DAQ system and the computer, a general purpose interface bus (GPIB), a pulse rate counter and a six port wire connector.

First of all, insert an I/O module into the DAQ chassis. To do this, remove the plastic cover from the connector in any empty module slot within the chassis, squeeze the two I/O module latches on its sides, insert it into the module slot on the DAQ chassis and press it until both latches lock the module in place. Connect the DAQ chassis to any available USB port on your computer with the help of a USB cable. Connect the power source to the DAQ chassis. The DAQ chassis requires an external +12V dc regulated power supply. This is supplied by an external voltage regulator shown in Figure 4.1. By combining the ease of use and low cost of a data logger with the performance and flexibility of modular instrumentation, National Instruments (NI) compact DAQ provides fast and accurate measurements in a small, simple and affordable system.

A 6-core polytetrafluoroethylene (PTFE) coated leads come out of the sonde. Their colour codes and the associated functionalities are given in Table 4.2. The six leads go into each of the six ports of the wire connector unit. The other end of these ports are connected to various electronic modules. A +18V 32mA max. regulated dc source supplies power to the sonde. The dc supply is connected to the live wire (red) and common return line wire (brown) of the sonde. The blue wire which determines the pulse rate output is connected to the pulse rate counter (also called frequency meter in some text). The remaining three wires (grey, yellow and orange) which constitute the digital output of the sonde are fed to the DAQ unit. With the flexible NI software provided, one can easily log the sonde data out to a file or export the data to a spreadsheet. This system is ideal for applications that require portability and hence it can be used at well site for real time data acquisition.

4.2.1 Data acquisition system (DAQ)

The NI Compact DAQ system is a data acquisition and control system that uses open software and runs built-in data logging programs for acquisition, analysis, control, and display of the data. It provides plug-and-play simplicity to transfer sonde data over the USB bus on to the personal computer. It consists of three parts: C series I/O modules, the cDAQ chassis, and a USB connection to transfer data from the DAQ chassis to the personal computer. The I/O module fits inside the DAQ chassis and acts as a communication means between the sonde and the DAQ chassis. The grey, yellow and orange wires (digital output of the sonde) are fed to the I/O module through the GPIB (general purpose interface bus) cable shown in Figure 4.1.

4.2.2 C series input-output (I/O) module

I have used NI 9401 C-series I/O module which is an 8-channel bidirectional digital input module for any NI Compact DAQ chassis. It can be programmed for eight digital inputs, eight digital outputs, or four digital inputs and four digital outputs. For our sonde system, I have used it as 4 I/P : 4 O/P module. The I/O module is designed as a self-contained measurement module. All circuitry required to process the sonde data is contained within the module itself. All analog to digital (ADC) and digital to analog (DAC) conversions happen in the module before the data reaches the chassis. The I/O modules are hot-swappable and automatically detected by the DAQ chassis.

4.2.3 Data transfer using LabView

First of all, power on the DAQ chassis. It has two light emitting diodes (LED's) marked with 'active' and 'ready'. The 'active' LED indicates whether the chassis is communicating over the USB bus. Its colour indicates whether the USB connection is full-speed (shown by green light) or hi-speed (shown by orange light). The 'ready' LED is lit when the chassis is ready to receive data from the sonde. The I/O module and the DAQ chassis measure and control the digital data coming out of the sonde. They also provide necessary signal conditioning to sonde data. The data processing at the DAQ chassis requires customizing the DAQ system with I/O module to meet channel count and measurement type requirements. This is done through the LabView software. A brief detail of how the data is output from the sonde is described below.

A custom made data acquisition and control program called 'SondeSystem' was written in LabView software to check the prototype sonde performance. A block diagram of

this program is shown in Figure 4.2. The program is scaled to a change of one least significant bit which is equal to $4\pi \times 10^{-5}$ SI units. For simplicity, I have shown the sonde output in decimal numbers within the program in Figure 4.2. However, all the sonde output values will eventually be multiplied by $4\pi \times 10^{-5}$ as shown in Tables 4.4 and 4.5. The software communicates with the DAQ chassis and the I/O module to monitor and acquire all the measurements. The software generates a 10 kHz clock pulse which is supplied to the orange wire of the sonde through the DAQ chassis. The I/O module then clocks the susceptibility data out of the sonde in a 24-bit serial fashion. The DAQ chassis makes the sonde data being transferred in a 24-bit binary mode to the personal computer. The binary data output is decimated by the software and is displayed on the computer screen.

Figure 4.3 shows a computer screen image of the sonde data output. It is divided into two parts. The 10 kHz trigger waveform is shown by the upper half of the image and the data waveform is shown by the lower half. When the sonde comes in contact with a formation containing magnetic minerals, its output increases. This increase in output is shown by an increase in frequency of the output pulses shown in the data waveform window (Figure 4.4). However, the exact change in the sonde output is read by the 'Data' button shown on the right in Figures 4.3 and 4.4.

4.3 Operating considerations of the sonde

The operating considerations of the sonde mentioned below correspond to those of standard wireline tools. However, I have used 44.5 mm diameter boreholes instead of industry standard 101.6 mm diameter (sometime even larger) boreholes. This is because the sonde external diameter is 43 mm and it has to be in close proximity of the formation in order to detect its magnetic susceptibility signal. In Sections 4.7.2 and 4.8, I will see the effect of bigger diameter boreholes on sonde performance. Some of the considerations taken into account during sonde preparation include:

- Maximum downhole time = 24 hours
- Total power dissipated by electronics = 18 Watts
- Borehole operating temperature = 110 ^{o}C
- Maximum case temperature of any chip should not exceed 100 ^{o}C
- Maximum power dissipated by a single chip = 1.5 to 2 Watts
- Entire system must fit within 43mm external diameter enclosure

4.3.1 Sonde calibration

A composite block of sand, cement and magnetite is used for calibration purposes. The details of this block are given in Section 4.8. The magnetite particles can show extremely small drifts within the calibration block over long periods of time. The calibration check is performed before and after a logging sequence. The calibration of the sonde with time is assumed to be superior to the ferromagnetic drift of the sample.

4.3.2 Capacitive effects of borehole fluids

The magnetic susceptibility sonde will be involved in applications where it will be immersed in water or mud downhole. To simulate the capacitive effects of these borehole fluids during calibration, the calibration is grounded via hand contact and the change in reading is noted.

4.3.3 Thermal equilibration

The temperature compensation of sonde electronics (Section 3.5 **Chapter 3**) has a time constant of approximately 10 minutes. Therefore, prior to commence logging, the sonde electronics should be allowed to achieve thermal equilibrium within the borehole for this period of time.

4.3.4 Referencing

The sonde is raised to about 1.5 meter above the ground and the magnetic susceptibility reading is noted. This reading is called the sonde reference. All the readings in the borehole are taken with respect to this sonde reference. However, care should be taken that no metallic objects are present near the sonde when taking the reference measurement.

4.3.5 Pressure and temperature considerations

The electronic circuitry is maintained at approximately normal air pressure. The silicon oil surrounds the sensing coil and compensates for the temperature and pressure induced drifts. However, the sonde should not be exposed to temperatures in excess of 110 °C as this is the maximum temperature rating the sonde electronics have. I have also installed a peak recording thermometer inside the sonde which cut out the electronic circuit automatically if the temperature exceeds 110 °C.

4.3.6 Electromagnetic compatibility

The sonde electronics mentioned in **Chapter 3** contains no high frequency components likely to cause emissions which could affect other apparatus lying nearby. The design, including the use of filter in the mains supply and decoupling of internal power supplies, is intended to produce minimal emissions. Other equipment operating in the area is therefore unlikely to be affected. The unit is also unlikely to be affected by interference from other equipment in the normal operating environment. However the sensor coils, by their nature, are susceptible to electromagnetic interference and operation close to high frequency sources of radiation should be avoided. Interference is indicated by instability in the reading when the sonde is maintained in a fixed position.

4.3.7 Logging rate

The zone of investigation has a vertical FWHM (full width half maximum) of 140 mm, and a horizontal penetration beyond the borehole wall of 35 mm. The sonde system acquires data at a rate of 5 readings per second. Therefore, the maximum logging rate achieved will be 5 x 140 mm per second or 0.7 m per second. Lower logging rates must be used for higher resolution.

4.4 Prototype performance experiments

The main purpose of these experiments is to characterize and evaluate the performance of the prototype magnetic susceptibility sonde. Beyond simply proof of concept, these experiments seek to answer the following key performance-related questions:

- How is the sonde's performance affected by in-situ conditions?
- How sensitive is the sonde?
- How does an increase in borehole diameter affect the sonde performance?
- How does the sonde output change with a change in mineralogy or its percentage within the formation?
- What kind of susceptibility data is output from the sonde when run in a heterogeneous borehole?

To answer these questions, several baseline or control experiments were carried out. To see the effect on sonde performance in-situ downhole, I need to know how various environmental parameters, which may affect the sonde output, change with an increase in depth. Temperature and pressure are the most important parameters which encounter significant variations with depth. However, a change in pressure is known to have a

very little or no effect on the magnetic susceptibility signal whereas a change in temperature affects the magnetic susceptibility significantly. In **Chapter 5**, I have carried out experiments to see the effect of a change in temperature on the magnetic susceptibility signal. There, I have performed laboratory based experiments on various reservoir samples to model the in-situ downhole conditions.

I have already discussed in Section 3.3 **Chapter 3** one of the factors contributing towards sonde sensitivity is the strength of its magnetic field, which eventually depends on the number of turns on the coils, the length and spacing between the coils, and the amount of current flowing through the coils. A low strength magnetic field (corresponding to the lower part on the hysteresis curve) may be overshadowed by the formation eddy currents. Likewise, a strong magnetic field (corresponding to the high field part of the hysteresis curve) will not take into account the ferromagnetic component of the formation (I will explain this in **Chapter 5** in detail). The prototype sonde produces a 10 mT applied field which is strong enough to suppress formation eddy currents and also to take into account the ferromagnetic minerals present within the formation material.

Another main factor contributing towards sonde sensitivity is its distance from the formation wall. The performance of the magnetic susceptibility sonde will deteriorate if it is not in the close proximity of the formation wall (in other words, the diameter of the borehole is increased). This is because the strength of the magnetic field decreases in non-magnetic or weakly magnetic mediums (it decreases exponentially in air). Therefore, if there is an increase in gap between the sonde and the formation wall, the strength of the magnetic field penetrating into the formation material will decrease. This decrease in strength will also depend on the type of drilling fluid present between the sonde and the formation (conductive mud, oil based mud, air based etc.). In the following sections, I will prepare 44.5 mm, 50 mm and 101.6 mm diameter laboratory based model boreholes to see the effect of an increase in diameter on sonde performance.

4.5 Borehole materials used in my experiments

Seven representative materials were used in my experiments for the preparation of model boreholes (Table 4.3). These include Doddington sandstone (DS), Clashach sandstone (CS), Locharbriggs sandstone (LS), china clay (CC), mixtures of china clay +

ilmenite (CI), ball clay + ilmenite (BI) and ball clay + magnetite (BM). The rock susceptibility data was obtained using the Bartington's magnetic probe. Some of the data for samples DS, CS and LS was obtained from the Building Research Establishment (BRE) as part of their research in Partners in Technology Programme funded by the Department of the Environment, Transport and the Regions, and Natural Stone Products Ltd [1].

China clay is diamagnetic and consists of a mixture of diamagnetic clay kaolinite and quartz. It shows negative magnetic susceptibility when measured on the Bartington susceptibility probe. On the other hand, ball clay contains a small amount of hematite; the reason it is light brown in colour. It also contains other minerals, primarily kaolinite (but also montmorillonite). Mica and quartz are also present in substantial amounts. Its fine particle size makes it very low perm. CI and BI samples were obtained by mixing china and ball clays with ilmenite powder which is a paramagnetic mineral. The BM sample is obtained by mixing ball clay with magnetite powder (a ferromagnetic mineral). This gives us a variety of borehole samples containing one or more of the diamagnetic, paramagnetic and ferromagnetic mineral. The main permeability controlling clay mineral 'illite' is not available in powder form - the reason I have used ilmenite which is an antiferromagnetic mineral and whose magnetic susceptibility (1.7×10^{-6} m^3kg^{-1}) is very close to that of illite (0.15×10^{-6} m^3kg^{-1}).

Samples DS, CS and LS were obtained by drilling 50 mm internal diameter holes through their solid rocks. The Doddington Sandstone (quarried near the golf course in the village of Doddington between Wooler and Berwick-upon-Tweed, U.K) is from the Fell Sandstone Group of the Carboniferous Limestone. It is a fine-to-medium grained stone with occasional rust coloured markings (the sample I used doesn't have any rust markings though). It is a relatively clean sandstone and shows diamagnetic behaviour when measured on Bartington's MS2K magnetic susceptibility probe (Table 4.3).

Clashach Sandstone (quarried along the Moray Firth coast, U.K) is a pale yellow buff, non-calcareous, medium grained sandstone (we can see the yellowish pink streaks on the sample in Figure 4.8). When measured on the MS2K probe, it shows a very small and positive magnetic susceptibility (Table 4.3). The positive susceptibility may be due to the presence of paramagnetic or ferromagnetic minerals. We will see the effect on the sonde of paramagnetic and ferromagnetic minerals in **Chapter 5** in detail.

Locharbriggs Sandstone (quarried near the village of Locharbriggs, U.K) has a distinctive medium-grained texture, combining with the subtle bedding planes. It is from the New Red Sandstone of Permian age. It shows a slightly higher positive magnetic susceptibility (Table 4.3) compared to Clashach and Doddington sandstones. The higher susceptibility is due to the presence of hematite (a canted antiferromagnetic mineral) which is the likely the cause of this material being red.

4.6 Preparation of model boreholes in the laboratory

The heterogeneous model boreholes have been prepared in the laboratory using powdered materials and from solid rocks. The 44.5 mm diameter boreholes were prepared using a combination of ball clay, china clay, ilmenite and magnetite powders. The 50 mm diameter boreholes were prepared from solid blocks of Doddington, Clashach and Locharbriggs sandstones. In both cases, the borehole samples are stacked together to see the effect of bed boundaries and also the effect of individual samples on the magnetic susceptibility sonde.

4.6.1 Model boreholes from powder material

To prepare a heterogeneous borehole from powder materials, I have used two techniques. In the first technique, I have used the apparatus shown in Figure 4.5a. It consists of a hard, transparent plastic tube which holds the material tight inside the tube. There is a non-magnetic steel rod placed in the center of the plastic tube. It is a 44.5 mm diameter rod which when removed from the plastic tube, leaves a gap in the middle which allows the prototype sonde to pass through the model borehole. There is also a base holder made from a non-magnetic steel to hold the plastic tube in place. There is also a hole in the middle of this base holder which holds the steel rod in the center of the tube. Figure 4.5b shows the arrangement when various parts of this borehole preparation kit are put together. There is a pressure seal on the top which is used to push the powder material down for compaction.

The clay samples (BI, CI, and BM) are initially passed through a series of sieves to remove the coarse particles. I also crushed the Locharbriggs sandstone (LS) in powder form to see the effect of quartz sandstone on the output of the susceptibility sonde. The four samples are then poured in layers into the assembly shown in Figure 4.5b. The pressure seal is put on the top which slides down inside plastic tube to put pressure on powder samples. The sample is then put in a high pressure chamber shown in Figure

4.6a. A couple of steel rods are used to push the pressure seal down for sample compaction. I allowed the sample to settle for a week after which it was removed from the pressure chamber. The sample is then put inside another pressure chamber (Figure 4.6b) to remove the central steel rod out. This chamber uses a very rigid white polymer rod whose one side is put on the central steel rod. The pressure is exerted on the other end of the polymer rod with the help of a nozzle in the pressure chamber. The pressure is manually increased with the help of a handle which gradually pushes the central rod out of the borehole sample leaving a 44.5 mm diameter hole in the centre.

Model boreholes prepared this way were very brittle. It was very difficult to run the sonde through the borehole without touching its side walls. Any slight contact of the sonde on either side of the borehole wall would scrap the material off the wall thus leaving a bigger diameter hole at that particular depth. If the material used in the model boreholes possess a very small positive or otherwise negative magnetic susceptibility (e.g. CI sample), it would make it very difficult for the susceptibility sonde to detect its magnetic susceptibility if part of the borehole wall is scratched off. It will also be seen in Section 4.7.2 that the sensitivity of the sonde drops with an increase in borehole diameter or if there is no material within the vicinity of the sonde. Also, since these boreholes are prepared by merely exerting pressure on the powder sample, the borehole walls are not very compacted. However, the main problem using such boreholes is them being brittle.

In the second technique, I have used exactly the same arrangement as in the first technique, except in this case I have used a hollow plastic tube at the center which has a 44.5 mm internal diameter. In this case, I do not remove the center tube out of the borehole sample. The powder material is poured in between the outer and inner plastic tubes. Pressure is exerted with the help of a pressure seal and the pressure assemblies shown in Figure 4.6. In this technique, I prepared samples made of pure china clay, china clay + ilmenite (95%, 5%), ball clay + ilmenite (70%, 30%) and ball clay + magnetite (this sample is actually a mixture of 50% ball clay, 40% sand, 9% cement and 1% magnetite). If the samples are poured in layers, the plastic tubes have to be long to accommodate all the layers. If too long, they cannot withstand the high pressure exerted by the pressure assembly of Figure 4.6. Therefore, the samples are prepared individually and are shown in Figure 4.7.

4.6.2 Model boreholes from solid rock

In the second set of borehole samples, I have prepared 50 mm diameter boreholes by drilling through solid blocks of Doddington, Clashach and Locharbriggs sandstones (Figure 4.8). Such boreholes have an external diameter of 80 mm. A 30 mm thickness of the borehole wall is sufficient for the sonde magnetic field to penetrate through the material and obtain enough magnetic information from the borehole formation.

4.7 Results of experiments in the model boreholes

4.7.1 Sonde performance in a 44.5 mm diameter heterogeneous borehole- Powder samples

Figure 4.9 shows the individual samples of Figure 4.7 when stacked together in a borehole formation (from the top: BI, CI and BM samples). The sonde enters the borehole from the top and runs downwards through the center plastic tube. In real wireline logging applications, the sonde is sent downwards and the logging is carried out whilst it is being pulled up. However, for our experiments purposes, I have done the logging while moving the sonde downwards since it is easy to track the position of the sensor coil within the borehole if the sonde runs from the top. There is a gap of around 50 mm between neighbouring samples (BI and CI, and CI and BM). There is no material present within these gaps. They are deliberately created to model fractures within borehole formation and to see their effect on the susceptibility sonde system. There is also a gap between the sonde and the formation wall equal to the thickness of the inner plastic tube (2.5 mm in this case). This gap is essential because in real downhole conditions, the susceptibility sonde will not be touching the borehole wall and there will be a small gap between the sonde and the formation wall. However, care should be taken in case of deviated wells where the tilt in the tool string will change the distance between the sonde and the formation wall. The sensors built on the tool string provide information on the amount and direction of tilt. If the tilt makes the sonde to bring nearer to the formation wall, it will cause an artificial increase in the sonde output. Likewise, if the sonde moves further away from the formation, it will cause a reduction in its output. In these situations, the sonde output should be adjusted in conjunction with the tilt information (i.e. the positioning of the coil section with respect to the formation).

Table 4.4 shows the output data from the magnetic susceptibility sonde when run in the borehole of Figure 4.9 (table also includes data from the china clay sample which is not shown in Figure 4.9). The base of the sensor coil section is the reference position from

which all the measurements are taken. Figure 4.10 shows the corresponding plot of the data given in Table 4.4. From the figure, the sonde provides an output of 150 SI when held in air (outside the borehole at depth 9000 mm). However, as the sensor coil section of the sonde comes in contact with the china clay sample (depths 9025-9125 mm), the sonde output starts decreasing. This is because china clay mainly contains diamagnetic clay kaolinite and there are no paramagnetic or ferromagnetic minerals present. The output decreases to its maximum when the whole of the sensor coil lies within the CC sample (9125 mm). The sonde output may also have some contribution from eddy currents produced within the CC sample. I will discuss the effect of these currents in more detail in Section 4.7.2.

As the sonde travels out of the CC sample, its output increases slightly (depths 9125-9175 mm) due to the presence of fracture and there is no material present. Since the length of the sensor coil is 100 mm, at 9175 mm depth, half of the sensor coil will still be under the influence of the CC sample. That is why the sonde output doesn't come back to its base reading (150 SI) and still shows a slight negative at depth 9175 mm.

As the sensor coil moves towards the CI sample (depths 9175-9275 mm), the sonde output starts increasing (from more negative to less negative). This is because CI sample contains ilmenite as an impurity which has a small and positive magnetic susceptibility. The sonde output ultimately becomes positive at depth 9275 mm (the point where the whole of the sensor coil lies within the CI sample). Therefore, one can say that about 5% ilmenite is required to raise the magnetic susceptibility of diamagnetic china clay to positive.

Again due to the fracture at depths 9275-9325 mm, the sonde output starts decreasing. We can see in Figure 4.10 that the sonde output is slightly positive at depth 9300 mm. This is because at this depth, 75% of the sensor coil is still lying within the CI sample and only 25% of it lies in the fracture region. That is why sonde output shows a small and positive output due ilmenite present in the CI sample. However, at depth 9325 mm, 50% of the sensor coil lies in the fracture region. The susceptibility of air overcomes the small positive signal due to ilmenite and the output comes back to the base reading (150 SI).

The sonde output increases quite rapidly as the sensor coil moves towards the BI sample (depths 9325-9425 mm). It is maximum at depth 9425 mm when the sensor coil is completely surrounded by the BI sample. Once again, as the sensor coil moves out from the BI sample into the fracture (depths 9425-9475 mm), the output decreases to some extent but it doesn't reach to the base line reading i.e. 150 SI. This is due to the reason that at depth 9475 mm, the sonde srarts receiving magnetic signal from the BM sample due to the high magnetic susceptibility of magnetite. As the sensor coil moves into the BM sample (depths 9475-9575 mm), the sonde shows much higher output compared to BI sample. This is because 1% magnetite in sample BM has much higher magnetic susceptibility than a 30% ilmenite in the BI sample (see Tables 2.1 and 2.2 **Chapter 2** for magnetic susceptibilities of paramagnetic and ferromagnetic minerals).

4.7.2 Sonde performance in a 50 mm diameter heterogeneous borehole - Solid rock samples

Figure 4.11 shows the individual samples of Figure 4.8 when stacked together in a borehole formation (from the top: DS, LS, and CS samples). In this case, samples have been prepared from solid blocks of rock. One such Locharbriggs block is shown in Figure 4.11 on which all the samples are stacked. There is no central plastic tube present in the borehole of Figure 4.11 (as was required in Figure 4.9). I increased the diameter of this borehole from 44.5 mm in Section 4.7.1 to 50 mm in this section to see its effect on the sensitivity of the sonde. In the next section, I will increase the borehole diameter to 101.6 mm to see the effect of industry standard boreholes on the sonde output. For these larger boreholes, the sonde is centralised using adhesive plastic plugs (not shown in Figures 4.11 and 4.13) inside the borehole samples.

In Figure 4.11, the sonde enters the borehole from the top and runs downwards. In this case, samples are stacked on top of each other and there is no gap in between neighbouring samples (no fractures). Table 4.5 shows the output data of the magnetic susceptibility sonde and Figure 4.12 shows the corresponding plot of the data. From the figure, the sonde provides an output reading of 150 SI when held in air (7000 mm). However, as the sensor coil section of the sonde comes in contact with the DS layer (depths 7025-7125 mm), the sonde output starts decreasing. This is consistent with the fact that Doddington sandstone mainly consists of a diamagnetic quartz and whose probe magnetic susceptibility is -0.3×10^{-5} SI (Table 4.3). The output decreases to the maximum (146 SI) when the whole of the sensor coil lies within the sample (7125 mm).

The Locharbriggs sandstone contains hematite, the reason its probe magnetic susceptibility is slightly positive (1.7×10^{-5} SI, Table 4.3). That is why when the sonde comes in contact with the LS layer in Figure 4.12 (depths 7125-7225 mm), its output slightly increases from 146 SI in Doddington layer to 147 SI in Locharbriggs. However, in this case the overall sonde output is still negative (<150 SI). This is because the coil section in the sonde is 100 mm long. When the transmitter coil induces magnetic field in to the formation, the field travels a vertical distance of around 100 mm from transmitter coil to the receiver coil traversing through the formation. Along with the magnetic susceptibility signal produced due to magnetic minerals within the formation material, eddy currents are also generated due to conductivity of the formation material. If the concentration of magnetic minerals is relatively small, the conductivity effects dominate the magnetic susceptibility signal and the sonde output goes negative (<150 SI). That is why the magnetic probe shows a small positive susceptibility for the LS sample (since its magnetic field sees into a very small volume of material and no significant eddy currents are generated); whereas the magnetic sonde shows a negative susceptibility (conductivity effects overcome magnetic susceptibility). The sonde output decreases to 146 SI for CS layer (depths 7225-7325 mm) and increases back to 147 SI for LS block (depths 7325-7425 mm).

Another point to note from Figures 4.10 and 4.12 is that the sonde output is more negative for the CC sample compared to the DS sample. The CC sample is dominated by diamagnetic kaolinite whereas the Doddington sample mainly contains diamagnetic quartz. One reason is that kaolinite is more diamagnetic than quartz. But the main reason for the CC sample being more negative is due to its 44.5 mm internal diameter and hence being close to that of the sonde. Eddy currents have a pronounced effect on sonde output when the formation is close to the sensor coils.

4.8 Effect of an increase in borehole diameter on sonde performance

To model the effect of an increase in borehole diameter and the effect of decentralisation on the sensitivity of the prototype sonde, I have prepared a four inch (101.6 mm) internal diameter borehole section. It has the dimensions of height – 290 mm, width – 230 mm, depth - 230 mm and weighs around 25 kg. It is a homogenous sample and has a composition by weight of 80 % sand, 18 % cement, and 2 % magnetite. To prove the homogeneity of this model borehole, I used Bartington's portable MS2K probe and tested the magnetic susceptibility signal along the outer walls

of this model borehole. The susceptibility was very consistent along all the four walls. Figure 4.13 shows a photographic image of this borehole section, and the sonde placed in its centre.

First of all, I took the reference magnetic susceptibility reading by holding the sonde in air about 1.5 meter above the ground. The sonde is then slid through the borehole sample such that the sensing coil section is inside the borehole and is surrounded by the formation material. The sonde is placed in the centre of the 101.6 mm diameter borehole and the sonde output is noted. This gives the magnetic susceptibility of the borehole material surrounding the sonde. The sonde is then decentralized in small steps towards one side of the borehole. Since the borehole sample is homogeneous, it doesn't matter to which side of the borehole the sonde is decentralized. Table 4.6 shows an increase in the sonde output as it is moved towards one side of the borehole wall. The table also calculates the net magnetic susceptibility value (after subtracting the air value) which corresponds to the magnetic susceptibility of the formation material.

Figure 4.14 shows a graphical variation in magnetic susceptibility signal as the gap between the sonde and the nearside formation wall changes. The sonde has an outer diameter of 43 mm. When the sonde is at the center of the 101.6 mm diameter borehole, there will be a 29 mm gap between the sonde and on either side of the formation wall. This makes the sonde read a lower value of magnetic susceptibility. However, as the sonde is moved towards either side of the borehole, the gap between the sonde and the nearside formation wall decreases. This makes the magnetic susceptibility output increase until it reaches to its maximum value when the sonde is touching the formation wall.

4.9 Conclusions

- Model boreholes prepared in the laboratory can be used to test the prototype sonde and to process the data output from the sonde. Such boreholes can be made using powder materials or by drilling through solid pieces of rock.

- The sonde is more sensitive for smaller diameter boreholes. In such cases, the formation wall is much closer to the sensor coil and the magnetic susceptibility produced by magnetic minerals present within the formation material can be easily detected by the sonde. The sensitivity of the sonde decreases with an increase in

borehole diameter. In other words, sensitivity decreases as the distance between the borehole wall and the sonde increases.

- If there is a relatively lower concentration of magnetic minerals present within the formation material, eddy currents produced within the formation overcome susceptibility and the sonde shows a negative output. The conductivity of normally encountered borehole fluids will not, however, be sufficiently high to produce this effect.

- One of the main advantages of NI Compact DAQ used in system modelling of the prototype sonde is that it combines signal connectors, signal conditioning, and analog-to-digital converters in a single package. This feature eliminates the need of cabling together multiple components and reduces the number of components that can contribute to noise or failure. Another advantage of the DAQ system is that the digitally isolated DAQ module also breaks error-causing ground loops. Ground loops occur when the system or device under test shares the same ground as the data acquisition system and there is a potential difference between the two devices.

Electrical	Power requirements	+12 to +18 Vdc at 32mA
	Interface	Three-wire 24-bit serial interface.
	I/O connection	6-wire.
Mechanical	Construction	The susceptibility sonde contains an aluminium cylinder containing the electronics and the PVC enclosure containing the sensor coil. This cylinder is sufficiently robust for down-hole operation but can be damaged if it is subjected to excessive shock through dropping or strain through bending.
	Connector type	The sonde uses interface adaptor which includes electrical feed-through for electrical connection between the coil and the electronics.
	Pressure compensation	Silicon oil which expands with an increase in temperature for pressure compensation.
	Weight/length	1kg approx./870mm.
Output data format	Pulse rate output	80 μs pulse width is output.
	Digital data output	Data is output in a 24-bits format with the MSB first.
Calibration	Calibration block	A cement, sand and stable single domain magnetite composite block is used for sonde calibration.
	Groundwater effects	The borehole fluids (formation/drilling fluids) do not affect the sonde output.
Environmental	Max. operating pressure	10,000 psi
	Max. operating temperature	110 ^{0}C
	Max. stratigraphic resolution	35 mm F.W.H.M. (full width half maximum).

Performance	Sensing coil type	A field generating and a compensated pick-up coil.
	Operating frequency	1.4 kHz.
	Principle of operation	ac induction.
	Measuring range	$(4\pi \times 10^{-5})$ to $(4\pi \times 10^{-1})$ SI
	Temperature induced baseline drift	$<80\pi \times 10^{-5}$ SI from 20 ^{0}C to 90 ^{0}C. <1% full scale.
	Jitter	This can be reduced by shielding the whole system from temperature and pressure induced stresses. See section 3.6 **Chapter 3** for details.

Table 4.1: Specifications for the magnetic susceptibility sonde system

Wire no.	Colour code	Functionality	Description
1	Blue	Pulse rate out	0 to 8,000 × ($4\pi \times 10^{-5}$) SI full scale
2	Grey	Ready	Low to high pulse denotes data ready.
3	Yellow	Serial data out	Data are clocked out in a 24-bit binary format.
4	Orange	Clock in	Data is clocked out after the ready pulse is provided.
5	Red	Input	Operates from a regulated +18V supply.
6	Brown	Ground	Ground terminal.

Table 4.2: A six wire electrical interface for the magnetic susceptibility sonde system.

Sample type	Short name	Mineral composition	Sediment type	Porosity (%)	Volume magnetic susceptibility (10^{-5} SI)
Doddington sandstone	DS	Mainly quartz	Sandstone	14.8	-0.3
Clashach sandstone	CS	Mainly quartz	Sandstone	21.4	0.1
Locharbriggs sandstone	LS	Quartz, hematite	Sandstone	18.2-24.9	1.7
China clay	CC	Kaolinite, quartz.	Whiter clay	NM	-0.7
China clay + ilmenite	CI	Kaolinite, quartz, ilmenite.	Whiter clay	NM	2.3
Ball clay + ilmenite	BI	Kaolinite, hematite, ilmenite, quartz,	Darker clay	NM	30.2
Ball clay + magnetite	BM	Ball clay, magnetite, cement, sand.	Brown clay	NM	221.5

Table 4.3: Properties of reservoir samples used in my study and their corresponding magnetic susceptibilities measured on Bartington's probe. NM – not measured.

Arbitrary depth (mm)	**Volume magnetic susceptibility in air (A) ($4\pi \times 10^{-5}$ SI)**	**Volume magnetic susceptibility inside borehole (B) ($4\pi \times 10^{-5}$ SI)**	**Net volume magnetic susceptibility (B - A) ($4\pi \times 10^{-5}$ SI)**	**Type of formation**	**Overlap b/w sensor coil and individual layers (mm)**
9000	150	150	0	Air	0
9025	150	150	0		0
9050	150	148	-2	China clay (CC)	25
9075	150	146	-4		50
9100	150	143	-7		75
9125	150	141	-9		100
9150	150	144	-6	Natural crack	25
9175	150	148	-2		50
9200	150	149	-1	China clay + Ilmenite (CI)	25
9225	150	150	0		50
9250	150	151	1		75
9275	150	152	2		100
9300	150	151	1	Natural crack	25
9325	150	150	0		50
9350	150	156	6	Ball clay + Ilmenite (BI)	25
9375	150	164	14		50
9400	150	170	20		75
9425	50	172	22		100
9450	150	167	17	Natural crack	25
9475	150	160	10		50
9500	150	164	14	Ball clay + sand + cement + magnetite (BM)	25
9525	150	180	30		50
9550	150	196	46		75
9575	150	199	49		100
9600	150	192	42	Air	75
9625	150	171	21		50
9650	150	154	4		25
9675	150	150	0		0

Table 4.4: Change in sonde output when run in a 44.5 mm diameter heterogeneous borehole consisting of CC, CI, BI, and BM layers.

Arbitrary depth (mm)	**Volume magnetic susceptibility in air (A) ($4\pi \times 10^{-5}$ SI)**	**Volume magnetic susceptibility inside borehole (B) ($4\pi \times 10^{-5}$ SI)**	**Net volume magnetic susceptibility (B - A) ($4\pi \times 10^{-5}$ SI)**	**Type of borehole sample**	**Overlap b/w sensor coil and individual layers (mm)**
7000	150	150	0	Air	0
7025	150	150	0		0
7050	150	149	-1	Doddington sandstone	25
7075	150	148	-2		50
7100	150	147	-3		75
7125	150	146	-4		100
7150	150	146	-4	Locharbriggs sandstone	25
7175	150	147	-3		50
7200	150	147	-3		75
7225	150	147	-3		100
7250	150	147	-3	Clashach sandstone	25
7275	150	146	-4		50
7300	150	146	-4		75
7325	150	146	-4		100
7350	150	146	-4	Locharbriggs block	25
7375	150	147	-3		50
7400	150	147	-3		75
7425	150	147	-3		100
7450	150	148	-2	Air	75
7475	150	149	-1		50
7500	150	150	0		25
7525	150	150	0		0

Table 4.5: Change in sonde output when run in a 50 mm diameter heterogeneous borehole consisting layers of Doddington, Locharbriggs and Clashach sandstones.

Volume magnetic susceptibility in air (A) ($4\pi \times 10^{-5}$ SI)	**Sonde decentralization inside borehole (mm)**	**Volume magnetic susceptibility inside borehole (B) ($4\pi \times 10^{-5}$ SI)**	**Net volume magnetic susceptibility (B - A) ($4\pi \times 10^{-5}$ SI)**
150	0	155	5
150	5	157	7
150	9	160	10
150	13	164	14
150	17	170	20
150	21	173	23
150	25	189	39
150	29	213	63

Table 4.6: Effect of decentralization of the magnetic susceptibility sonde on its output signal inside the borehole.

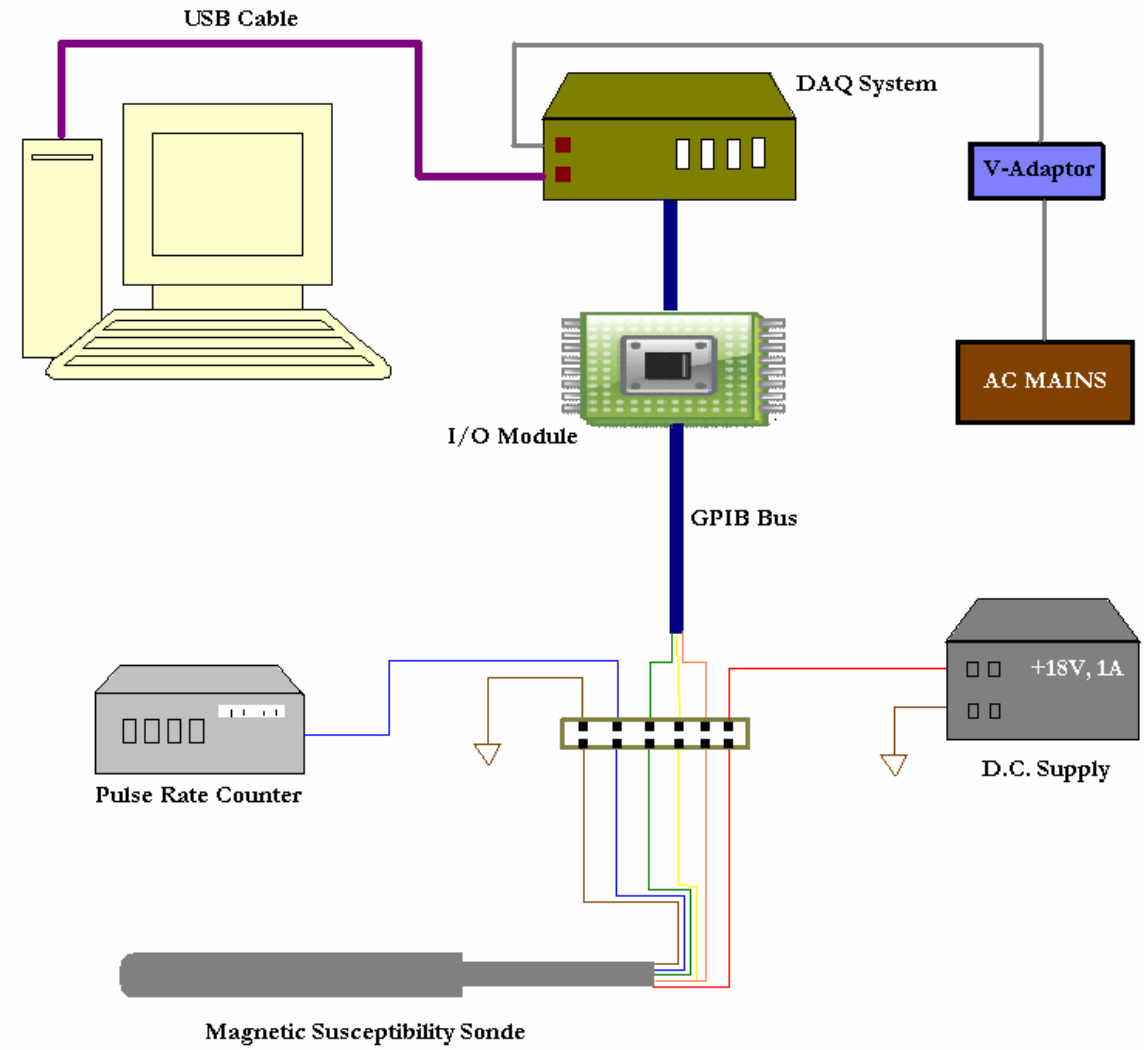

Figure 4.1: Schematic of the connections among various electronic modules of the sonde system.

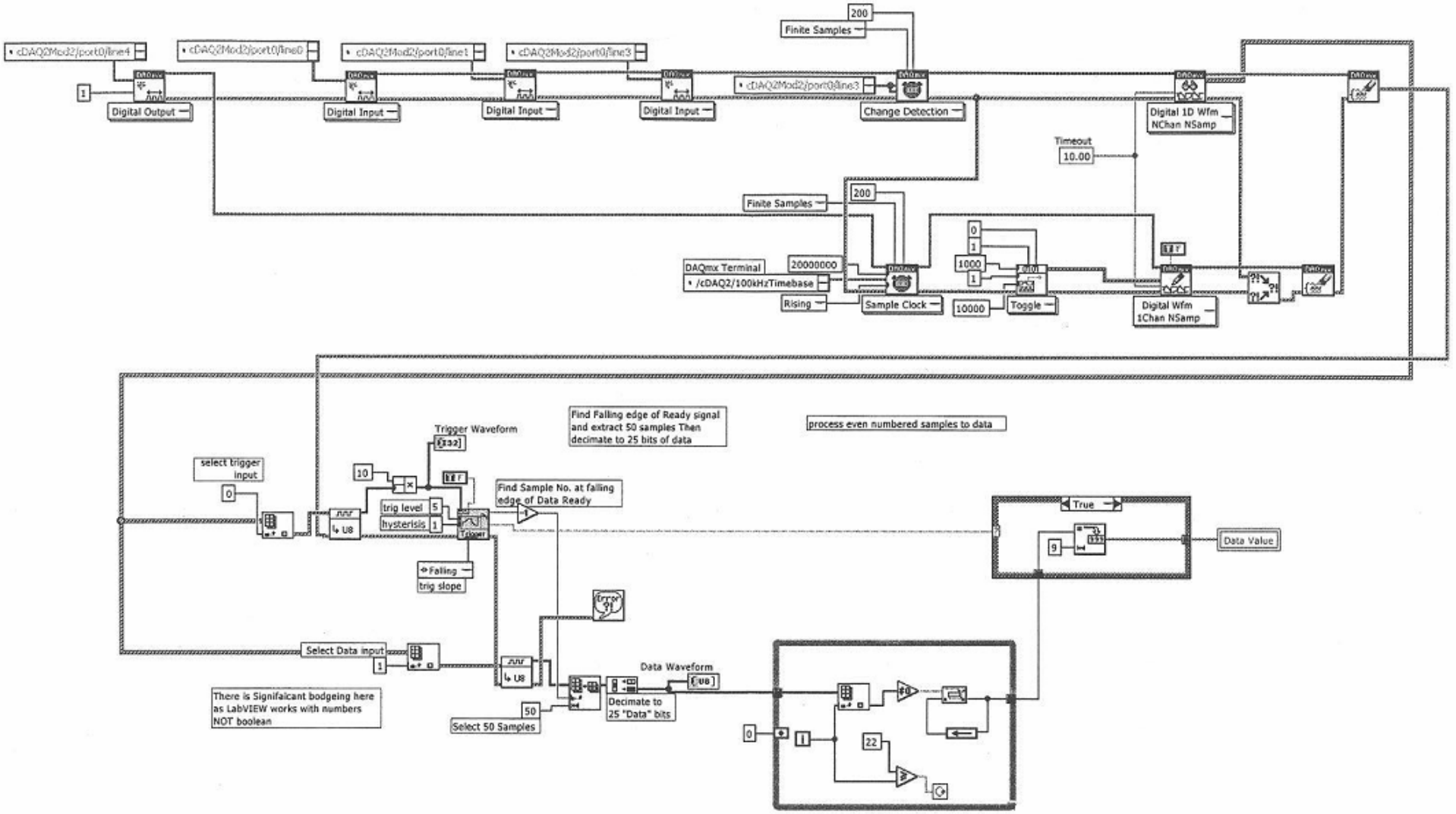

Figure 4.2: A print out of the LabView program written for the sonde system.

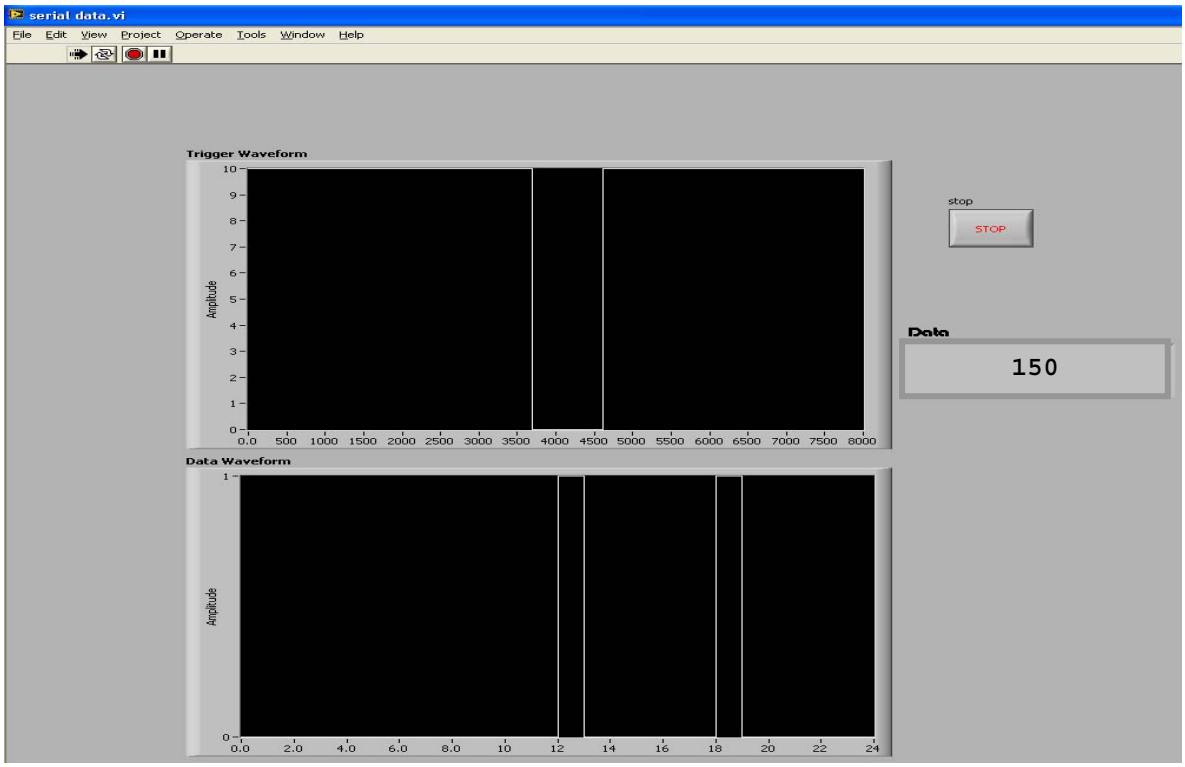

Figure 4.3: A computer screen image of the sonde data output.

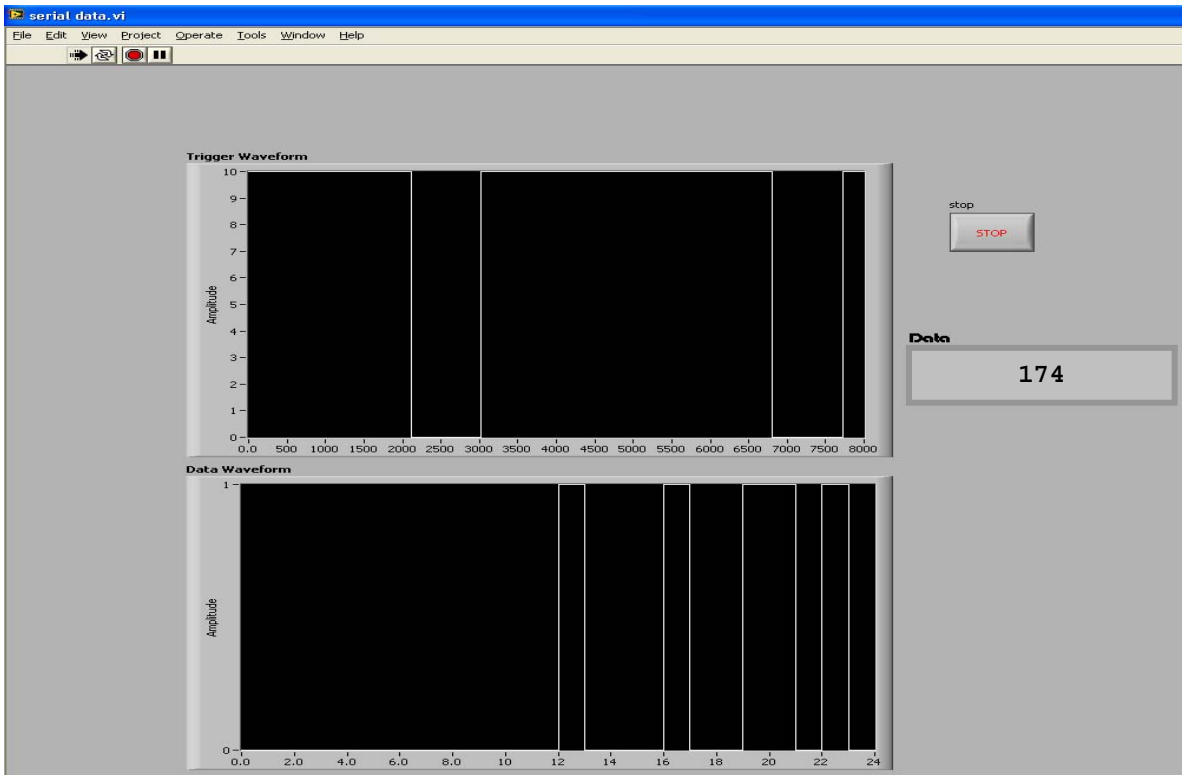

Figure 4.4: An increase in frequency of the output waveform when the sonde comes in contact with a strongly magnetic formation.

(a)

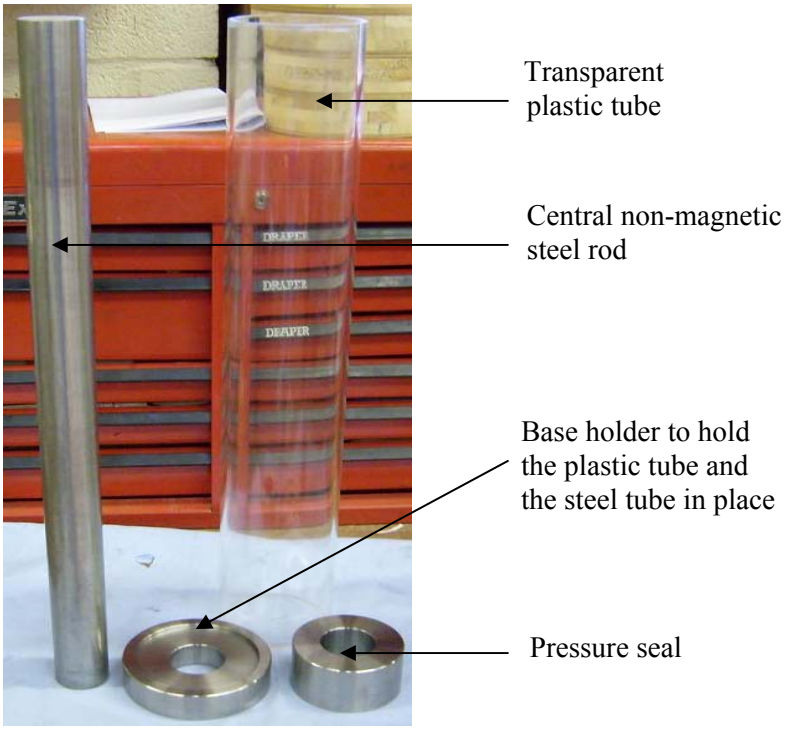

(b)

Figure 4.5: Apparatus to prepare model boreholes from powder materials. (a) Various parts of the borehole preparation kit shown individually. (b) When parts are put together.

(a)

Pressure handle to increase pressure on the borehole sample.

Steel rods to push the pressure seal against the powder material.

Borehole sample with layers of ball clay + ilmenite, china clay + ilmenite, Locharbriggs, and ball clay + magnetite.

(b)

White polymer to push the central non-magnetic steel rod out of the borehole sample.

Handle to push the polymer tube down inside the center of the borehole.

Gap to push the central steel rod out of the borehole sample.

Figure 4.6: (a) High pressure assembly for inserting pressure on the powdered samples. (b) Another pressure assembly to remove the central rod out from the borehole sample.

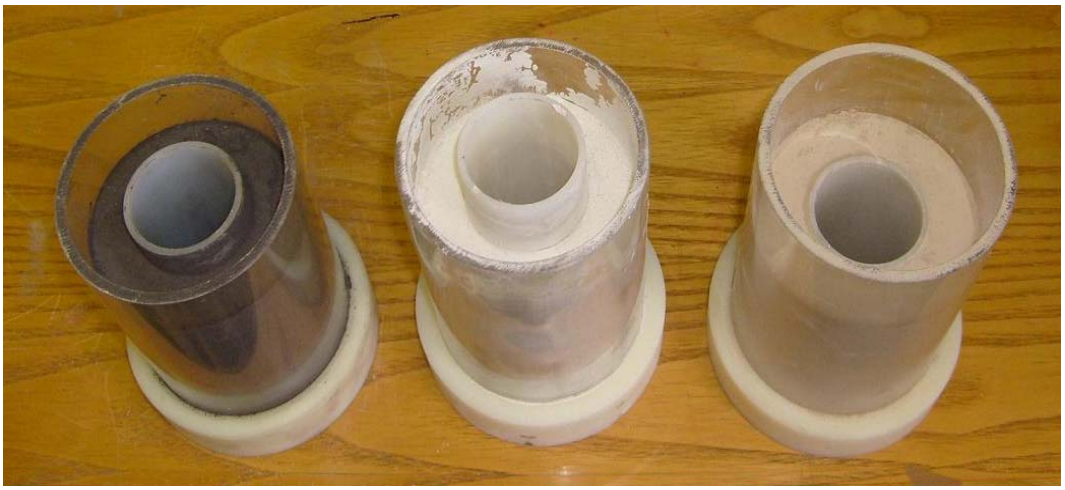

Figure 4.7: 44.5 mm internal diameter borehole samples made from powder materials. **Left:** ball clay + ilmenite sample. **Center:** china clay + ilmenite sample. **Right:** ball clay + magnetite sample.

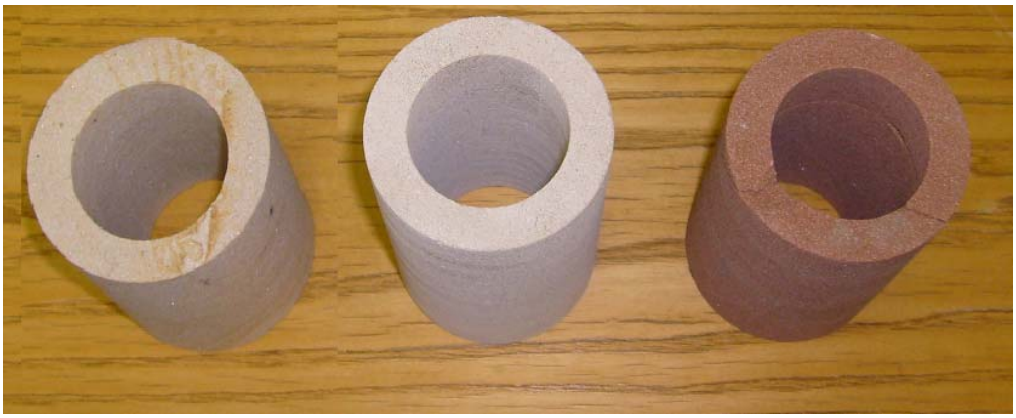

Figure 4.8: 50 mm internal diameter borehole samples made from solid blocks of materials. **Left:** Clashach sandstone. **Center:** Doddington sandstone. **Right:** Locharbriggs sandstone.

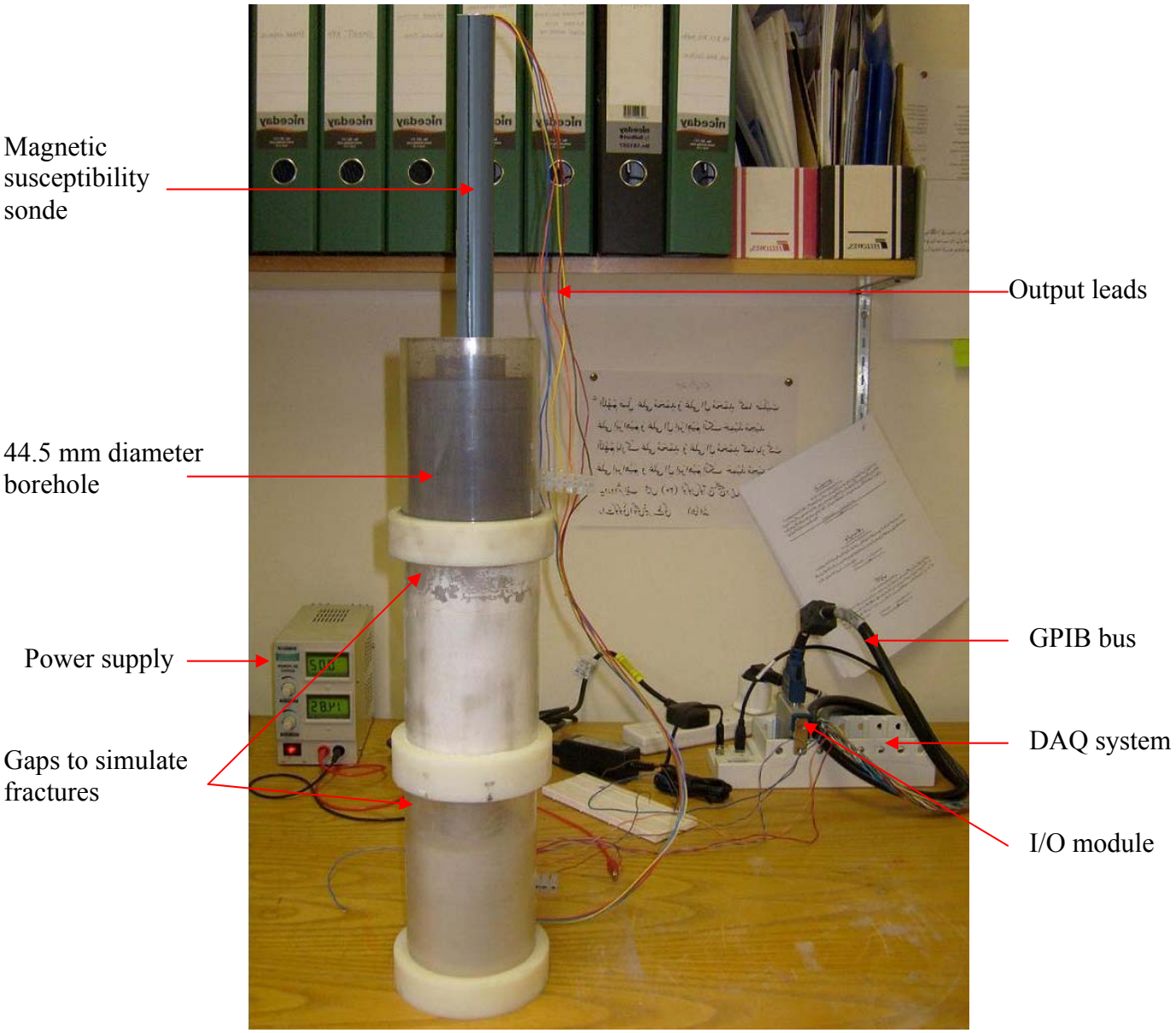

Figure 4.9: Prototype magnetic susceptibility sonde running inside the 44.5 mm diameter samples (from the top: BI, CI and BM samples) when stacked together in the borehole formation.

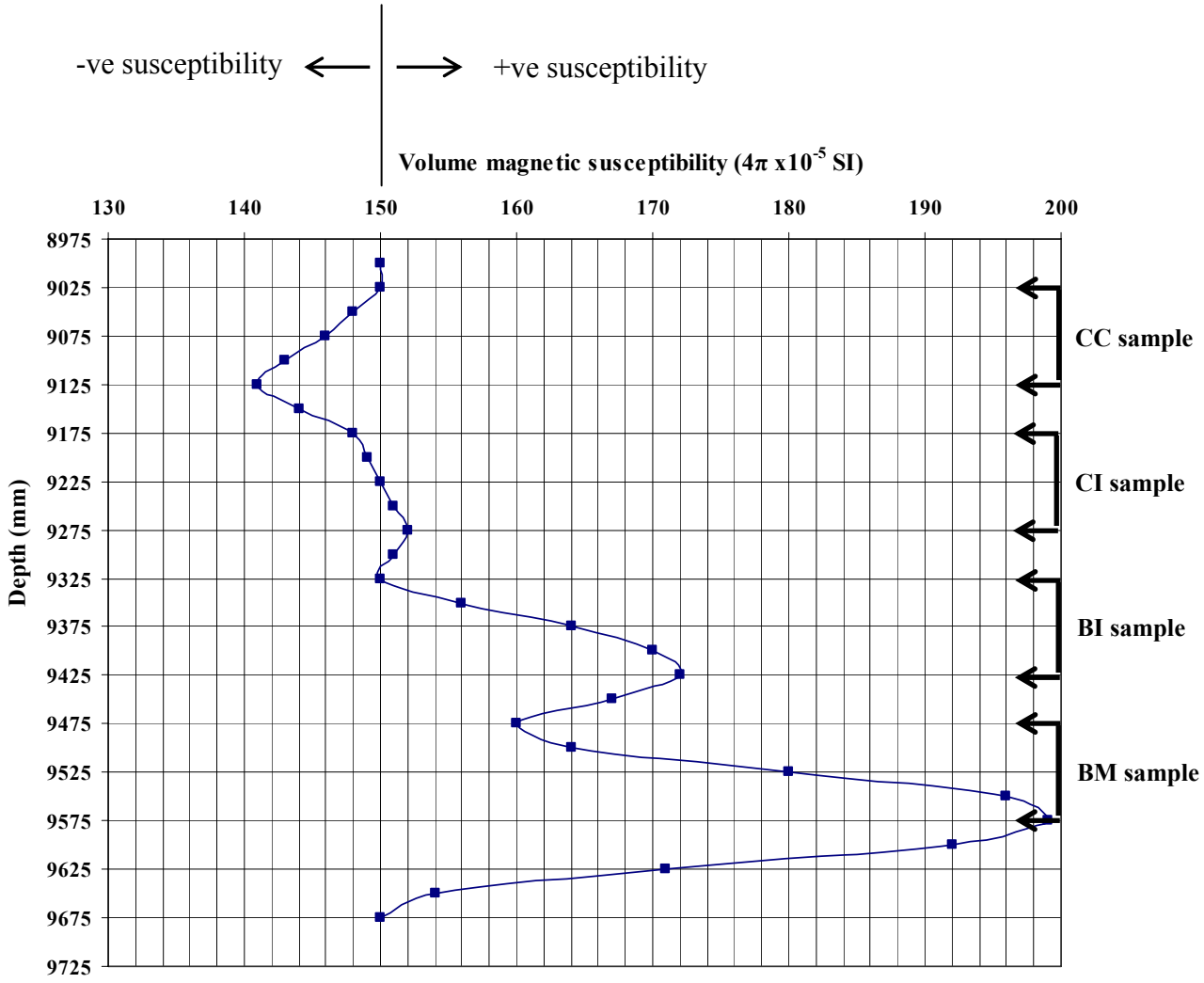

Figure 4.10: Output from the magnetic susceptibility sonde when run in a 44.5 mm diameter heterogeneous reservoir. The depth on the vertical scale represents four different layers; china clay (9025-9125 mm), china clay + ilmenite (9175-9275 mm), ball clay + ilmenite (9325-9425 mm), ball clay + magnetite (9475-9575 mm).

Figure 4.11: Prototype magnetic susceptibility sonde running inside the 50 mm diameter samples (from the top: Doddington, Locharbriggs, and Clashach sandstones) when stacked together in the borehole formation. At the bottom is a solid Locharbriggs block.

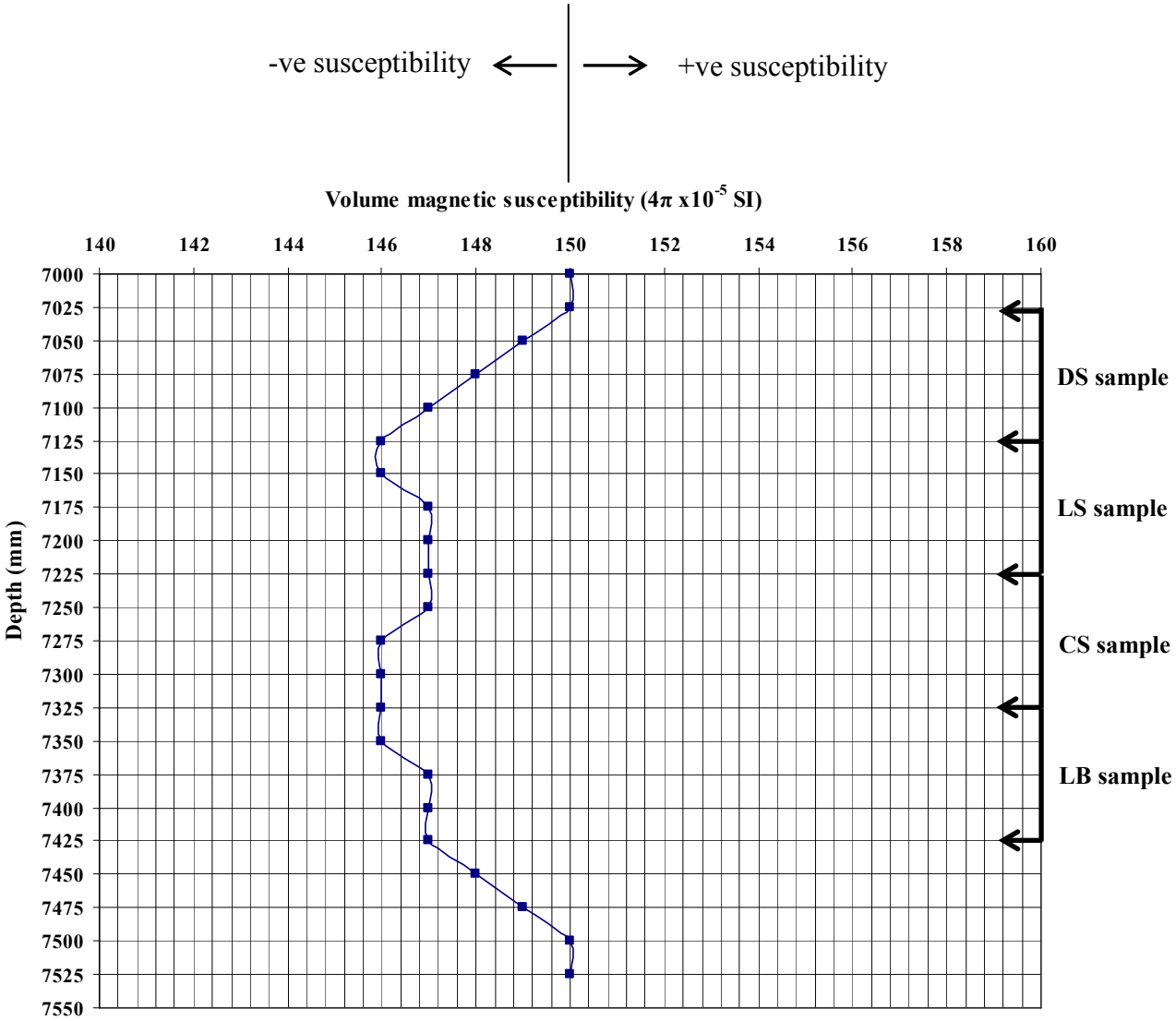

Figure 4.12: Output from the magnetic susceptibility sonde when run in a 50 mm diameter heterogeneous reservoir. The depth on the vertical scale represents three different layers; Doddington sandstone (DS: 7025-7125 mm), Locharbriggs sandstone (LS: 7125-7225 mm), Clashach sandstone (CS: 7225-7325 mm), Locharbriggs block (LB: 7325-7425 mm). LS and LB layers show slightly higher susceptibility due to the presence of hematite.

Figure 4.13: A photographic image of the borehole section and the sonde placed in its center.

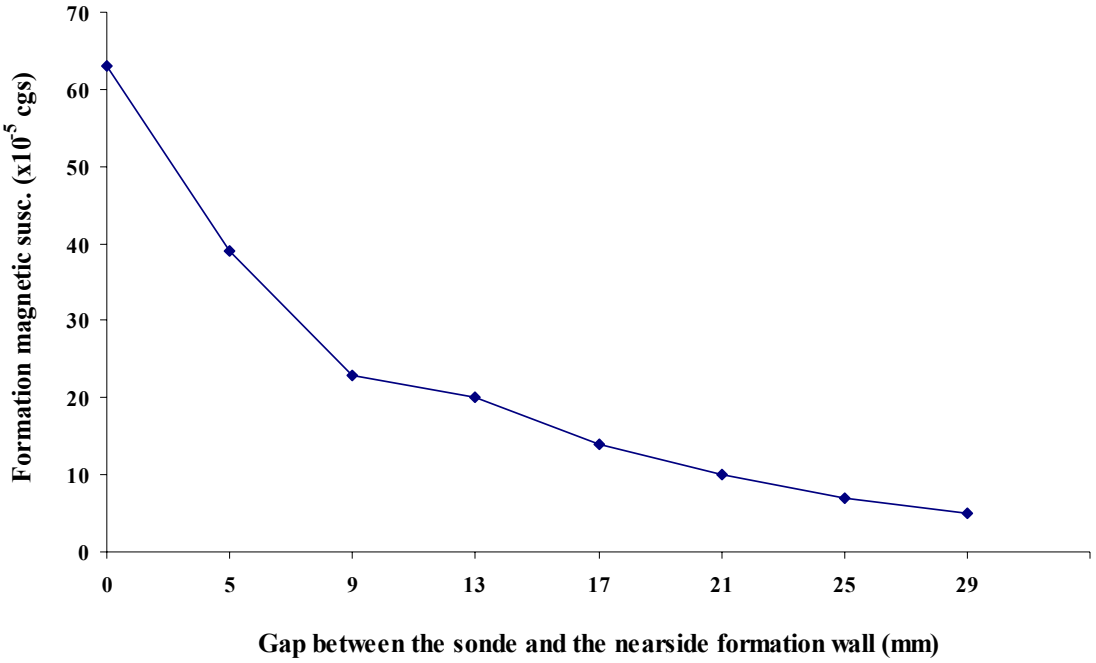

Figure 4.14: Effect of decentralization of the magnetic susceptibility sonde on its output when run in the borehole of Figure 4.13.

Chapter 5

Effect of Temperature on Magnetic Susceptibility of Reservoir Rocks

5.1 Introduction

The main objective of this chapter is to study the variations in magnetic properties of reservoir rock samples at reservoir temperatures. Using the geothermal gradient the experimental variation of magnetic susceptibility with temperature was converted into the variation with depth. Initially, room temperature magnetic hysteresis measurements on all reservoir rock samples were obtained. This allows one to identify multiple mineral components in the rock samples and also their relative amounts. High temperature magnetic hysteresis measurements on the samples were performed to model the behaviour of various reservoir minerals (ferromagnetic, paramagnetic, diamagnetic) at in-situ reservoir conditions. Experiments showed very interesting results indicating that the change in magnetic behaviour of reservoir rock with temperature depend on the type of magnetic minerals present. For example, rock samples having predominantly diamagnetic matrix show a very little or no variation in their high field hysteresis slope with temperature. For samples having predominantly paramagnetic minerals, their high field hysteresis slope decreases with an increase in temperature according to the Curie-Weiss law. Ferromagnetic minerals (I include for simplicity ferrimagnetic and antiferromagnetic components in this category) can show a variety of behaviour at high temperatures. In this chapter, I also study the effect of temperature on the ferromagnetic hysteresis loops which are obtained after subtracting the paramagnetic/diamagnetic contributions of the reservoir rock minerals present in the samples under test. The results show that the ferromagnetic susceptibility doesn't change much with temperature in the lower part of the ferromagnetic hysteresis loop. However, at high applied fields, ferromagnetic susceptibility slightly increases with an increase in temperature.

In the second phase of experiments, temperature dependent susceptibility (TDS) measurements on reservoir rock samples were carried out at low applied fields (1.1mT and 10mT). In this case, I separate out magnetic susceptibilities of individual reservoir rock minerals (ferromagnetic, paramagnetic, and diamagnetic) and analyse their response at increasing temperatures. Magnetic hysteresis parameters like saturation magnetization (Ms), saturation remanent magnetization (Mrs), coercivity (Hc), and

coercivity of remanence (Hcr) were also obtained from the ferromagnetic hysteresis loops. To analyse the effect of temperature on these individual parameters, the ratios Mrs/Ms and Hcr/Hc were plotted on a Day plot to identify the variations in magnetic phase and grain size.

5.2 Previous studies

Magnetic susceptibility is a measure of the degree to which a substance affects a known magnetic field and is a function of the concentration, grain size, and the type of magnetic minerals present (Begét et al., 1990). The temperature dependent susceptibility (TDS) and magnetic hysteresis measurements help detect thermal alterations in the reservoir rock minerals. The acquisition of TDS curves also helps to identify the type of magnetic minerals and magnetic phase transitions in a sample (Hrouda et al., 2003). Changes in hysteresis curves with temperature reflect the variations in multiple mineral components (diamagnetic, paramagnetic and ferromagnetic) in the rock sample. The complex multi-component hysteresis curves exhibit graphically the magnetic contribution of these components, and also numerically through the values of the high and low field magnetic susceptibilities (the slopes at high and low fields). The temperature dependence of their magnetic susceptibilities are used to separate out the effect of each of these minerals from a mixture of magnetic assemblages (Kelso et al., 2002). In such measurements, magnetic susceptibility measurements at low field (χ_{Lfld}) reflect the result of all the thermal changes in a complex mineral system such as a natural rock (Henry et al., 2005). A change in high field susceptibility (χ_{Hfld}) of a sample can be explained by a change in paramagnetic and/or diamagnetic minerals. Recently, a study based on the comparison of hysteresis loops measured at room temperature after successive heating steps revealed that the processes of grain growth, oxidation, stress release, and phase transformations can be evaluated using this technique (Henry et al., 2005).

As a sample is heated, internal thermal energies are aided by external energy, which as a general rule causes the low field susceptibility (χ_{Lfld}) to reduce. Therefore the magnetisation (and hence χ_{Lfld}) of a material is a competition between the ordering of atomic magnetic moments and their disordering by thermal energies. The thermal alteration of magnetic minerals can correspond to the appearance of a new ferromagnetic mineral from paramagnetic phases, the transformation of ferromagnetic phases into other ferromagnetic minerals, or to grain-size and structural changes of

ferromagnetic carriers (Henry et al., 2005). The nature of mineral changes may be highly unpredictable because they are often related to other properties of the sample, such as the amount of water, organic matter, and the presence and intensity of a reducing atmosphere. It would also mean that many Curie temperature (Tc) and Neel temperature (T_N) values are approximate and may vary according to the precise crystalline structure, degree of oxidation and presence of impurities.

5.3 Reservoir samples used in my experiments

Ten representative samples from five reservoirs were studied in this chapter (Table 5.1). The reservoir rock samples were deliberately chosen to reflect a range of typical reservoir types and petrophysical properties (porosity, permeability). The samples represent three types of reservoir: (i) shoreface, (ii) high pressure high temperature (HPHT) shallow marine; (due to being at greater depth than the shoreface samples), and (iii) turbidite reservoirs. Shoreface reservoir I (oil well 2) from the North Sea was represented by a clean sandstone (P21.0) and a muddy sandstone (P28.6). Sample P28.6 is situated around 7 m below sample P21.0. Another shoreface reservoir (reservoir II and oil well 8, belongs to another sector of the North Sea and of a completely different age) was represented by a cemented calcite dogger (P81.3), a relatively clean sandstone (P84.0) and a micaceous sandstone (P812.2). The samples are separated by intervals of around 2 and 10m respectively.

The HPHT shallow marine samples (sandstones M28 and M68) have also been taken from one oil well. They were collected at well depths of 5667.1 and 5693.3 meters respectively.

The turbidite reservoir samples came from a gas reservoir in the Nile delta. They consist of an unconsolidated white sand (1750.24), an unconsolidated darker sand (1760.61) and a shale (S3).

Note that the remaining petroleum fluids, oil residue and organic matter have been cleaned out of samples M28 and M68 by standard cleaning procedures. However, samples P21.0, P28.6, P84.0 and P812.2 contain tiny amounts of residual crude oil.

5.4 Importance of magnetic hysteresis measurements on reservoir rocks

Magnetically weak samples (sedimentary rocks which include clastic and carbonate reservoirs) often show magnetic susceptibilities which are around $0.1x10^{-6}$ m^3kg^{-1} or smaller (John Dearing, 1999). The presence of small amounts of ferromagnetic minerals (e.g magnetite) can significantly affect the magnetic susceptibility of these weakly magnetic rocks. Table 5.2 shows that the magnetic susceptibility value of $0.001x10^{-6}$ m^3kg^{-1} is equivalent to ~0.96 ppm of SP magnetite (0.02 μm), ~1.62 ppm SSD (0.2 μm) or 4.96 ppm titanomagnetite (20 μm). Table 5.3 shows the volume concentration of these crystals in a $10cm^3$ pot. The half of the pot is assumed to be occupied by the solid framework. This shows that samples showing relatively low values of magnetic susceptibilities, there may still be millions of magnetite crystals.

Likewise, if a sample shows negative magnetic susceptibility value, it should not mean that the sample only contains diamagnetic minerals. About 45ppm (0.0045%) titanomagnetite or 9 ppm (0.0009%) ultrafine magnetite is required to raise the χ_{Lfld} of diamagnetic peat ($-0.009x10^{-6}$ m^3kg^{-1}) to zero (John Dearing 1999). Therefore, from the low field magnetic susceptibility values, it is difficult to tell which minerals (diamagnetic, paramagnetic, ferromagnetic) are present in the sample and in how much concentration. High field hysteresis measurements provide us a solution where ferromagnetic components are shown by characteristic kinks at low fields whereas at high fields, largely paramagnetic and diamagnetic components contribute in the susceptibility signal.

5.5 Room temperature magnetic hysteresis measurements on reservoir samples

Initially, magnetic hysteresis measurements on all the reservoir samples were obtained at room temperature using the equipment described in Section 2.5.4 **Chapter 2**. The hysteresis curves were plotted on a graph of applied magnetic field (x-axis) versus magnetisation (y-axis). This is achieved by cycling a sample between a very strong magnetic field applied in one direction and an equal but opposite magnetic field in the other direction. By doing this, a sample responds to these applied field cycles by creating its own magnetisation on the basis of the concentration of magnetic minerals, their grain size, and grain shape. In my experiments the applied field ranged up to 1000 mT (field strength is measured in milliTesla (mT); magnetization measured in Am^2).

On the hysteresis plots, the magnetic susceptibility is given by the slope of the graph. Changes in the slope for a given sample can indicate the relative amounts of multiple mineral components in the sample (Ivakhnenko and Potter, 2008). It potentially allows very sensitive and subtle changes in the magnetic mineralogy to be readily recognized. This can be important, since small changes in illite (a paramagnetic clay) content can significantly affect fluid permeability (Potter, 2005 & 2007). These mineralogical changes, which can potentially be easily recognized from the hysteresis curves, may not necessarily be readily identified by other methods such as X-ray diffraction (XRD).

Figures 5.1a and 5.1b show the room temperature hysteresis curves of all the reservoir samples studied in this chapter. Graphical analysis of these curves from various reservoir rocks reveal clear differences that can be explained by the relative amounts of the different mineral components that they contain. Diamagnetic minerals are recognised by exhibiting straight lines of negative slope. In contrast, paramagnetic minerals will exhibit a straight line with positive slope. A mixture of a diamagnetic matrix mineral (such a quartz) and a paramagnetic clay mineral (such as illite) will have a slope that is dependent upon the content of the two minerals (Ivakhnenko and Potter, 2008). The presence of ferromagnetic components causes "kinks" in the characteristic hysteresis loops in the low field region of the graphs. The special case of a single ferromagnetic component hysteresis loop is shown in **Chapter 2** (Section 2.5, Figure 2.7).

In a complex case of a high applied magnetic field well above the saturation magnetisation (Ms) of any ferromagnetic component in the sample, only the paramagnetic, diamagnetic, and antiferromagnetic matrix minerals will respond to the external field. Therefore the magnetisation in high magnetic fields above Ms can be used to calculate the high-field magnetic susceptibility (χ_{Hfld}).

One method of finding the high field magnetic susceptibility (χ_{Hfld}) is to calculate the high field slope by adding a trendline for a few data points in the high field part of the hysteresis curve using the equation below.

$$y = mx + c$$

For magnetisation 'M' and applied field 'H', we can rewrite the above equation as;

$$M = mH + c \tag{5.1}$$

where 'M' represents the magnetisation, 'H' represents the applied field, and 'm' is the slope of the line in the high field part of the hysteresis curve which also represents the paramagnetic/diamagnetic susceptibility. The intercept 'c' is the shift of the high field slope from the origin (M=0; H=0) due to the presence of ferromagnetic impurities. This means we can calculate the paramagnetic susceptibility by subtracting the value of the intercept 'c' from the magnetisation 'M' at high applied fields. And of course another more conventional way is to calculate the angle of the high field slope. The tangent of the angle will be the paramagnetic susceptibility (provided both X and Y axes are on the same scale). However, one should be careful to multiply the resulting magnetic susceptibility by $4\pi\times10^{-4}$ if the applied field is in mT (by $4\pi\times10^{-7}$ if the applied field is in Tesla). That is

$$\chi_{Hfld} = (M/H)\times4\pi\times10^{-4} \tag{5.2}$$

where magnetisation (M) is in Am^2kg^{-1} and applied field (H) is in mT. The χ_{Hfld} represents the sum of magnetic susceptibilities of paramagnetic, diamagnetic and antiferromagnetic components.

$$\chi_{Hfld} = \chi_{dia} + \chi_{para} + \chi_{antiferro} \tag{5.3}$$

Whereas the initial low field magnetic susceptibility (χ_{Lfld}) also takes into account the ferromagnetic component of the sample. That is

$$\chi_{Lfld} = \chi_{ferro} + \chi_{dia} + \chi_{para} + \chi_{antiferro} \tag{5.4}$$

Therefore the difference between equations 5.3 and 5.4 gives us the ferromagnetic susceptibility.

$$\chi_{ferro} = \chi_{Lfld} - \chi_{Hfld}$$

Likewise we can obtain the magnetisation induced by the ferromagnetic component (M_{ferro}) after subtracting the magnetisation induced by the diamagnetic and/or paramagnetic components (M_{Hfld}) from the hysteresis curve.

$$M_{ferro} = M_{Lfld} - M_{Hfld}$$

We can then calculate ferromagnetic hysteresis curves (Figures 5.2 and 5.2) for the reservoir samples by plotting the magnetisation (M_{ferro}) against the applied field (H).

5.5.1 Reservoir I samples (P21.0 and P28.6)

Room temperature hysteresis loops for shoreface reservoir I samples (P21 and P28.6) are shown in Figure 5.2a. In this figure, sample P21.0 exhibits an almost straight line with a steep negative high field slope. This demonstrates that the sample consists primarily of a diamagnetic mineral. This is consistent with the fact that this sample is a clean sand (essentially diamagnetic quartz). The slight "kink" in the curve at low applied field indicates the presence of a very minute amount of a ferromagnetic mineral. Sample P28.6 also exhibits a negative slope at high fields, indicating a predominant diamagnetic component (again quartz in this case), but the slope is less negative than that for sample P21.0. This suggests an increased contribution from paramagnetic component(s) in sample P28.6. This is consistent with this sample being a muddy sandstone (Table 5.1), with a slightly higher content of paramagnetic illite clay. However, the less pronounced hysteresis loop at low applied fields demonstrates a relatively low concentration of ferromagnetic component in sample P28.6 compared to sample P21.0.

Figure 5.2b shows the corresponding ferromagnetic hysteresis loops (after diamagnetic correction) for samples P21 and P28.6. The high field slope is almost zero and the hysteresis curves purely indicate the magnetisations due to ferromagnetic contribution. Some of the slope-corrected ferromagnetic loops in Figure 5.2 do not show perfect saturation at higher fields (>0.4 T). This is because I have performed the slope correction manually and there may still be a tiny amount of error (due to paramagnetic/diamagnetic impurities) in the construction of these ferromagnetic hysteresis loops. From Figure 5.2b, the magnitude of magnetisation is higher for sample P21 than for sample P28.6 verifying that sample P28.6 contains a relatively lower ferromagnetic component.

5.5.2 Reservoir II samples (P84.0, P812.2 and P81.3)

Room temperature hysteresis loops for shoreface reservoir II samples (P812.2, P84 and P81.3) are shown in Figure 5.2c. Samples P84.0 and P812.2 show a very similar pattern to those of reservoir I samples (P21 and P28.6). Sample P84.0 consists predominantly of a diamagnetic mineral (quartz again) with a small ferromagnetic component. Sample P812.2 also has a diamagnetic high field signature (likely to be predominantly quartz), but the slope is slightly more positive, indicating the presence of another mineral (in this case mica). This sandstone also has a small ferromagnetic component shown by a small kink in the low field part of the hysteresis curve. In contrast, sample P81.3 is a natural cement dogger whose high field magnetic susceptibility is dominated by a paramagnetic mineral (possibly pyrite). Its low field magnetic susceptibility reveals the presence of a relatively higher amount of ferromagnetic component shown by a bigger kink.

Figure 5.2d shows the corresponding ferromagnetic hysteresis loops for samples P812.2 and P84 (after diamagnetic correction), and for sample P81.3 (after paramagnetic correction). The magnitude of ferromagnetic magnetization (in other words ferromagnetic contribution towards low field magnetic susceptibility) is higher in sample P81.3 than in samples P812.2 and P84. The ferromagnetic hysteresis loops of reservoir I and reservoir II samples (Figures 5.2b and 5.2d) show that sample P28.6 has got the lowest ferromagnetic component amongst all. Its ferromagnetic hysteresis loop is also more unstable (distorted) compared to other samples. We will see in Section 5.6.2 how its ferromagnetic component behaves with an increase in temperature.

5.5.3 HPHT shallow marine samples (M28 and M68)

Figure 5.3a shows the room temperature hysteresis loops for high pressure high temperature shallow marine reservoir samples M28 and M68. Sample M28 exhibits a straight line with positive high field slope due to the presence of paramagnetic clays. However, unlike shoreface sample P81.3, sample M28 has a very slight kink at low fields indicating the presence of a very small amount of ferromagnetic component. Sample M68 is very similar to shoreface reservoir samples P21, P84 and P28.6. It exhibits a straight line with negative slope (diamagnetic component) at high fields, with a slight “kink” at low fields (small ferromagnetic component). Their corresponding ferromagnetic hysteresis loops shown in Figure 5.3b indicate that sample M28 contains a very similar magnitude of ferromagnetic component like shoreface sample P28.6.

However ferromagnetic component in M28 is relatively stable compared to sample P28.6.

5.5.4 Turbidite samples (1750.24, 1760.61 and S3)

Room temperature hysteresis loops for turbidite samples (1750.24, 1760.61 and S3) are shown in Figures 5.3c. The steeper positive high field slopes of samples 1760.61 (darker sand) and S3 (shale) indicate a higher paramagnetic clay content than the relatively cleaner sand sample 1750.24. Their low field hysteresis loops indicate that all of these samples contain ferromagnetic components. However samples 1760.61 and S3 contain a higher ferromagnetic content shown by a bigger kink than sample 1750.24.

Figure 5.3d shows their corresponding ferromagnetic hysteresis loops. We can see that the magnitude of magnetisation due to the ferromagnetic component is highest in sample S3 (rich shale), slightly less in sample 1760.61 (darker sand), and finally the lowest in sample 1750.24 (whiter sand). Also we can see that ferromagnetic hysteresis loops are much smoother and stable for these samples compared to sample P28.6. This is due to the presence of a higher ferromagnetic content in these samples.

5.5.5 Hematite sample (MST1)

Room temperature hysteresis loop for sample MST1 is shown in Figure 5.1b. The negative high field slope indicates that the main matrix mineral is diamagnetic quartz. The ferromagnetic component saturates at much higher fields which suggests the presence of an antiferromagnetic component (hematite in this case). The presence of an antiferromagnetic component is inferred because: 1) the loop is open at fields above 0.4 T, and 2) its ferromagnetic component saturates at much higher applied fields.

5.6 Effect of temperature on magnetic susceptibilities of dia, para and ferromagnetic minerals

The shapes of temperature-susceptibility curves and distinctive transition points can be used for the detection of minerals and domains in a sample. For example, paramagnetic substances show a decline in their magnetic susceptibility (χ_{para}) with increasing temperature according to the Curie-Weiss Law. The higher the amount of paramagnetic minerals in a sample, the greater will be the decay in high field slope at increasing temperatures. Theoretically modelled variations in magnetic susceptibility with temperature for a paramagnetic clay (illite) are shown in Figure 5.4.

The thermal treatment of ferromagnetic minerals may also lead to the destruction and formation of new mineral phases through oxidation, reduction and dehydration. For example, the presence of titanomagnetite undergoes alteration during low temperature oxidation (< 200 ^{o}C) (Thomson and Oldfield 1986). In the first step of low temperature oxidation (LTO), the (titano)magnetite is changed to (titano)maghemite. This is accompanied by decreasing susceptibility and magnetization intensity and increasing Curie temperatures. In the second step, the (titano)maghemite is changed into magnetite and then further into hematite. The oxidation to magnetite is accompanied by increasing Curie temperatures, susceptibility, and magnetization intensity, whereas the oxidation to hematite lowers the susceptibility and magnetic intensity but increases the Curie temperature (Petersen and Friesen, 1982). It is not necessary in each case during low temperature oxidation that (titano)magnetite is first changed into (titano)maghemite and then into magnetite or hematite. There might also be a direct way of oxidizing (titano)magnetite into magnetite and hematite.

Figure 5.5 summarizes the common features in temperature-susceptibility curves. However, it is difficult to interpret these curves especially when the sample contains a mixture of minerals. To some extent the curves are additive, e.g. a mixture of magnetite and paramagnetic minerals will produce an intermediate curve (John Dearing 1999). However, one should keep in mind that the temperature-susceptibility curve represented by MAG in Figure 5.5 is for the coarse grain MD magnetite whose susceptibility does not change much with an increase in temperature (below Tc). In Figures 2.9 and 2.10, I have shown fine grained magnetite whose magnetic susceptibility increases with an increase in temperature. This is due to the reason that smallar crystals normally contain SD or PSD grains. At higher temperatures, these grains tend to shift towards more stable MD state. This effect is also shown in Figure 5.28 of this chapter.

The high temperature susceptibility measurements in my experiments are carried out by using the VFTB equipment (variable field translation balance) discussed in Section 2.5 **Chapter 2**. The instrument contains a heating unit which is composed of a heater coil, a water-cooled unit, and a thermocouple capable of heating the sample up to 800 ^{0}C. The system is designed to control the sample temperature to observe continuous change in magnetic properties of a sample with temperature. Magnetic properties that can be measured by this equipment include measurement of isothermal remanent magnetization (IRM), hysteresis curves, DC magnetiszation, AC susceptibility, and

anisotropy of magnetic susceptibility (AMS). It takes a relatively long time (≈15mins) for a heating run and acquisition of hysteresis curves. However, the wide dynamic range and sensitivity of measurement (from $2\times10^{-6}Am^2$ to $5\times10^{-4}Am^2$) and the strong magnetic field, with a maximum field of 5T, along with the precise control of temperature within $\pm0.2\ ^0C$ appeal to cutting edge magnetic studies. In my experiments, I have not reached the Curie temperature of the minerals since the in-situ reservoir temperatures for most of the minerals found in hydrocarbon reservoirs do not exceed $200\ ^0C$.

In this section, I have performed temperature dependent susceptibility (TDS) measurements on reservoir samples at 1.1 mT and 10 mT applied fields. Such analyses will be useful to simultaneously see the effect of variations in temperature and applied field on the magnetic susceptibilities of individual minerals (χ_{para}, χ_{dia} and χ_{ferro}). Figure 5.6 shows susceptibility versus temperature curves for samples M68 and P28.6 having mainly diamagnetic matrix and a small ferromagnetic component. These curves are drawn using equations given in Section 5.5. The diamagnetic susceptibility (χ_{dia}) of these samples does not show much variation at 1.1 mT (Figure 5.6a) and 10 mT (Figure 5.6b) applied fields. A slight decrease in χ_{dia} curve with temperature is due to the presence of paramagnetic impurities in the sample. The curves χ_{ferro} and χ_{Lfld} follow very closely to each other at 1.1 mT applied field and is shown by a small difference between χ_{ferro} and χ_{Lfld} curves (Figure 5.6a). This indicates that χ_{Lfld} is mainly dominated by ferromagnetic components and there is very little effect of the diamagnetic matrix on the low field susceptibility signal.

From the hysteresis curves mentioned in Section 5.5, it is known that the majority of the minerals (diamagnetic, paramagnetic, ferromagnetic) respond at relatively low applied fields. However, there is only a partial alignment of paramagnetic magnetic moments at low fields. This is because their atomic magnetic moments require relatively higher applied fields in order to change their orientation. In Figure 5.6, I have shown the magnitudes of susceptibilities for samples M68 and P28.6 at 1.1 mT and 10 mT applied fields. At 1.1 mT, χ_{ferro} and χ_{Lfld} curves follow very closely because diamagnetic and paramagnetic contributions are low and χ_{Lfld} is mainly dominated by χ_{ferro}. However, at 10 mT, the larger difference between χ_{ferro} and χ_{Lfld} curves indicates that diamagnetic magnetic moments have an increased contribution towards χ_{Lfld}. The susceptibility scale at 10mT is much lower compared to 1.1mT due to the reason that in the lower part

of the hysteresis curve, magnetisation increases very slowly with a sharp increase in the applied field. This significantly reduces the magnitude of magnetic susceptibility (χ = M/H). A similar effect is seen for samples 1760.61 and 1750.24 where the difference between χ_{ferro} and χ_{Lfld} becomes wider at 10 mT (Figure 5.7). However the difference is relatively narrower compared to samples M68 and P28.6. This is due to the fact that 1760.61 and 1750.24 samples contain relatively large amount of ferromagnetic minerals.

Since the curves are nicely separated and the paramagnetic/diamagnetic susceptibilities become more effective at 10 mT than at 1.1 mT applied field, this allows one to analyse temperature induced changes in individual susceptibilities (χ_{para}, χ_{dia} and χ_{ferro}) more effectively at higher applied fields. At the same time, it becomes more and more difficult to design the downhole susceptibility sonde with higher applied fields due to various reasons (formation conductivity effects start dominating over susceptibility signal). However, the 10 mT is still very low and hence quite practical in making a downhole logging probe. Therefore, in the following sections, I will analyse TDS curves for all the reservoir samples at 10 mT.

5.6.1 Temperature dependent susceptibility (TDS) analysis on para-ferro samples (1760.61, P81.3)

In this section, I carry out magnetic hysteresis measurements at various reservoir temperatures and temperature dependent susceptibility (TDS) measurements on reservoir samples that contain a ferromagnetic component and a paramagnetic matrix. These analyses are useful in identifying temperature induced changes in magnetic mineralogies (para, dia and ferro), their grain size distribution, and the concentration of minerals within the sample.

As mentioned in Section 5.5.4, sample 1760.61 is a darker sand with a relatively higher paramagnetic and ferromagnetic content. The magnetic susceptibility in the sample is mainly dominated by the ferromagnetic component. The sample is initially heated at four different temperatures (25, 89, 125 and 245 ^{0}C) and the corresponding hysteresis curves are obtained at each of these temperatures (Figure 5.8). By the looking at these hysteresis curves, one can see that the ferromagnetic susceptibility (shown by a kink at low fields) does not change much with an increase in temperature. This suggests that no major mineral transformation has occurred in the sample. The slope of the kink may

also change if there is a change in the amount of paramagnetic component present in the sample. This is because the contribution of paramagnetic susceptibility towards low field susceptibility (χ_{Lfld}) will have an effect on the slope of the kink. Since the kink shape doesn't change in Figure 5.8, it suggests that the relative contribution of ferromagnetic susceptibility towards χ_{Lfld} is much higher than the paramagnetic susceptibility.

From Figure 5.8, the paramagnetic susceptibility (shown by the high field slope) decreases as the temperature increases. The amount of decrease in the high field slope with temperature is an indicative of how much paramagnetic component is present in the sample. If the sample contains a relatively large amount of paramagnetic component, it will cause the high field slope to decrease quite significantly at higher temperatures.

To see the effect of temperature variations on the individual minerals, I have plotted the relevant paramagnetic, ferromagnetic and low field (L_{fld}) susceptibilities of sample 1760.61 in Figure 5.9. χ_{ferro} increases significantly between room temperature and around 100 ^{o}C. This could be due to a number of reasons:

- The overall MD behaviour of the sample was enhanced.
- Due to oxhidation of magnetite into maghemite and hematite.
- Due to the presence of titanomagnetite in the sample (see titanomagnetite susceptibility curve in Figure 5.5).

The fact that χ_{ferro} starts decreasing after around 100 ^{o}C makes an even stronger case for the presence of titanomagnetite. From Figure 5.5, the susceptibility of titanomagnetite increases to about 100 ^{o}C when SD/PSD grains start transforming into more stable MD grains. This happens due to the presence of higher magnetocrystalline energies in SD/PSD grains which act as a source of demagnetizing field. The effect of this demagnetizing field is enhanced at higher temperature and therefore minerals tend to shift to their more stable MD state. At around 100 ^{o}C, the susceptibility of titanomagnetite starts decreasing, whereas the presence of magnetite tries to flatten the susceptibility curve. Therefore, Figure 5.9 suggests that both titanomagneitie and magnetite minerals are present in the sample. The susceptibility versus temperature curves of both these minerals are superimposed to give the resultant χ_{ferro} curve. Figure 5.9 also shows that the ferromagnetic mineral concentration is much higher than the

paramagnetic concentration ($\chi_{ferro} >> \chi_{para}$) and that the ferromagnetic minerals dominate the χ_{Lfld} values. The result is that the low field magnetic susceptibility curve follows very closely to the ferromagnetic susceptibility curve and is less dependent on the paramagnetic susceptibility. If there is a higher concentration of paramagnetic component in the sample, it will cause a significant decrease in the slope of the low field susceptibility curve which in some cases may intersect the ferromagnetic susceptibility curve (we will see this effect in the TDS analysis of sample P81.3 below). Figure 5.10 shows the temperature dependent hysteresis curves for sample P81.3 (a cement dogger from shoreface reservoir) obtained at temperatures 25, 89, 125 and 245 ^{o}C respectively. This sample has a higher paramagnetic and a relatively lower ferromagnetic content. This is shown by its hysteresis curve at 25 ^{o}C with a high and positive high field slope, and a small kink at low fields. The presence of a relatively higher paramagnetic component is also evident from a significant decrease in high field slope with temperature. Therefore for sample P81.3, one can assume that the low field magnetic susceptibility of the sample will reduce quite significantly at high temperatures due to a decrease in the paramagnetic susceptibility. This is in contrast to sample 1760.61 (Figure 5.8), where a relatively higher ferromagnetic component does not show paramagnetic and hence low field susceptibilities (χ_{para} and χ_{Lfld}) display dropping significantly at higher temperatures.

To see the effect of temperature variations on the ferromagnetic component of sample P81.3, I have shown in Figure 5.11 the ferromagnetic hysteresis loops for sample P81.3 after paramagnetic slope correction. We can see that the ferromagnetic component doesn't change much with temperature at low applied fields. However at higher fields, the ferromagnetic slope increases with an increase in temperature. This indicates the possible transformation of a small amount of ferromagnetic component into paramagnetic component. This increase in slope is however not very prominent at low applied fields. The reason behind this is that magnetic signatures of magnetite and hematite do not show very different magnetizations at low applied fields. Since I have performed temperature dependent susceptibility (TDS) measurements at 10mT in this chapter, it would mean that ferromagnetic component will not show any abnormal change at higher temperatures. This is also evident from the ferromagnetic susceptibility curve shown in Figure 5.12 which doesn't show any abnormal change in low field or ferromagnetic susceptibilities with temperature.

From Figure 5.12, a high and positive χ_{Lfld} for sample P81.3 reflects the presence of paramagnetic and/or ferromagnetic minerals. The figure shows that the ferromagnetic mineral concentration is slightly higher than the paramagnetic concentration giving rise to slightly lower values for χ_{para} than χ_{ferro}. However, the ferromagnetic to paramagnetic susceptibility ratio (χ_{ferro}/χ_{para}) is much lower for this sample compared to sample 1760.61 (Figure 5.9). As the temperature increases, paramagnetic susceptibility of sample P81.3 significantly decreases due to the presence of a relatively higher paramagnetic component. The result is that the χ_{Lfld} curve starts decreasing at a higher rate than do χ_{ferro}. As the temperature reaches to about 140 ^{o}C, external thermal energies overcome the magnetic moments in paramagnetic minerals. The result is that the net high field slope becomes negative (Figure 5.10) and the diamagnetic susceptibility overshadows χ_{para}. This causes the χ_{para} curve to intersect the temperature axis (Figure 5.12); the reason χ_{Lfld} curve intersects the χ_{ferro} curve resulting in $\chi_{Lfld} < \chi_{ferro}$.

Figure 5.13 shows the χ_{Lfld} and χ_{ferro} curves for all the para-ferro samples studied in this chapter. Samples S3 (shale), 1760.61 (darker sand) and 1750.24 (whiter sand) contain a relatively large ferromagnetic component compared to their paramagnetic component. This makes their χ_{ferro} curves follow very closely to χ_{Lfld} curves. In contrast, sample P81.3 contains a relatively lower ferromagnetic and a higher paramagnetic content. That is why its χ_{Lfld} curve doesn't follow the χ_{ferro} curve. Instead it decreases significantly with a decrease in the paramagnetic susceptibility.

As opposed to all other samples (1760.61, 1750.24, P81.3), χ_{Lfld} and χ_{ferro} curves for sample S3 do not show a bump at around 100 ^{o}C. This suggests that the sample does not contain any titanomagnetite crystals. A slow and steady decrease in χ_{ferro} suggests that S3 is dominated by magnetite crystals. All other samples (1760.61, 1750.24 and P81.3) contain a tiny amount of titanomagnetite, the reason they show a small kink in their χ_{ferro} curve at around 100 ^{o}C.

Figure 5.14 shows the χ_{para} curves for all the para-ferro samples studied in this chapter. From the figure, sample S3 contains the highest paramagnetic content. It then decreases to sample 1760.61, then to 1750.24 and finally to P81.3. However, in terms of relative amounts of the paramagnetic and ferromagnetic content, sample P81.3 has got the highest concentration of paramagnetic component; the reason why its χ_{Lfld} curve intersects the χ_{ferro} curve (Figure 5.13). For the remaining samples (1760.61, 1750.24

and S3), χ_{Lfld} curves close down to χ_{ferro} curves at higher temperatures. However, the concentrations of their paramagnetic component is not enough to make them intersect their χ_{ferro} curves.

Therefore, for all the samples, there will be a relatively bigger gap between the room temperature χ_{ferro} and χ_{Lfld} curves, which will narrow down at higher temperatures (since paramagnetic minerals start to lose their magnetizations at higher temperatures). The size of the gap will depend on the relative concentrations of paramagnetic and ferromagnetic components in the sample. If I keep increasing temperature, a point is reached beyond which the diamagnetic component in the sample overshadows the paramagnetic effect and the χ_{Lfld} curve intersects the χ_{ferro} curve. This happens at around 140 ^{o}C for sample P81.3. On the other hand, if there is a relatively higher concentration of ferromagnetic component in the sample, there will be a narrower gap between the room temperature χ_{ferro} and χ_{Lfld} curves, which will stay almost consistent even at higher temperatures.

5.6.2 Temperature dependent susceptibility (TDS) analysis on dia-ferro samples (P84, P28.6)

In this section, I analyse temperature dependent susceptibility curves for samples P84 and P28.6 from a shoreface reservoir. Sample P84 is a clean sandstone. Its main matrix mineral is diamagnetic quartz with a tiny amount of ferromagnetic component. Sample P28.6 is a muddy sandstone. It contains a tiny amount of paramagnetic impurities which can be seen from a relatively higher high field slope (less negative compared to sample P84) in Figure 5.15. Although their room temperature hysteresis curves (Figure 5.15) show that both samples have almost similar amounts of ferromagnetic component, their χ_{ferro} curves in Figure 5.16 show that sample P84 has slightly higher ferromagnetic component than sample P28.6. It is also evident from this figure that the magnitude of diamagnetic susceptibility for sample P28.6 is less than sample P84 due to the presence of paramagnetic impurities. Another important point to note is that at low applied fields, diamagnetic mineral assemblages are easily masked by the presence of much stronger ferromagnetic minerals. However, the bigger gap between χ_{Lfld} and χ_{ferro} curves (Figure 5.16) for both samples P84 and P28.6 indicates that the concentration of ferromagnetic minerals is small enough and the diamagnetic component dominates in these samples.

Figure 5.17 shows the temperature dependent hysteresis curves for samples P84 and P28.6 obtained at temperatures 25, 89, 125 and 245 ^{o}C respectively. Since the sample P84 has got a higher diamagnetic component (Figure 5.15), its high field slope doesn't change much with temperature (Figure 5.17a). This is consistent with the fact that diamagnetic susceptibilities do not show much variation at increasing temperatures. However in case of sample P28.6, the high field slope decreases with an increase in temperature (Figure 5.17b). This is also consistent with the fact that P28.6 contains paramagnetic impurities (paramagnetic susceptibility decreases at higher temperatures). This analysis is also useful in the sense that by just visual observation of the sample, we can roughly tell whether there will be much effect of temperature on the sample. The darker the sample is, the higher the amount of paramagnetic clay minerals in the sample, and the greater will be the effect of temperature on sample's magnetic susceptibility. On the other hand, if the sample is a relatively clean sand, it will mainly have a diamagnetic matrix which will not be affected much by temperature variations. And of course, the presence of any ferromagnetic minerals in the sample will also have an impact on the overall magnetic susceptibility since these minerals can show a variety of susceptibility variations at increasing temperatures (Figure 5.5).

Figures 5.18 and 5.19 show the ferromagnetic hysteresis loops for samples P84 and P28.6. A slight increase in the high field slope with temperature for sample P84 is likely due to the oxidation of magnetite into hematite. It is also evident from the figures that the ferromagnetic component for sample P28.6 is erratic at higher temperatures compared to the ferromagnetic component for sample P84. If the heating is continued to about 464 ^{o}C, a new ferromagnetic component is formed in sample P28.6. This is shown by a massive kink in the hysteresis loop in Figure 5.20. This effect will be explained in detail in Section 5.8 where I plot the hysteresis parameter ratios Mrs/Ms and Hcr/Hc on a Day plot (Figure 5.28). In short, at high temperatures (above 300 ^{o}C), reducing process caused by the partial burning of a small amount of organic matter causes the transformation of maghemite and hematite in to magnetite. The reducing process can be demonstrated by the low temperature Verwey transition (not covered in this thesis), the temperature at which magnetite undergoes a phase change.

Figure 5.21 shows the temperature dependent susceptibility curves (χ_{Lfld} and χ_{ferro}) for all the dia-ferro samples studied in this chapter. Their corresponding χ_{dia} curves are shown in Figure 5.22. The high field slopes of the hysteresis curves of these samples

(Figure 5.1b) indicate that the paramagnetic impurities increase from sample P84 to P28.6 and then to sample P812.2. Figure 5.22 confirms this by showing an increase in the paramagnetic component in these samples, their corresponding χ_{dia} curves start shifting upwards. This is due to the fact that the increased paramagnetic concentration starts overcoming the diamagnetic susceptibility.

5.6.3 High temperature analysis on dia-antiferro sample (MST1)

Figure 5.23 shows the change in slope with temperature for sample MST1 having an anti-ferromagnetic component (hematite in this particular case) shown by a big and wide kink that saturates at much higher fields, and a diamagnetic matrix shown by the negative high field slope. The high field slope decreases with an increase in temperature. This indicates that the diamagnetic matrix mineral has paramagnetic impurities which lose their magnetization at higher temperatures. The kink at low field doesn't change much indicating that the ferromagnetic component (I include for simplicity ferrimagnetic and antiferromagnetic components in this category) has not gone through any high temperature mineral transformation.

5.7 Temperature and depth dependence on magnetic hysteresis parameters

Using the geothermal gradient the experimental variation of magnetic susceptibility with temperature was converted into the variation with depth for our reservoir rock samples. A gradient of 33 m/^{o}C (Mayer-Gurr, 1976) was used in my study. The equation that was used to convert temperature respectively to depth of sediment is as follows

$$D = 33T-33(Ts+k_t) \quad (5.5)$$

where D is depth in m, T is temperature in ^{o}C, Ts is the average annual sediment surface temperature in ^{o}C, and k_t is a geographic constant. The average annual sediment surface temperature has been taken as 9.2 ^{o}C, and k_t taken as 0.8, which is an appropriate value for the North Sea region. The conversion of temperature to depth using this equation is shown in Figure 5.24.

Typical depths of the North Sea shoreface reservoir samples were around 4000 m corresponding to an in-situ temperature of 131 ^{o}C. The in-situ temperature for the turbidite samples were around 63 ^{o}C, whilst those for the HPHT shallow marine

samples were around 181-188 ^{o}C. Except for sample P28.6, I have not analysed any of our samples beyond 245 ^{o}C, since the reservoir depths for most of these samples indicate that their reservoir temperatures do not exceed beyond 200 ^{o}C.

In order to gain an insight into the magnetic properties of reservoir rocks and minerals at in- situ reservoir conditions, the dependence of magnetic hysteresis parameters on temperature variations has been experimentally determined for the representative reservoir samples. The hysteresis parameters and their ratios provide additional methods for determining magnetic mineralogy, magnetic grain size, and magnetic concentration. Note that I have not considered the effect of pressure changes on the magnetic properties of the reservoir samples, which are likely to be far less significant than the effect of temperature (Kapička et al., 2003).

In this section, I have classified samples into three groups based on their room temperature low field magnetic susceptibility values given in Table 5.4. The values of magnetic susceptibility and hysteresis data in Table 5.4 have been calculated directly from the hysteresis loops (and ferromagnetic hysteresis loops; Figures 5.2 and 5.3) discussed earlier in the chapter. Sample P84 (relatively clean sand) has relatively lower χ_{Lfld}. On the contrary, sample 1760.61 (darker sand) is characterized by a relatively higher value of magnetic susceptibility. For sample P81.3 (calcite dogger), the corresponding value is somewhere between that of sample P84 and 1760.61. Sample P84 is dominated by diamagnetic matrix whereas sample P81.3 contains paramagnetic matrix.

The high temperature hysteresis parameters (Table 5.5) are obtained from the ferromagnetic hysteresis loops analysed individually for each of the samples at various temperatures. For simplicity, the ferromagnetic hysteresis loops for the individual samples are not shown in this chapter (except for sample P81.3 in Figure 5.11). From the table, sample P81.3 has a slightly higher ferromagnetic content than sample P84 shown by the slightly higher χ_{ferro} values.

Four parameters can be derived from the hysteresis data (Section 2.5, **Chapter 2**); saturation magnetization (Ms, in Am^2), saturation remanent magnetization (Mrs, in Am^2), coercivity (Hc, in mT), and the coercivity of remanence (Hcr, in mT). The changes in the hysteresis parameters as a function of thermal demagnetization are

shown in Figure 5.25. These parameters are plotted against depth (modelled from the experimental changes with temperature). The magnetic parameter changes can be mainly caused by (1) variations in grain-sizes; and/or (2) chemical transformations among magnetite, maghemite, and hematite (Liu et al., 2002). In Figure 5.25a, the saturation megnetisation does not change much at greater depths for all three samples (P84, 1760.61 and P81.3). This indicates that no major mineral transformation has occurred in these samples (Cui et al., 1994). In Figure 5.25b, the room temperature saturation remanent magnetization (Mrs) increases from sample P84 (0.06) to sample P81.3 (0.094), and in turn to sample 1760.61 (2.5), indicating that sample 1760.61 has got the highest concentration of ferromagnetic grains. However, for each of the three samples, Mrs decreases at higher depths, or in other words with increasing temperatures. This indicates that the concentration of PSD/SD grains decreases and that of MD grains increases at greater depths (Liu et al., 2002). See Table I for typical hysteresis parameter values of MD, PSD and SD grains.

The coercivity (Hc) and coercivity of remanence (Hcr) values for all three samples decrease at greater depths (Figures 5.25c and 5.25d). The presence of a small amount of SP grains can contribute enough induced magnetization resulting in a lower value of Hc, but with no effect on Hcr, which depends only on remanence (Jackson et al., 1990). Therefore the presence of both SP and MD particles can decrease Hc and a high value of Hcr/Hc can reflect the presence of both SP and MD grains. However, a decrease in both Hc and Hcr in Figures 5.25c and 5.25d suggests that PSD grains are being transformed into MD grains (rather than SP) at higher depths (Moskowitz, 1980).

The variations in hysteresis parameters can be explained better when plotted as Mrs/Ms and Hcr/Hc ratios as shown in Figures 5.26 and 5.27. From Tables 5.4 and I, the room temperature Mrs/Ms ratios for samples P84 (0.171), P81.3 (0.160), and 1760.61 (0.332), indicate the concentration of PSD grains in these samples. However, the Mrs/Ms (Hcr/Hc) ratio decreases (increases) with an increase in temperature (depth) for samples P84 and P81.3, indicating that PSD grains concentration decreases and MD grains concentration increases (Dunlop, 1986). For sample 1760.61, the Mrs/Ms ratio decreases first but then stabilizes itself after around 4000m.

When plotted on a Day plot (Figure 5.28) an explanation for the observed changes in hysteresis parameters of our reservoir samples (1760.61, P84 and P81.3) becomes

apparent. To see the effect of depth on hysteresis parameters for a number of reservoir samples, I have also plotted samples P28.6, M28 and 1750.24 on the Day plot. From Figure 5.28, the sedimentologically distinctive cement dogger (sample P81.3) and the relatively clean sand (P84) do not show any significant change in magnetic properties at higher depths. They simply show a slow drift from PSD towards MD region. A similar, but less pronounced trend is observed for sample 1750.24. Samples M28 and 1760.61 show a slightly different behaviour. Initially they tend to shift from PSD to MD region (Mrs/Ms decreases). However, at higher depths, their Mrs/Ms ratios increase again showing an increase in the concentration of SD/PSD grains. This is caused when a small amount of MD magnetite oxidises to a high susceptibility maghemite (Liu et al., 2002). Although samples M28 and 1760.61 contain very different concentrations of ferromagnetic minerals, their temperature analyses show very similar effects on their hysteresis parameters. One can argue that suppose mineralogical alterations are minimal and much of the change observed in Fig 5.28 is due to the temperature dependence of particle magnetic properties at SP/SD boundary- i.e. demagnetisation of the Mrs (i.e. lower Mrs/Ms). If this is true, the ratio Mrs/Ms should keep decreasing at higher temperatures. However for samples 1760.64 and M28 in Fig. 5.28, we see that Mrs/Ms initially decreases and then increases with an increase in temperature. We have also shown the evidence of mineralogical alteration in Fig. 5.20 which also supports the argument of hysteresis parameter changes as a result of mineralogical alterations.

The shoreface sample P28.6 plot in the SD region at room temperature. As the temperature is increased (which corresponds to higher depths and is shown by different colour markings on the Day plot), the sample shifts towards the pseudo-single-domain (PSD) and multidomain (MD) regions. This shift is due to the growth of a newly formed MD magnetite which was also shown in Figure 5.20 (shown by lower values of coercivity and remanence). Note also that for sample P28.6 the in-situ reservoir temperature (around 131 ^{o}C) is unlikely to cause significant changes in the domain state of the ferromagnetic component compared to room temperature conditions. It is also worth noting that the model experiments in the laboratory also need to replicate the redox conditions downhole (humidity, pressure etc.) for the results to accurately reflect the in-situ reservoir conditions.

Grain type	Hc (mT)	Hcr/Hc	Mrs/Ms
MD	LOW (2.5-4)	HIGH >4	LOW (0.01-0.03)
PSD	MEDIUM	MEDIUM (1.5-4)	MEDIUM (0.03-0.5)
SD	HIGH (10-40)	LOW <2	HIGH (0.5-0.9)

Table I: Typical hysteresis parameter values for MD, PSD and SD grains (Dunlop 1986).

5.8 Percent susceptibility contribution of the matrix and the ferromagnetic components

Whilst analysing the magnetic properties of reservoir samples, it is important to determine the magnetic phase of the matrix, and the percent susceptibility contribution of the matrix and the ferromagnetic components towards low field susceptibility (χ_{Lfld}). In this section, I have used a technique in which by plotting the ratio χ_{ferro}/χ_{Lfld} against the percent susceptibility contribution of either the main matrix mineral ($\%\chi_{dia}$ or $\%\chi_{para}$) or the ferromagnetic mineral ($\%\chi_{ferro}$); whichever is greater, one can easily make interpretations about the magnetic nature of the matrix and other components within the sample (Figure 5.29). For this analysis, I have used room temperature mineral susceptibility values given in Table 5.5. The x-axis in Figure 5.29 expresses the following relationship:

$$\chi_{ferro} / \chi_{Lfld} = \chi_{ferro} / (\chi_{matrix} + \chi_{ferro}) \quad (5.6)$$

where χ_{matrix} represents the susceptibility of either the diamagnetic (χ_{dia}) or paramagnetic (χ_{para}) matrix.

Zone I (dia-ferro samples, $\chi_{dia} > \chi_{ferro}$)

The figure has been divided into four zones. The ratio χ_{ferro}/χ_{Lfld} less than 0 (zone I) indicates that the main matrix mineral is diamagnetic and the percent contribution of the diamagnetic matrix (χ_{dia}) towards χ_{Lfld} is greater than 50%. Therefore for zone I samples (P21, P84, P28.6 and M68), the vertical axis represents the percent susceptibility

contribution of the diamagnetic matrix ($\%\chi_{dia}$). Equation 5.6 also shows that χ_{dia} contribution increases as the ratio $\chi_{ferro}/\ \chi_{Lfld}$ get closer to the origin and it decreases as the ratio moves away from the origin (more negative). Therefore for zone I, samples P21 and P84 show a very similar diamagnetic susceptibility contribution. Sample P28.6 shows higher diamagnetic susceptibility contribution (being closer to the origin) compared to samples P21 and P84. However, the hysteresis curves of these samples (Figure 5.1b) show that samples P21 and P84 have higher negative high field slopes compared to sample P28.6. This would mean that samples P21 and P84 have got a higher diamagnetic component. However, if I analyse the ferromagnetic component in these samples (Figures 5.2b and 5.2d), sample P28.6 has got the lowest amount of ferromagnetic component which makes its diamagnetic susceptibility more prominent at low fields than for samples P21 and P84; the reason why sample P28.6 plots higher in Figure 5.29. Likewise, sample M68 has got the highest diamagnetic susceptibility contribution even though its high field slope is very similar to those of samples P21 and P84 (Figure 5.1b). This is again due to its relatively smaller ferromagnetic component compared to samples P21 and P84.

Zone II (para-ferro samples, $\chi_{para} > \chi_{ferro}$)

For χ_{ferro}/χ_{Lfld} ratios between 0-0.5 (zone II), the main matrix mineral is paramagnetic and the χ_{para} contribution towards χ_{Lfld} is greater than 50%. It is maximum at the origin and decreases as the ratio moves from 0 towards 0.5. There is no sample lying in zone II which would mean that none of our samples has paramagnetic component that contributes more than 50% towards low field susceptibility.

Zone III (ferro-para samples, $\chi_{ferro} > \chi_{para}$)

For χ_{ferro}/χ_{Lfld} ratios between 0.5-1 (zone III), samples contain a paramagnetic matrix and the ferromagnetic minerals. The ferromagnetic contribution in this case is greater than paramagnetic contribution (contributes more than 50% towards χ_{Lfld}). There will be no paramagnetic effect when χ_{ferro}/χ_{Lfld} ratio becomes unity (Equation 5.6). Therefore, for samples lying in zone III (M28, 1750.24, P81.3, 1760.61, S3), M28 has got the lowest ferromagnetic component whereas sample S3 has got the highest.

Zone IV (ferro-dia samples, $\chi_{ferro} > \chi_{dia}$)

For χ_{ferro}/χ_{Lfld} ratios greater than 1 (zone IV), the main matrix mineral will again be diamagnetic. The only difference in this case is that the χ_{ferro} will contribute greater than

50% towards χ_{Lfld}. Therefore the vertical axis for zone IV samples (P812.2) will represent the percent susceptibility contribution due to the ferromagnetic component ($\%\chi_{ferro}$). It will be higher for χ_{ferro}/χ_{Lfld} ratio close to 1 and decreases as the ratio becomes higher and moves away from unity.

5.9 Conclusions

- Increase in temperature causes the magnetic ordering of paramagnetic material to become more chaotic, leading to a slight decrease in χ_{Lfld} due to χ_{para} being reduced. This can be seen in Figure 5.13 where χ_{ferro} and χ_{Lfld} has a bigger gap at low temperatures and the gap narrows towards higher temperatures.

- Pure diamagnetic minerals exhibit a magnetic susceptibility that is independent of temperature (and therefore independent of depth in the reservoir). The fact that experimentally some predominantly "diamagnetic" reservoir samples (P84, P28.6) showed slight decreases in χ_{dia} with increasing temperature (Figure 5.16) suggested that there are small amounts of paramagnetic minerals in the samples.

- Magnetic hysteresis measurements conducted at various temperatures can be used to identify relative concentrations and changes in magnetic behaviour (para, dia and ferro). A greater decrease in high field slope with temperature would mean the presence of a higher amount of paramagnetic component in the sample. This is consistent with observations of decreases in χ_{para} for reservoir samples S3 and 1760.61 (Figure 5.14) having an intrinsically higher paramagnetic content compared to the ferromagnetic content.

- Subtracting the paramagnetic and diamagnetic component from the hysteresis loops, the resultant ferromagnetic hysteresis loops are indicative of the ferromagnetic concentration in the sample. The temperature analyses of ferromagnetic hysteresis loops provide information on the stability of the ferromagnetic component. From this, one can infer whether the sample is likely to undergo chemical changes at in-situ reservoir conditions. Information like saturation magnetisation, domain state and percent contribution of ferromagnetic minerals towards total susceptibility (χ_{Lfld}) is obtained from the ferromagnetic hysteresis loops.

- Some idea of the domain state, single-domain (SD) or multidomain (MD), of the ferromagnetic carriers in the reservoir samples can be obtained by plotting relevant hysteresis parameters (Hcr/Hc versus Mrs/Ms) on a Day plot. Changes in the domain state with increasing temperatures were observed which either resulted from the formation of new ferromagnetic components and/or variations in grain size. For example, the shoreface sample P28.6 (Figure 5.28) plot in the SD region at room temperature. As the temperature was increased significantly, the sample shifts towards the pseudo-single-domain (PSD) and multidomain (MD) regions. This shift is due to the growth of newly formed MD magnetite which was also shown in Figure 5.20. Note, however, that for sample P28.6 the in-situ reservoir temperature (around 131 ^{o}C) is unlikely to cause significant changes in the domain state of the ferromagnetic component compared to room temperature conditions.

- Dividing the susceptibility of the ferromagnetic component (χ_{ferro}) by the low field susceptibility (χ_{Lfld}) for any reservoir sample and plotting it against the percent susceptibility contribution of the dominant susceptibility carrying mineral, one can easily make interpretations about the magnetic nature of the matrix and other components within the sample. One can also determine the percent contribution each component brings to the total or low field magnetic susceptibility.

Sample	Well	Type of reservoir sedimentary environment	Type of hydrocarbon in reservoir	Sediment	Well depth (m)	Permeability (mD)	Porosity (%)
P21.0	2	Shoreface	Oil	Sandstone	3660.3	996	18.6
P28.6	2	Shoreface	Oil	Muddy sandstone	3667.5	9	17.3
P81.3	8	Shoreface	Oil	Dogger	3716.2	0.02	5.9
P84.0	8	Shoreface	Oil	Sandstone	3718.4	75	21.1
P812.2	8	Shoreface	Oil	Micaceous sandstone	3725.9	4.0	19.0
M28	NK	HPHT shallow marine	Oil	Sandstone	5667.1	3.6	28.4
M68	NK	HPHT shallow marine	Oil	Sandstone	5693.3	4.0	21.1
1750.24	20	Turbidite	Gas	Whiter sand	1750.24	NM	NM
1760.61	20	Turbidite	Gas	Darker sand	1760.61	NM	NM
S3	20	Turbidite	Gas	Shale	1745.4	NM	NM

Table 5.1: Summary of the reservoir rock samples used in the study. Abbreviation: (NM) - not measured, (NK) - not known.

Titanomagnetite $10^{-6}m^3kg^{-1}$	Single domain $10^{-6}m^3kg^{-1}$	Ultrafine $10^{-6}m^3kg^{-1}$	% Fraction	ppm
20	60	100	10	100000
2	6	10	1	10000
0.2	0.6	1	0.1	1000
0.02	0.06	0.1	0.01	100
0.002	0.006	0.01	0.001	10
0.0002	0.0006	0.001	0.0001	1
0.00002	0.00006	0.0001	0.00001	0.1

Table 5.2: Magnetic susceptibility of magnetite and its percent fraction in various domain states (based on John Dearing, 1999).

	Crystal diameter (μm)	Crystal concentration (ppm)	Crystal volume (μm^3)	Surface area (μm^2)	No. of crystals in $10cm^3$ pot	Total mineral surface area in $10cm^3$ pot
SP	0.02	1	4×10^{-6}	1×10^{-3}	1×10^{12}	1×10^{9}
SSD	0.2	1.6	4×10^{-3}	2×10^{-1}	2×10^{9}	3×10^{8}
MD	200	5	4×10^{-6}	6×10^{5}	6×10^{0}	8×10^{-5}

Table 5.3: Numbers, volumes and total surface area of SP, SSD and MD magnetite crystals in a $10cm^3$ pot of soil with bulk $\chi_{Lfld} = 0.001\times10^{-6}m^3kg^{-1}$ calculated assuming spherical crystals ($v=4/3\pi r^3$; $a=4\pi r^2$) and 50% porosity (based on John Dearing, 1999).

Sample	Hc (mT)	Hcr (mT)	Mrs (10^{-6} Am^2kg^{-1})	Ms (10^{-6} Am^2kg^{-1})	Hcr/Hc	Mrs/Ms	SIRM (10^{-6} Am^2kg^{-1})	L_{fld} mass magnetic susceptibility (10^{-8} m^3kg^{-1})	H_{fld} mass magnetic susceptibility (10^{-8} m^3kg^{-1})	Mass ferro-magnetic susceptibility (10^{-8} m^3kg^{-1})	Natural remanent magnetisation (10^{-8} Am^2kg^{-1})
P21.0	14.995	25.192	0.070	0.370	1.680	0.259	0.078	-0.225	-0.523	0.298	65.1
P28.6	10.000	12.220	0.040	0.170	1.222	0.235	0.189	-0.202	-0.440	0.221	19.3
P81.3	10.025	32.080	0.094	0.589	3.200	0.160	0.120	1.256	0.290	0.966	28.5
P84.0	15.000	42.017	0.060	0.350	2.801	0.171	0.140	-0.239	-0.539	0.300	12.5
P812.2	14.992	43.432	0.065	0.430	2.897	0.151	0.070	0.267	-0.208	0.475	5.4
M28	8.021	30.108	0.045	0.300	3.754	0.185	0.075	0.582	0.225	0.358	4.0
M68	7.000	25.350	0.040	0.217	3.621	0.184	0.080	-0.360	-0.559	0.198	4.8
1750.24	9.013	49.659	0.600	5.000	5.510	0.120	0.374	8.609	2.036	6.573	66.8
1760.61	10.000	29.825	2.500	19.000	2.983	0.332	4.821	24.959	4.265	20.694	112.7
S3	11.970	35.290	5.000	23.000	2.948	0.217	4.414	93.967	11.480	82.487	1057.9

Table 5.4: Room temperature magnetic properties of representative reservoir rock samples.

Sample	Temp. (°C)	Modelled depth (m)	Type of reservoir sedimentary environment	Sediment	Ms (10^{-6} Am^2kg^{-1})	Mrs (10^{-6} Am^2kg^{-1})	Hc (mT)	Hcr (mT)	Mrs/Ms	Hcr/Hc	Applied field (mT)	L_{fld} mass magnetic susceptibility (10^{-8} m^3kg^{-1})	H_{fld} (para/dia) mass magnetic susceptibility (10^{-8} m^3kg^{-1})	Mass ferro-magnetic susceptibility (10^{-8} m^3kg^{-1})
P81.3	25	495	Shoreface	Dogger	0.589	0.094	10.025	32.080	0.160	3.200	10	1.256	0.290	0.966
P81.3	89	2607	Shoreface	Dogger	0.598	0.080	8.101	26.329	0.134	3.250	10	1.931	0.112	1.819
P81.3	125	3795	Shoreface	Dogger	0.621	0.070	6.989	23.203	0.120	3.320	10	1.819	0.025	1.794
P81.3	245	7755	Shoreface	Dogger	0.627	0.050	2.991	10.768	0.080	3.600	10	1.308	-0.155	1.463
P21	25	495	Shoreface	Sandstone	0.370	0.070	14.995	25.192	0.259	1.680	10	-0.225	-0.523	0.298
P21	89	2607	Shoreface	Sandstone	0.350	0.055	9.012	15.411	0.157	1.710	10	0.549	-0.566	1.115
P21	125	3795	Shoreface	Sandstone	0.400	0.050	11.021	19.199	0.125	1.742	10	0.566	-0.582	1.148
P21	245	7755	Shoreface	Sandstone	0.300	0.045	8.000	17.144	0.150	2.143	10	0.201	-0.610	0.811
P28.6	25	495	Shoreface	Muddy sandstone	0.170	0.040	10.000	12.220	0.235	1.222	10	-0.202	-0.440	0.221
P28.6	89	2607	Shoreface	Muddy sandstone	0.178	0.025	9.000	11.250	0.140	1.250	10	0.152	-0.473	0.625
P28.6	125	3795	Shoreface	Muddy sandstone	0.219	0.020	6.982	9.000	0.091	1.289	10	0.088	-0.491	0.579
P28.6	245	7755	Shoreface	Muddy sandstone	0.100	0.015	3.000	5.820	0.150	1.940	10	-0.158	-0.509	0.350
P28.6	464	14982	Shoreface	Muddy sandstone	16.990	2.130	0.992	4.339	0.125	4.374	10	0.904	-0.001	0.904
P84	25	495	Shoreface	Sandstone	0.350	0.060	15.000	42.017	0.171	2.801	10	-0.239	-0.539	0.300
P84	89	2607	Shoreface	Sandstone	0.340	0.050	11.010	31.446	0.147	2.856	10	0.366	-0.567	0.932
P84	125	3795	Shoreface	Sandstone	0.340	0.045	9.000	26.213	0.132	2.913	10	0.349	-0.579	0.928
P84	245	7755	Shoreface	Sandstone	0.310	0.030	8.000	25.600	0.097	3.200	10	0.207	-0.593	0.801
P812.2	25	495	Shoreface	Micaceous sandstone	0.430	0.065	14.992	43.432	0.151	2.897	10	0.267	-0.208	0.475
P812.2	89	2607	Shoreface	Micaceous sandstone	0.400	0.055	13.012	38.401	0.138	2.951	10	0.501	-0.277	0.778

P812.2	125	3795	Shoreface	Micaceous sandstone	0.380	0.040	9.000	26.933	0.105	2.993	10	0.797	-0.307	1.104
P812.2	245	7755	Shoreface	Micaceous sandstone	0.350	0.030	7.000	23.534	0.086	3.362	10	0.487	-0.394	0.881
M28	25	495	HPHT	Sandstone	0.300	0.045	8.021	30.108	0.185	3.754	10	0.582	0.225	0.358
M28	89	2607	HPHT	Sandstone	0.240	0.042	11.000	42.076	0.176	3.825	10	0.855	0.061	0.794
M28	125	3795	HPHT	Sandstone	0.240	0.036	14.982	58.580	0.150	3.910	10	0.979	-0.013	0.992
M28	245	7755	HPHT	Sandstone	0.240	0.048	1.000	3.625	0.201	3.625	10	0.778	-0.144	0.922
M68	25	495	HPHT	Sandstone	0.217	0.040	7.000	25.350	0.184	3.621	10	-0.360	-0.559	0.198
M68	89	2607	HPHT	Sandstone	0.236	0.029	10.000	35.520	0.123	3.552	10	-0.062	-0.591	0.528
M68	125	3795	HPHT	Sandstone	0.295	0.025	9.998	34.913	0.085	3.492	10	-0.146	-0.606	0.461
M68	245	7755	HPHT	Sandstone	0.267	0.020	5.000	18.605	0.075	3.721	10	-0.143	-0.628	0.485
1750.24	25	495	Turbidite	White sand	5.000	0.600	9.013	49.659	0.120	5.510	1750.24	8.609	2.036	6.573
1750.24	89	2607	Turbidite	White sand	4.600	0.400	7.000	39.347	0.087	5.621	1750.24	13.004	1.378	11.627
1750.24	125	3795	Turbidite	White sand	4.400	0.350	6.950	39.775	0.080	5.723	1750.24	11.725	1.179	10.546
1750.24	245	7755	Turbidite	White sand	3.600	0.200	5.000	29.345	0.056	5.869	1750.24	9.418	0.704	8.714
1760.61	25	495	Turbidite	Darker sand	19.000	2.500	10.000	29.825	0.332	2.983	10	24.959	4.265	20.694
1760.61	89	2607	Turbidite	Darker sand	17.500	2.000	9.010	27.950	0.312	3.102	10	48.856	3.357	45.499
1760.61	125	3795	Turbidite	Darker sand	17.000	1.800	8.000	25.716	0.306	3.215	10	47.636	2.972	44.664
1760.61	245	7755	Turbidite	Darker sand	14.700	1.500	5.000	15.123	0.372	3.025	10	39.822	2.016	37.805
S3	25	495	Turbidite	Shale	23.000	5.000	11.970	35.290	0.217	2.948	10	93.967	11.480	82.487
S3	89	2607	Turbidite	Shale	16.000	3.000	10.600	31.588	0.188	2.980	10	80.255	9.129	71.125
S3	125	3795	Turbidite	Shale	12.000	2.000	9.770	29.680	0.167	3.038	10	65.246	7.407	57.838
S3	245	7755	Turbidite	Shale	9.000	1.287	5.350	21.270	0.143	3.976	10	52.671	5.392	47.279

Table 5.5: High temperature magnetic properties of representative reservoir rock samples at applied fields of 10mT.

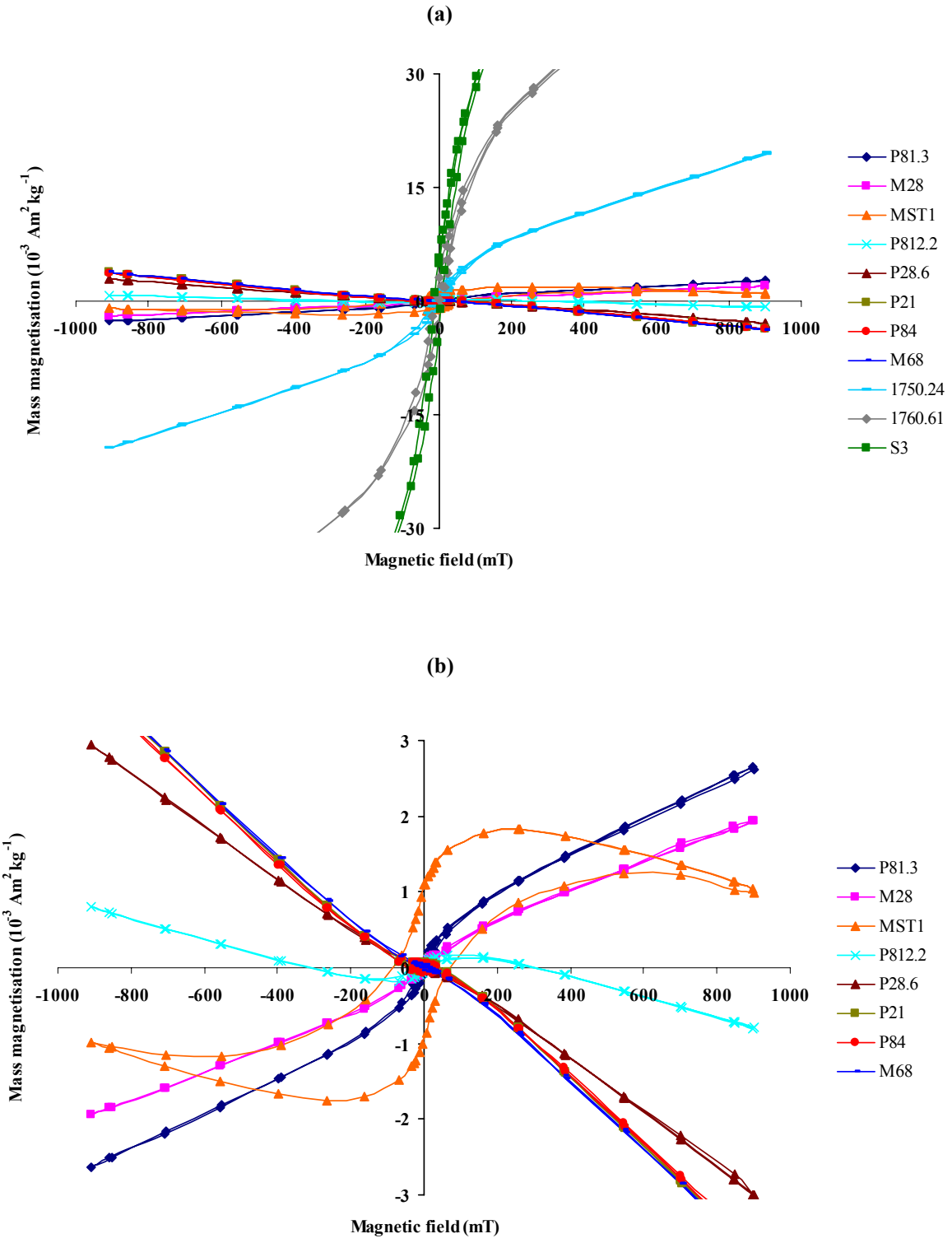

Figure 5.1: (a) shows room temperatue hysteresis curves for shoreface reservoir I & II samples (P21, P28.6, P812.2, P84 and P81.3), HPHT shallow marine samples (M68 and M28), turbidite samples (S3, 1760.61 and 1750.24), and a hematite sample MST1. Sample S3 is a shale with the highest positive high field slope. (b) shows the magnified hysteresis loops excluding highly paramagnetic turbidite samples (S3, 1760.61 and 1750.24). Sample M68 is relatively cleaner sand with the highest negative high field slope.

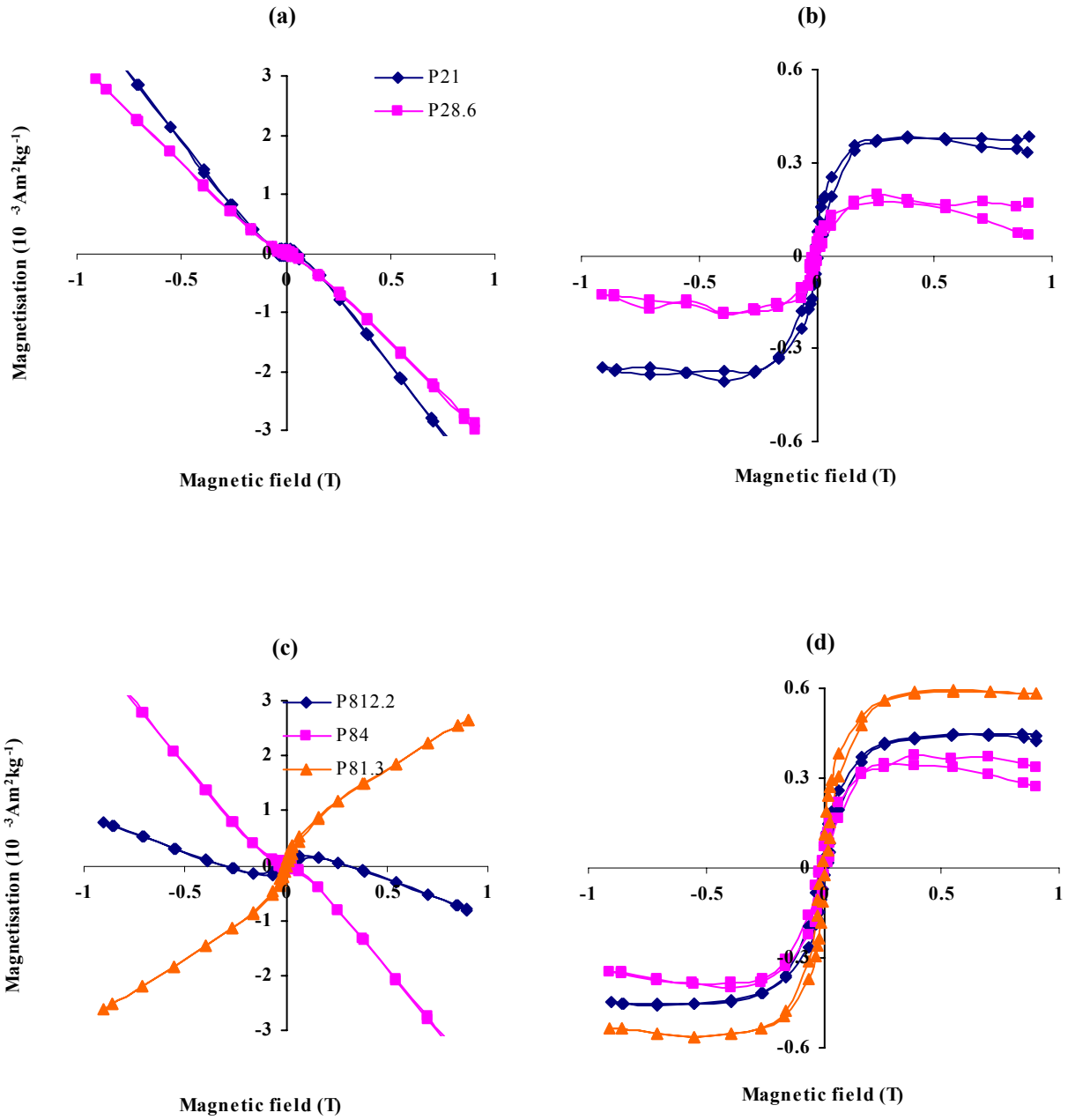

Figure 5.2: (a) and (c) represent the magnetic hysteresis loops for shoreface reservoir I samples (P21 and P28.6) and shoreface reservoir II samples (P812.2, P84 and P81.3) respectively. Their corresponding ferromagnetic hysteresis loops (b) and (d) are shown on the right after subtracting the paramagnetic/diamagnetic components.

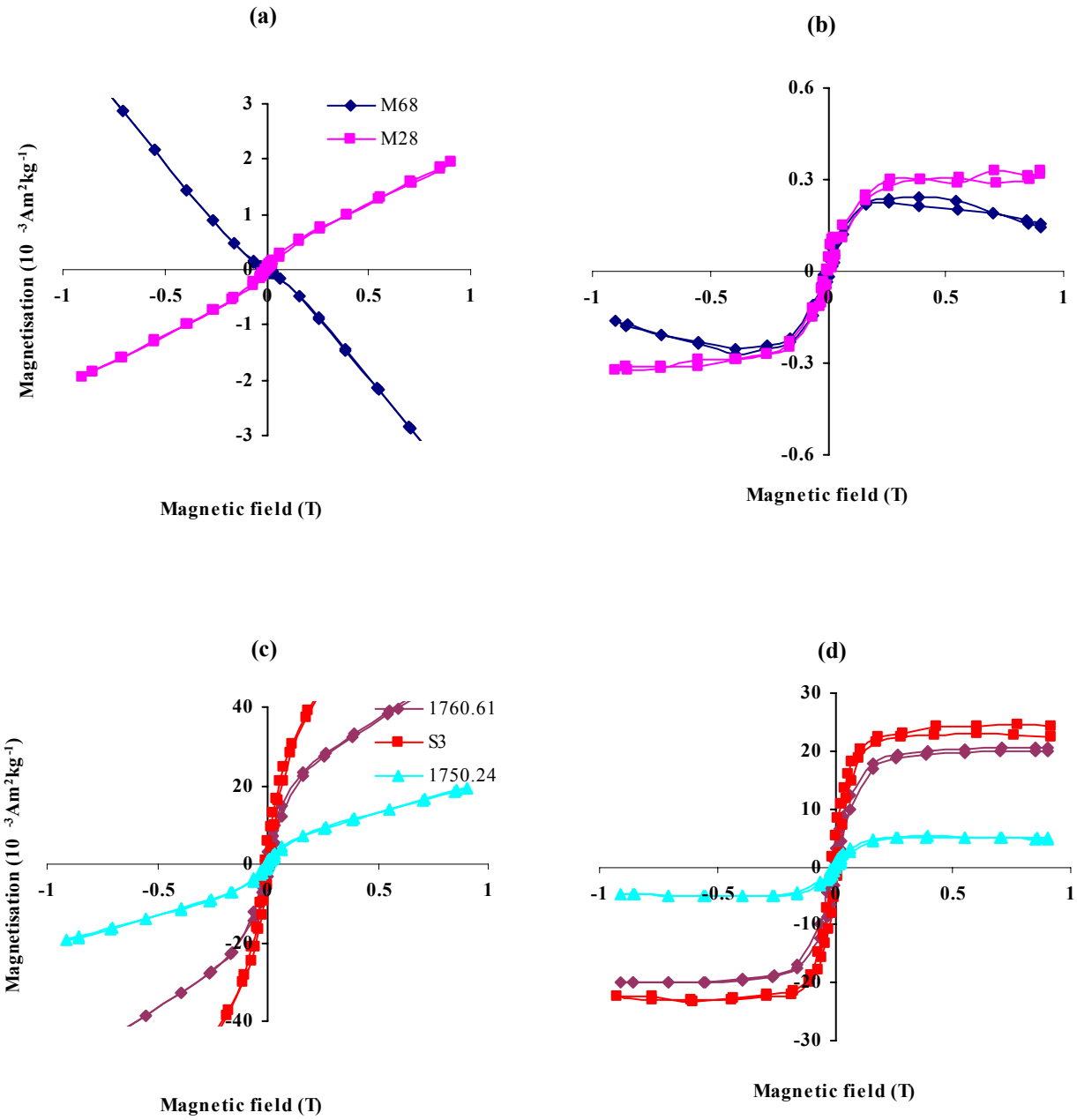

Figure 5.3: (a) and (c) represent the magnetic hysteresis loops for HPHT shallow marine reservoir samples (M68 and M28) and turbidite samples (S3, 1760.61 and 1750.24). Their corresponding ferromagnetic hysteresis loops (b) and (d) are shown on the right after subtracting the paramagnetic/diamagnetic components. Sample S3 (a shale) is rich in ferromagnetic component and so is sample 1760.61 which is a darker sand. The HPHT shallow marine samples which represent clean sandstone contain a lot less ferromagnetic component.

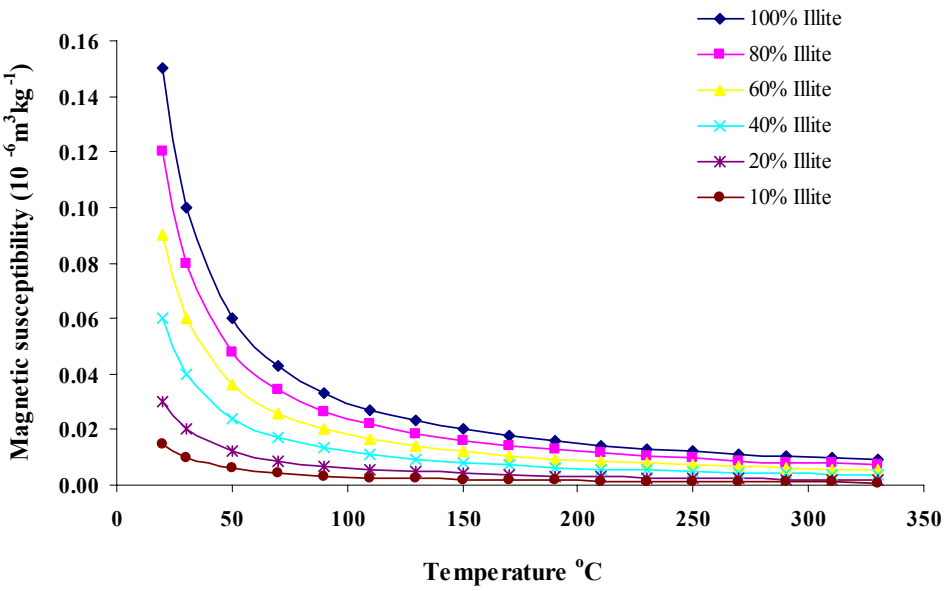

Figure 5.4: Theoretical magnetic susceptibility versus temperature curves for a mixture of Illite+Quartz. The curves above assume that quartz magnetic susceptibility (diamagnetic) is unaffected by temperature.

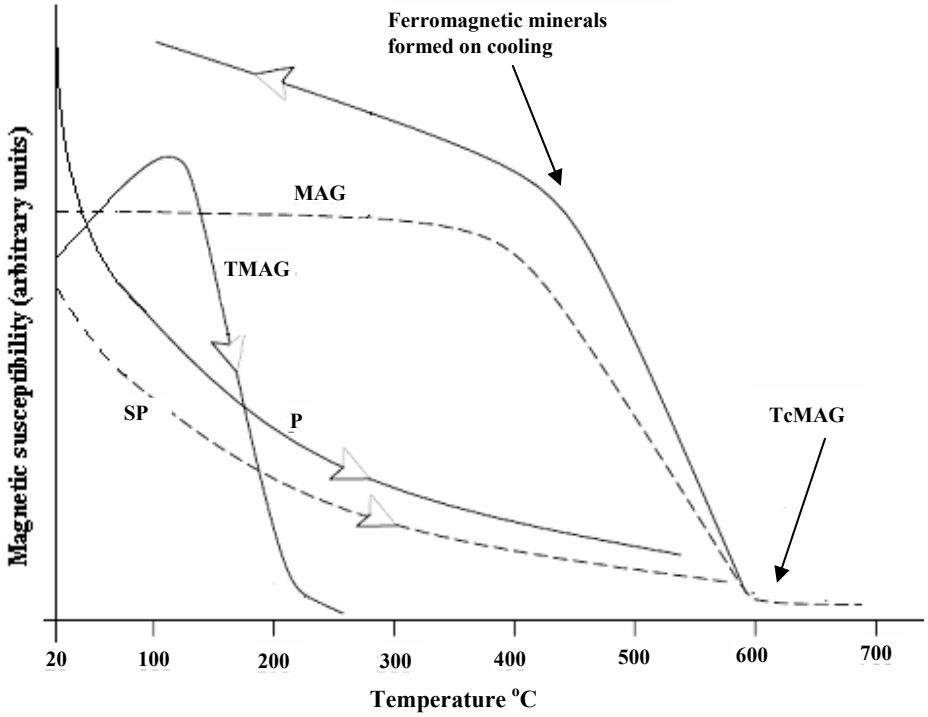

Figure 5.5: Schematic trends and transitions of low field (L_{fld}) magnetic susceptibility values from room temperature to +700 °C for different minerals and domains; superparamagnetic (SP), paramagnetic (P), magnetite (MAG: Tc 580 °C), titanomagnetite (TMAG: Tc 250 °C). Susceptibility axis not to scale. (based on Thomson and Oldfield 1986).

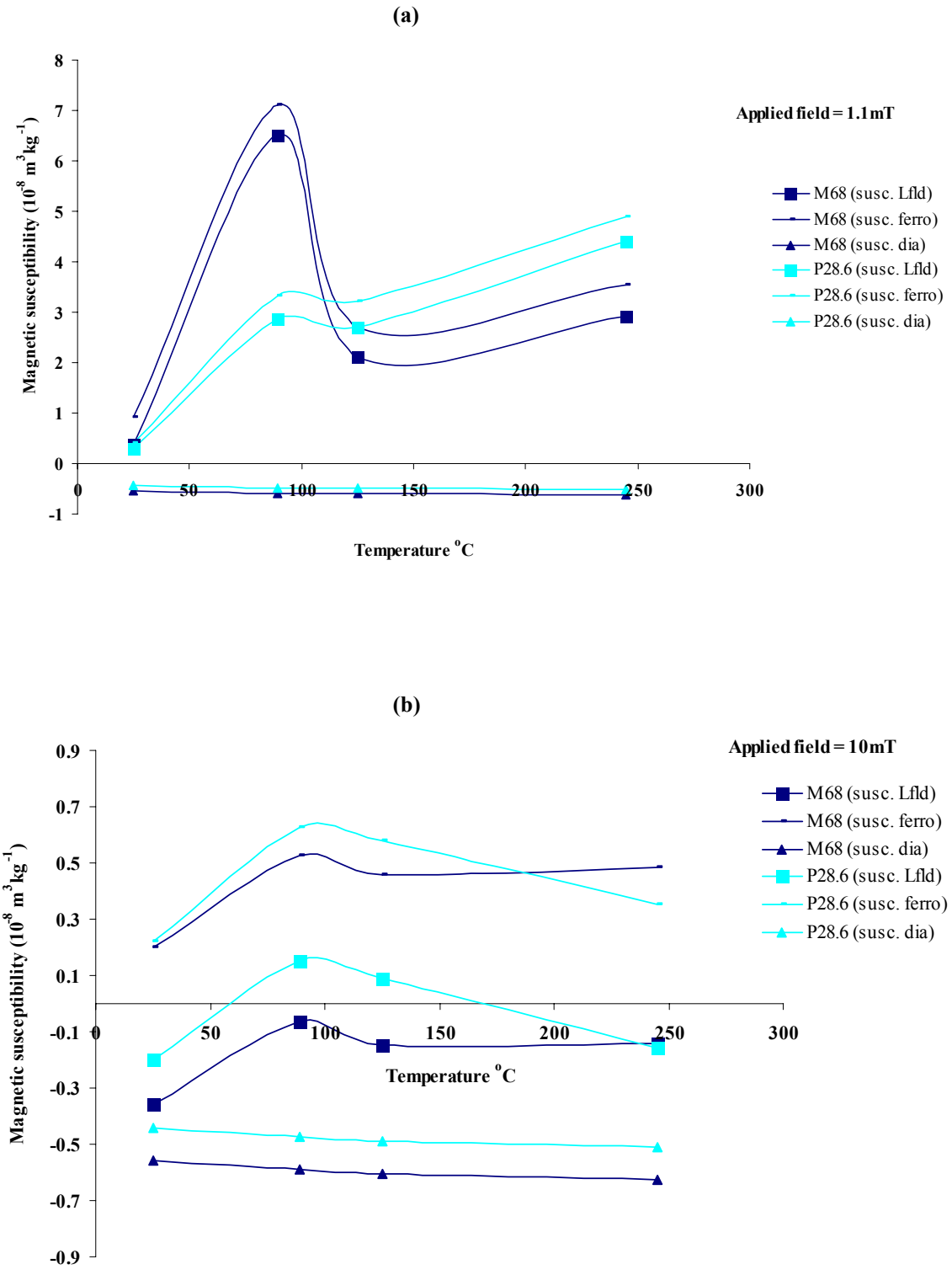

Figure 5.6: Susceptibility versus temperature curves, measured at 1.1mT and 10mT applied fields, for two samples having mainly diamagnetic matrix and a small ferromagnetic component.

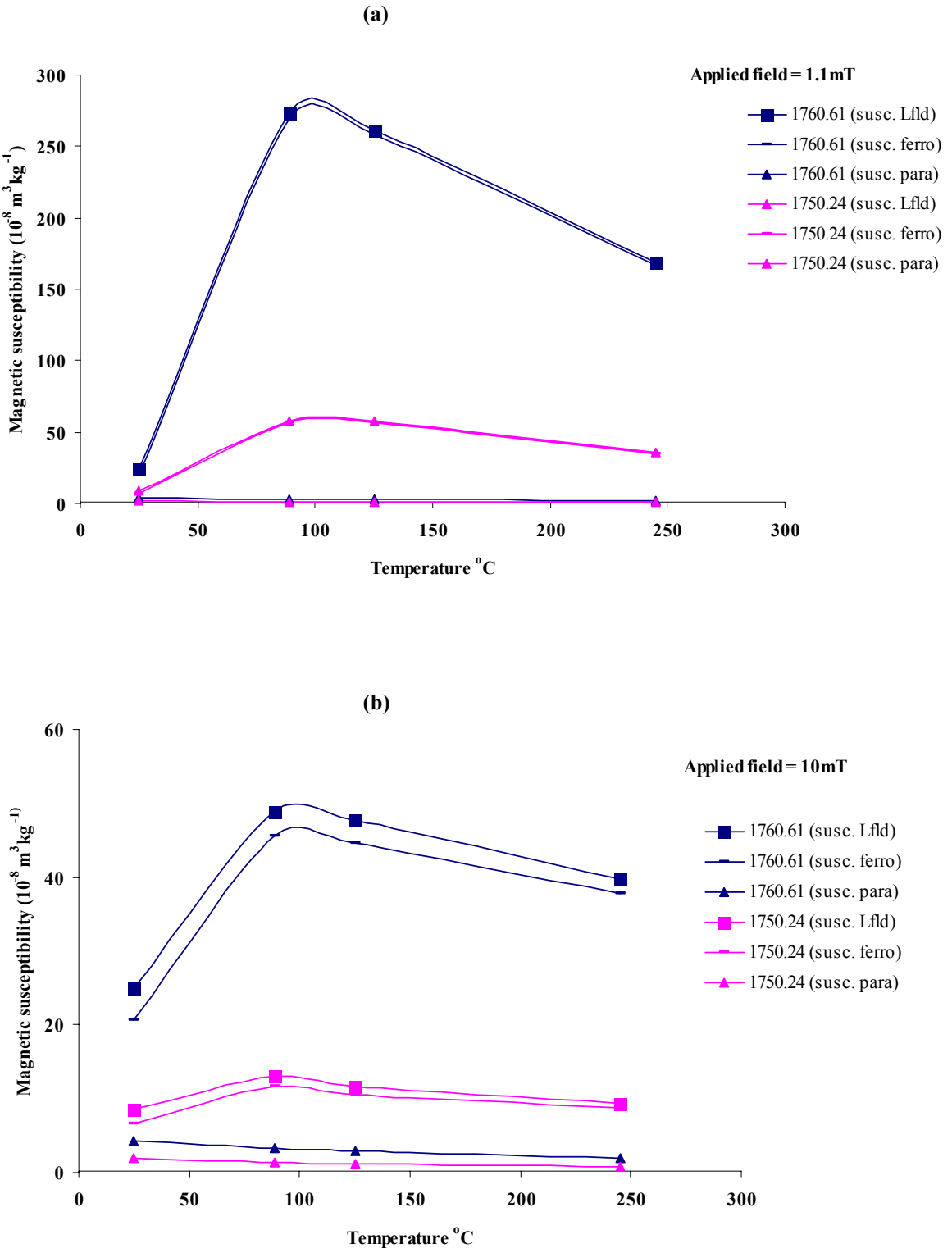

Figure 5.7: Susceptibility versus temperature curves, measured at 1.1mT and 10mT applied fields, for two samples having mainly paramagnetic matrix and a relatively large ferromagnetic component.

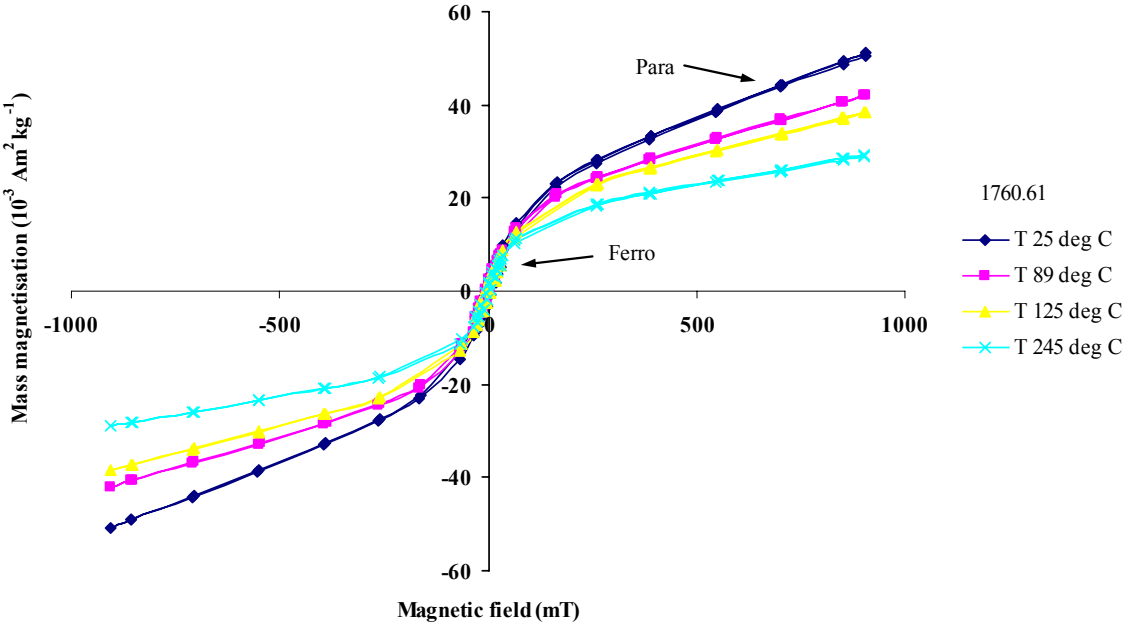

Figure 5.8: Change in slope with temperature for sample 1760.61 having a relatively higher ferromagnetic component. Magnetic susceptibility of ferromagnetic component slightly increases with temperature, whereas for paramagnetic component it decreases sharply with temperature. However, the predominant ferromagnetic component in the sample prohibits a sharp decrease in its slope with temperature. Therefore, the higher the ferromagnetic component in the sample, there will be less decrease in slope with temperature.

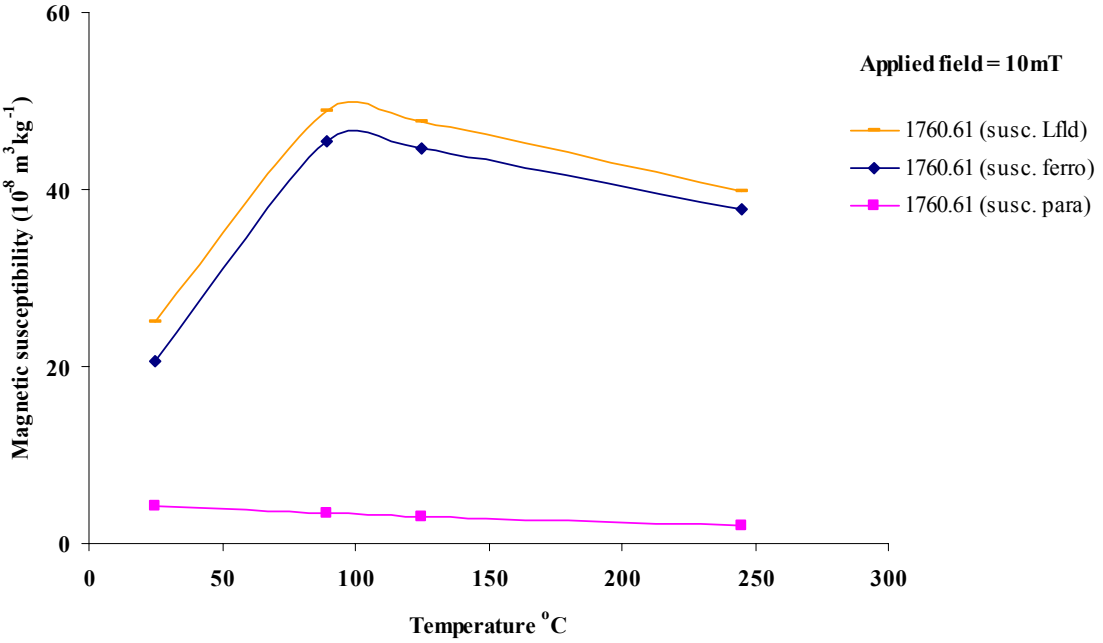

Figure 5.9: Variations in low field (Lfld), ferromagnetic and paramagnetic susceptibilities with temperature for sample 1760.61. The individual susceptibility curves help us identify what's happening to various magnetic minerals in the sample.

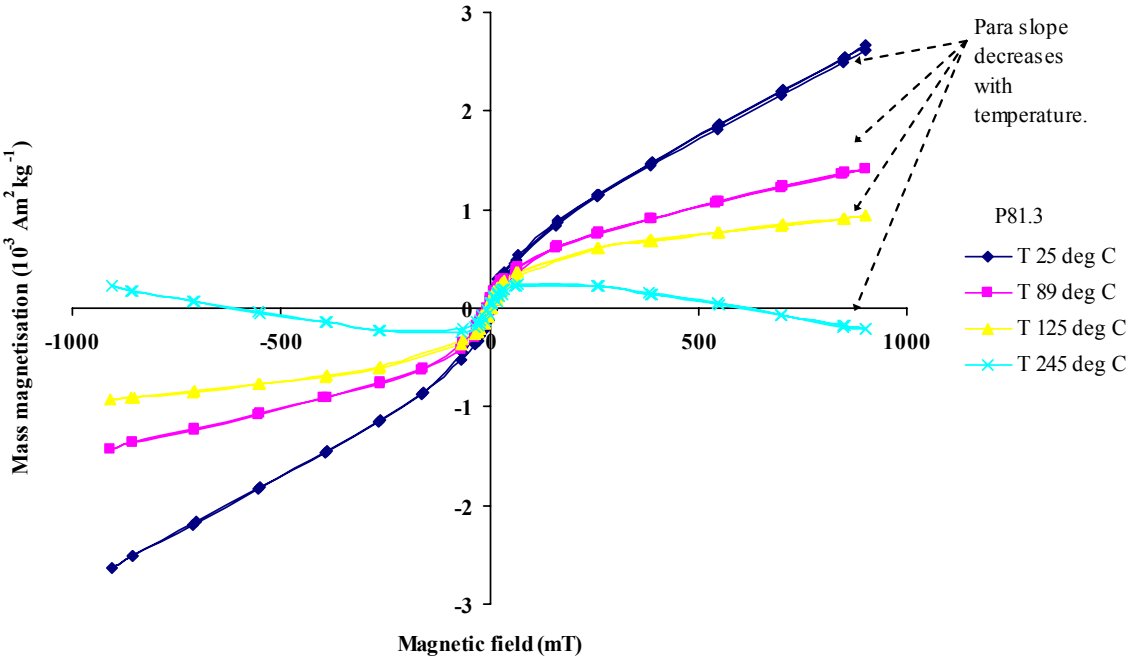

Figure 5.10: Change in slope with temperature for sample P81.3 having a small amount of ferromagnetic component. The susceptibility is mainly dominated by paramagnetic matrix. The high field slope decreases rapidly with an increase in temperature since the higher paramagnetic susceptibility overshadows the ferromagnetic component.

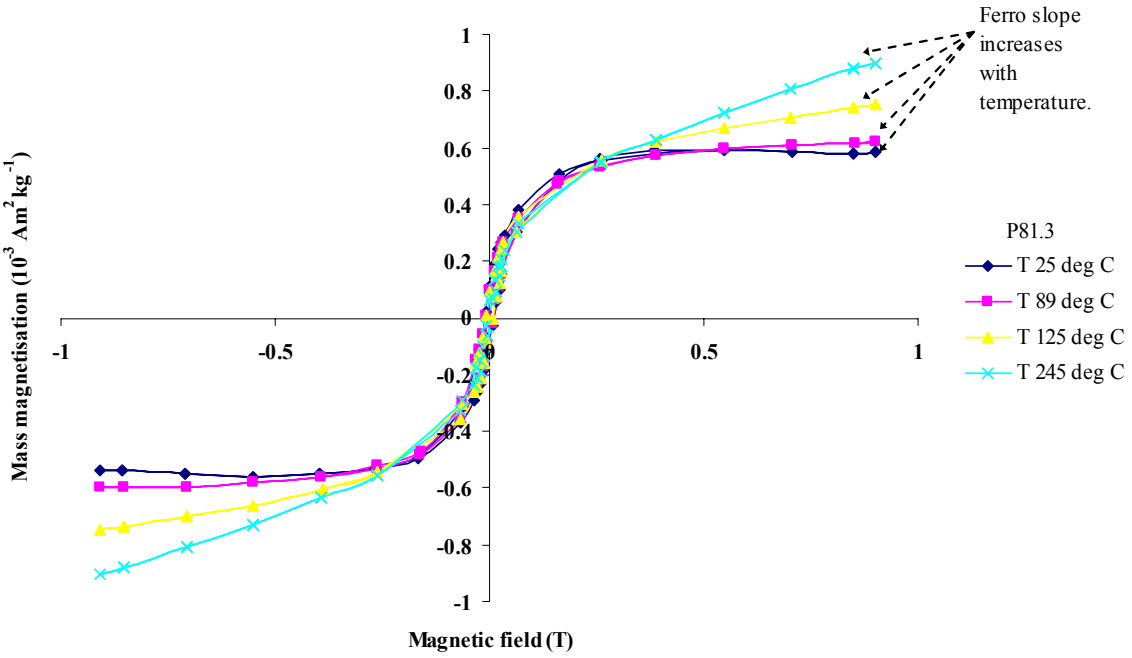

Figure 5.11: Effect of temperature on ferromagnetic component for sample P81.3. The high field ferromagnetic slope slightly increases with temperature. However the presence of large paramagnetic component overshadows this effect.

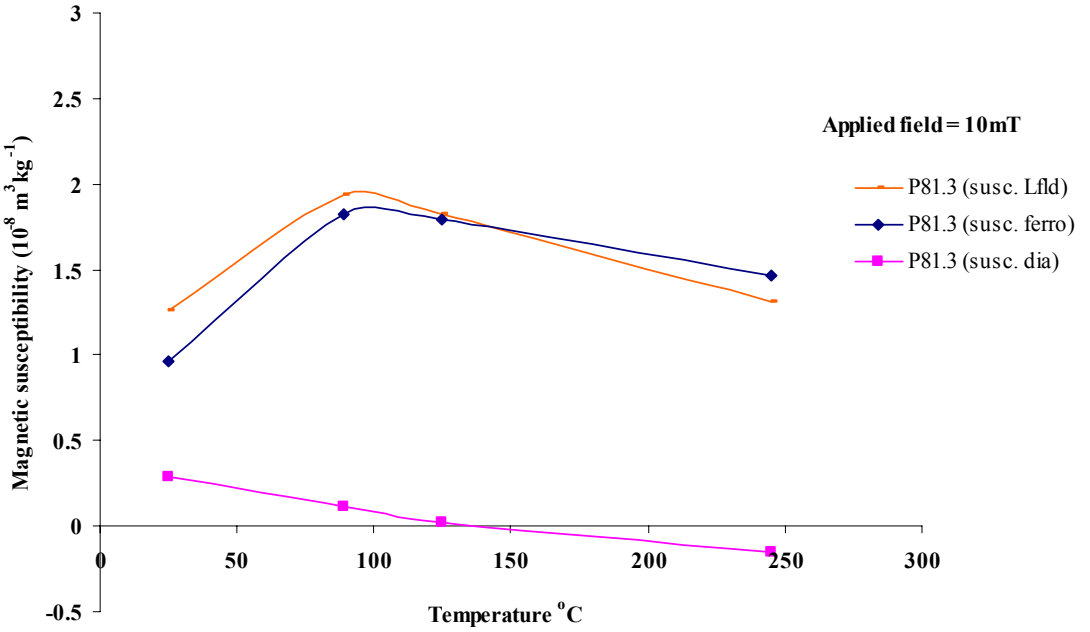

Figure 5.12: Variations in low field, ferromagnetic and paramagnetic susceptibilities with temperature. At around 140 °C, diamagnetic effect dominates and the slope becomes negative. This is also evident from the fact that ferromagnetic susceptibility becomes higher than L_{fld} susceptibility at this temperature.

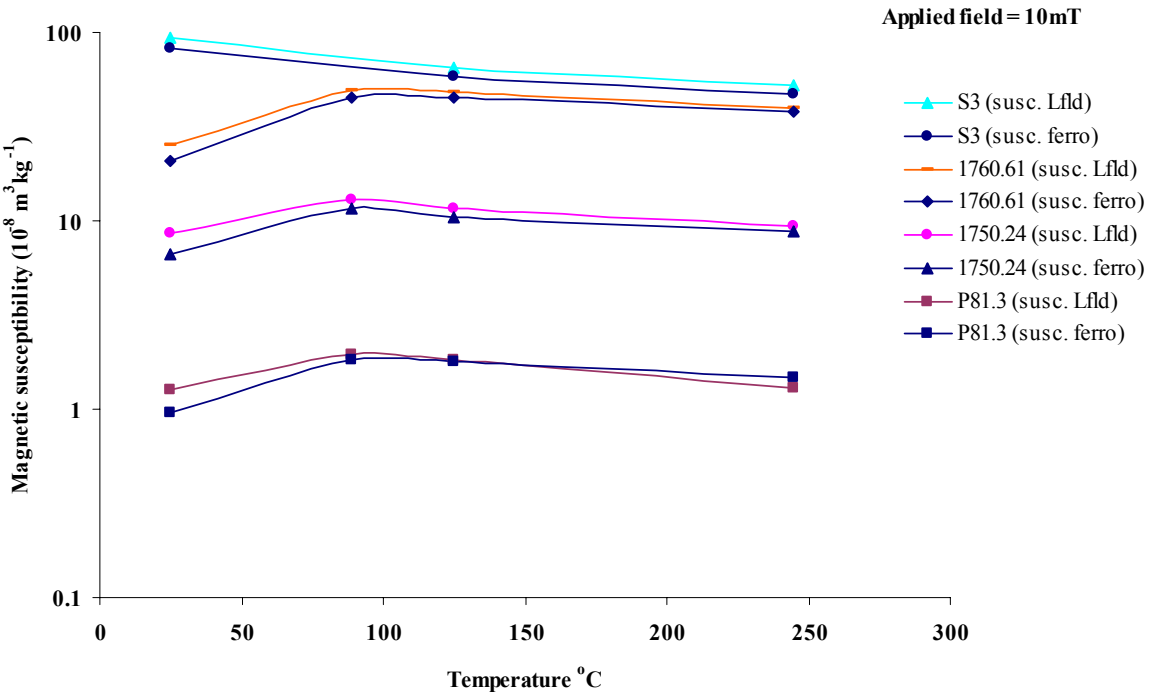

Figure 5.13: Experimental low field and ferromagnetic susceptibility (χ_{Lfld} and χ_{ferro}) versus temperature curves for samples having a paramagnetic matrix and the ferromagnetic component.

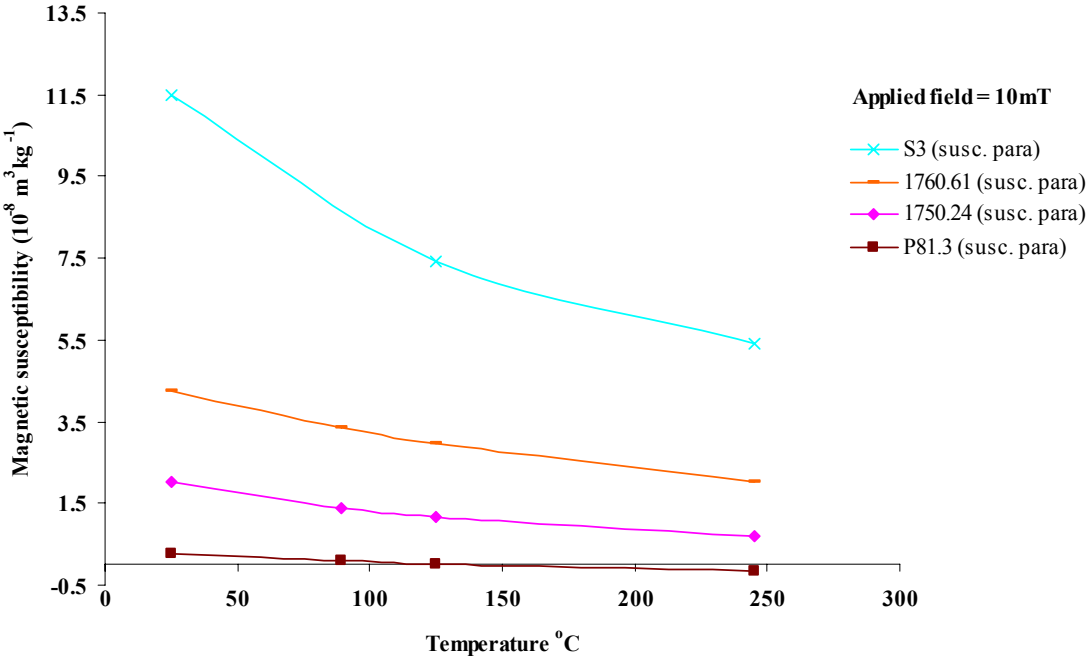

Figure 5.14: Experimental paramagnetic susceptibility (χ_{para}) versus temperature curves for reservoir samples having a paramagnetic matrix and a small ferromagnetic component.

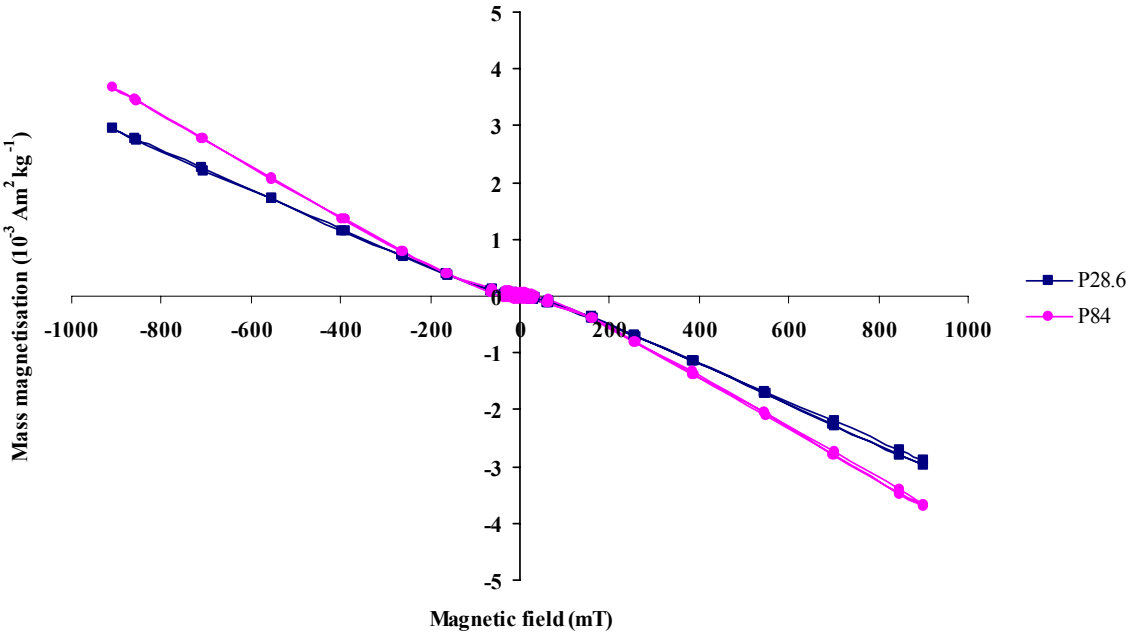

Figure 5.15: Hysteresis curves for samples P28.6 and P84. Both have almost the same ferromagnetic component. However, sample P28.6 has slightly higher paramagnetic component than P84. Theoretically, for the same ferromagnetic component, the low field susceptibility for sample P28.6 should decrease more rapidly compared to sample P84 (Figure 5.16).

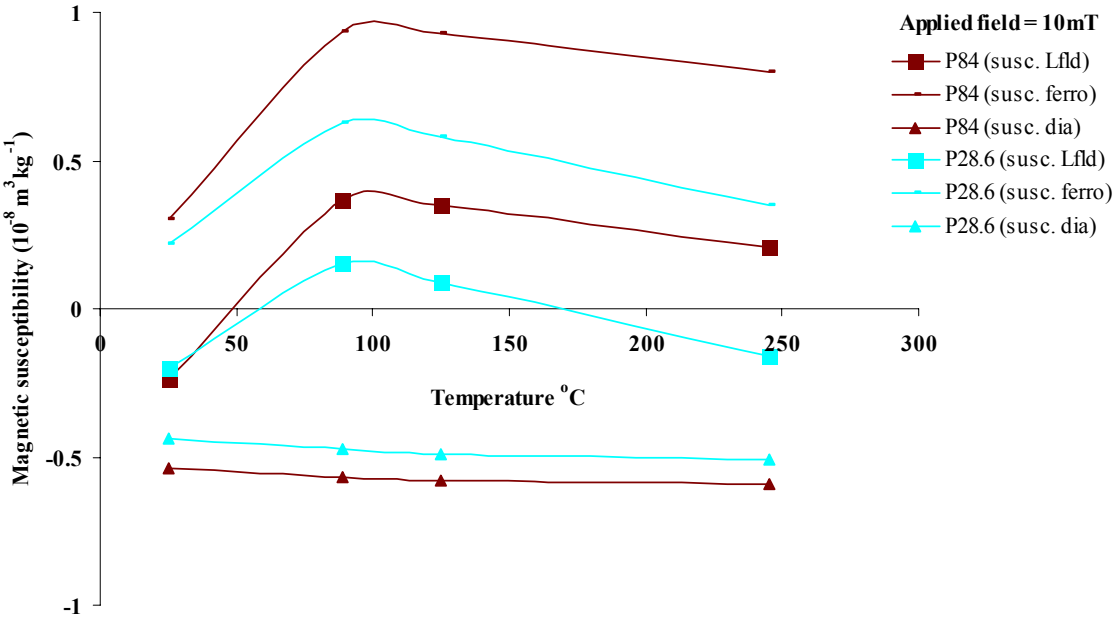

Figure 5.16: Sample P84 has a higher diamagnetic component whereas sample P28.6 contain paramagnetic impurities which can be seen by a lower magnitude diamagnetic susceptibility curve for sample P28.6.

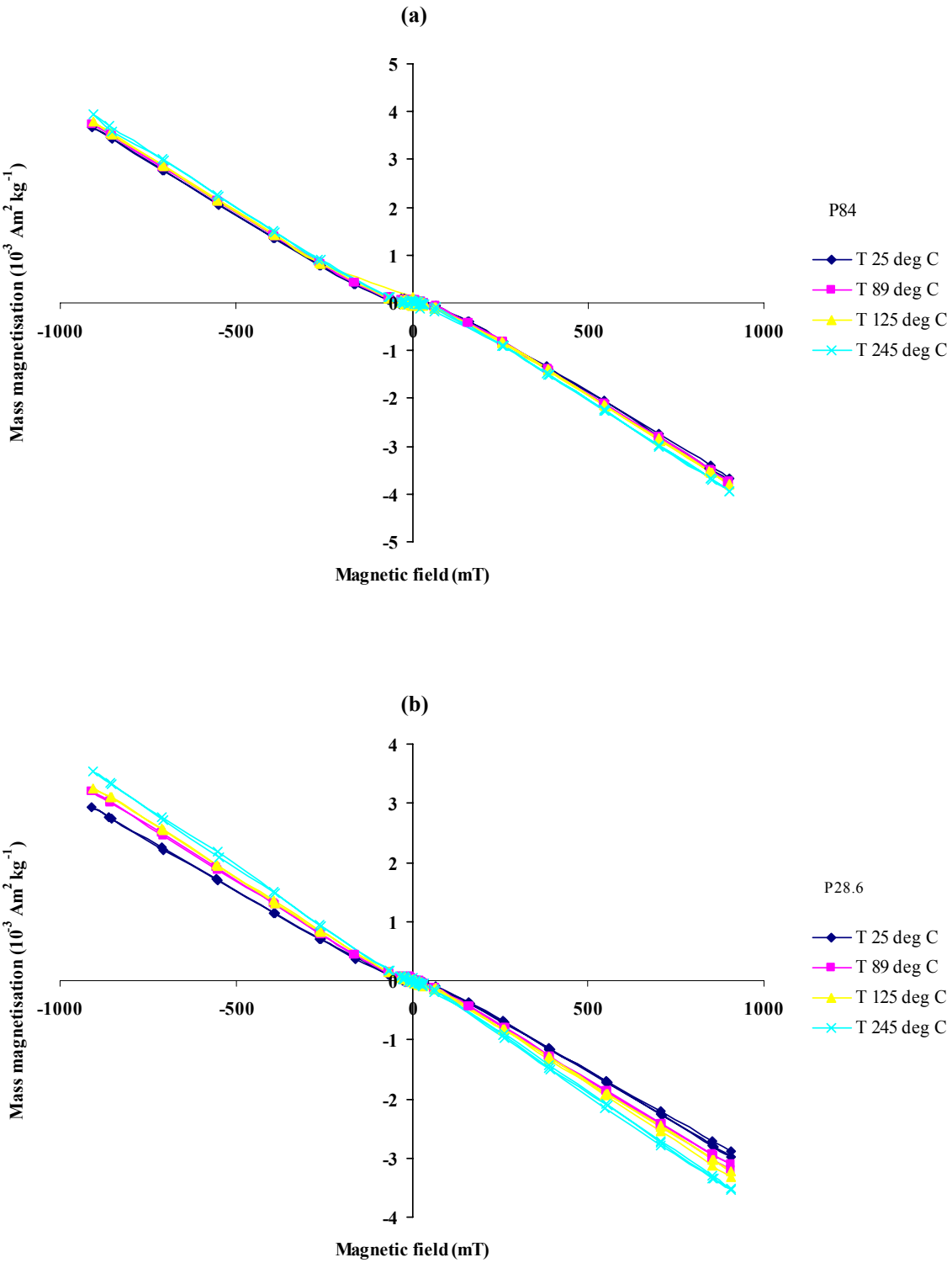

Figure 5.17: Change in high field slope with temperature for samples P84 and P28.6. Sample P84 mainly consists of a diamagnetic matrix whose susceptibility doesn't change with temperature. Sample P28.6 also has diamagnetic matrix as the main matrix mineral but also contains a tiny amount of paramagnetic clay. High field slope variations with temperature verifies this fact.

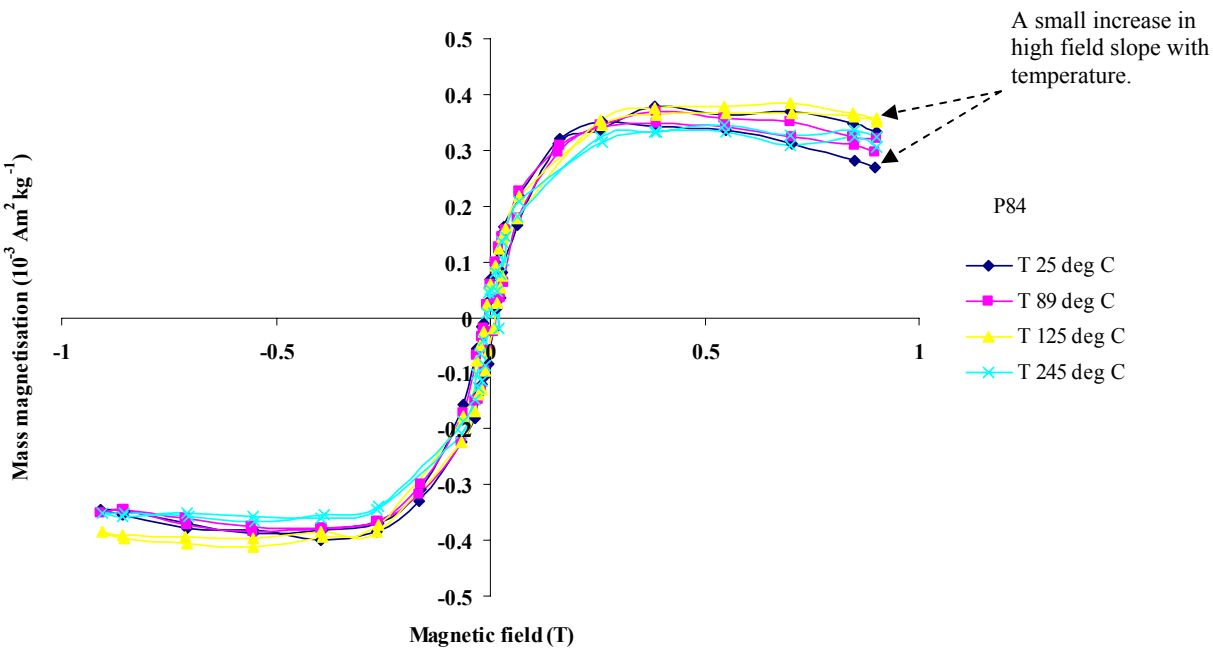

Figure 5.18: Changes in ferromagnetic hysteresis loops with temperature for sample P84.

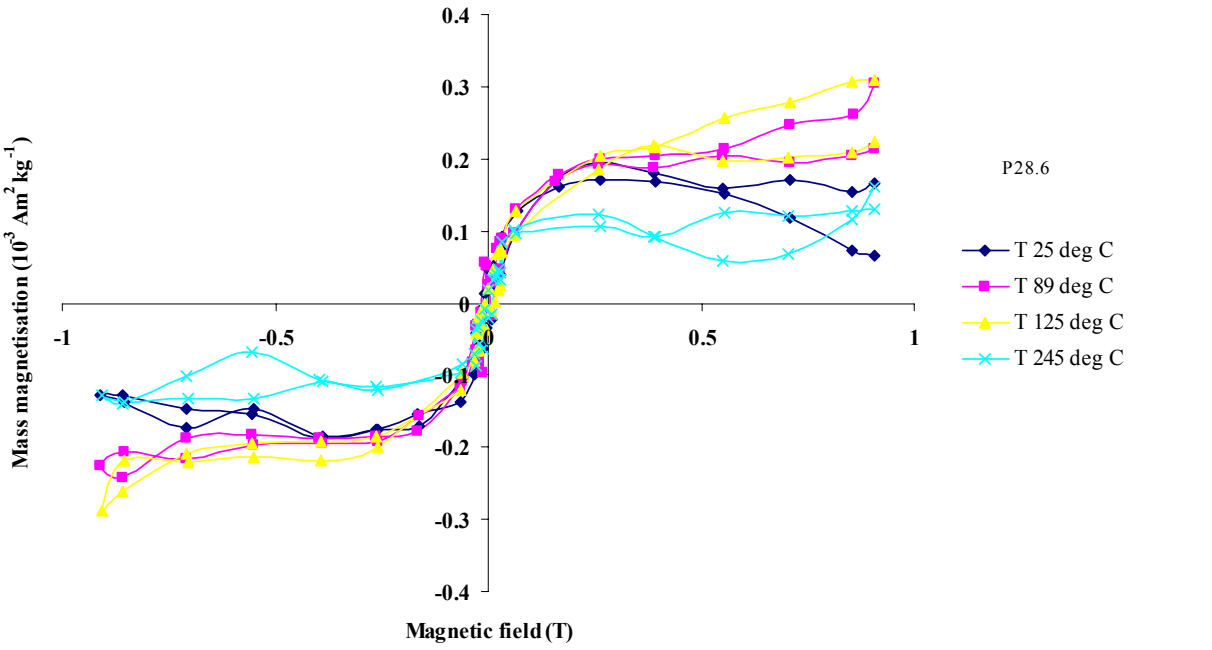

Figure 5.19: Changes in ferromagnetic hysteresis loops with temperature for sample P28.6.

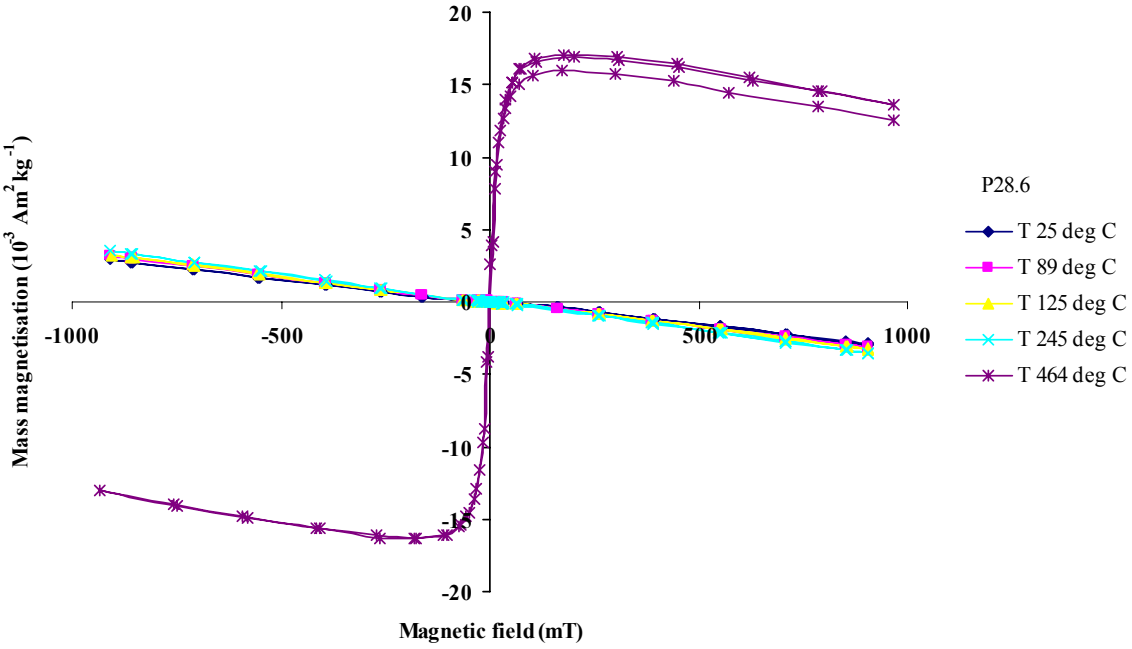

Figure 5.20: Formation of a new ferromagnetic component in sample P28.6 at high temperatures. This is shown by a large kink at low applied fields.

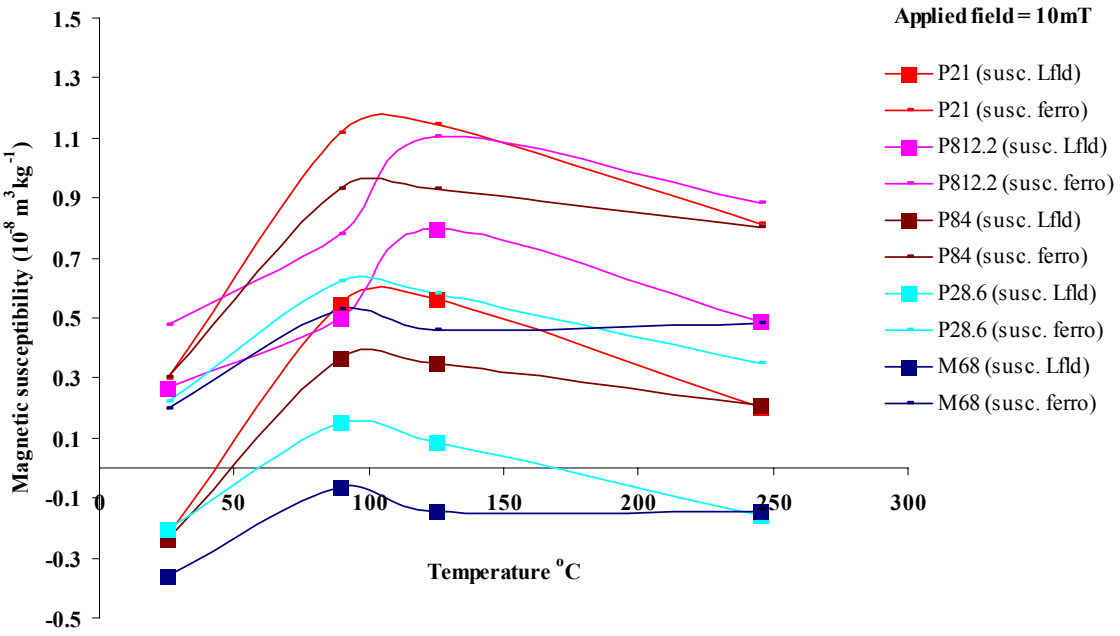

Figure 5.21: Experimental low field and ferromagnetic susceptibility (χ_{Lfld} and χ_{ferro}) versus temperature curves for samples having mainly diamagnetic matrix and a small ferromagnetic component.

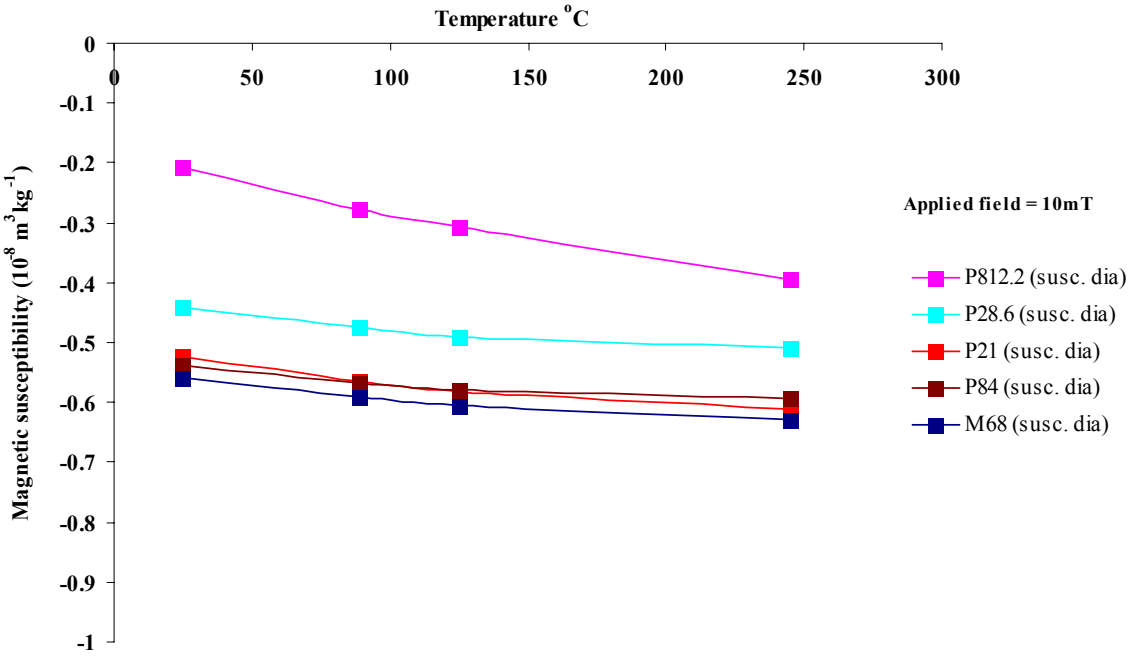

Figure 5.22: Experimental diamagnetic susceptibility (χ_{dia}) versus temperature curves for samples shown in Figure 5.21.

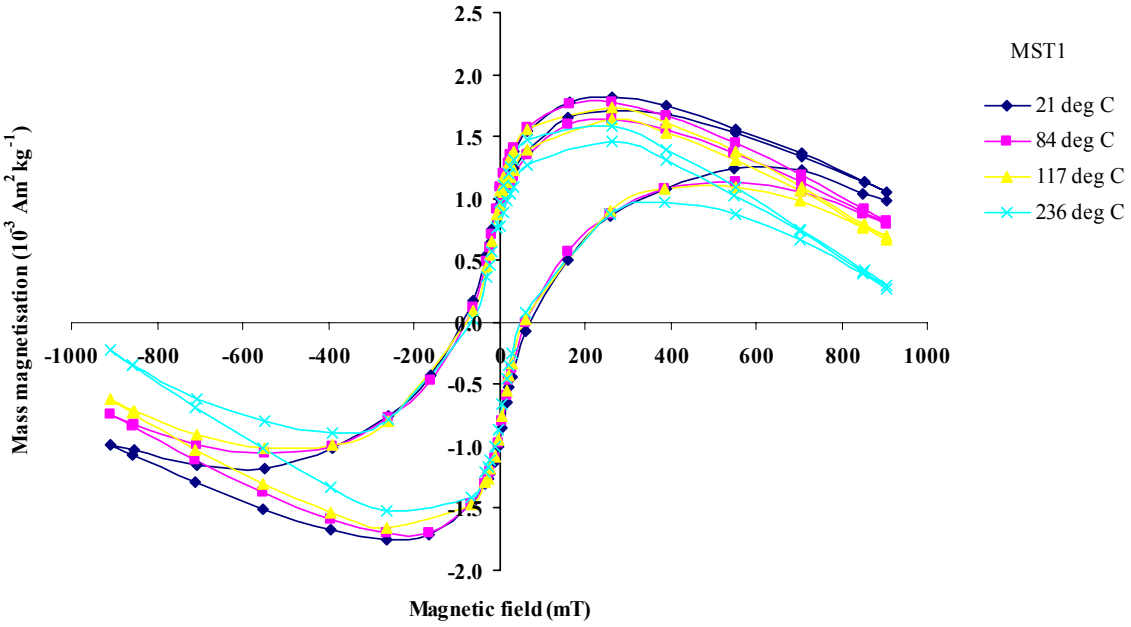

Figure 5.23: Changes in the slope of hysteresis curve with temperature for sample MST1 having an anti-ferromagnetic component (hematite) and a diamagnetic matrix (quartz).

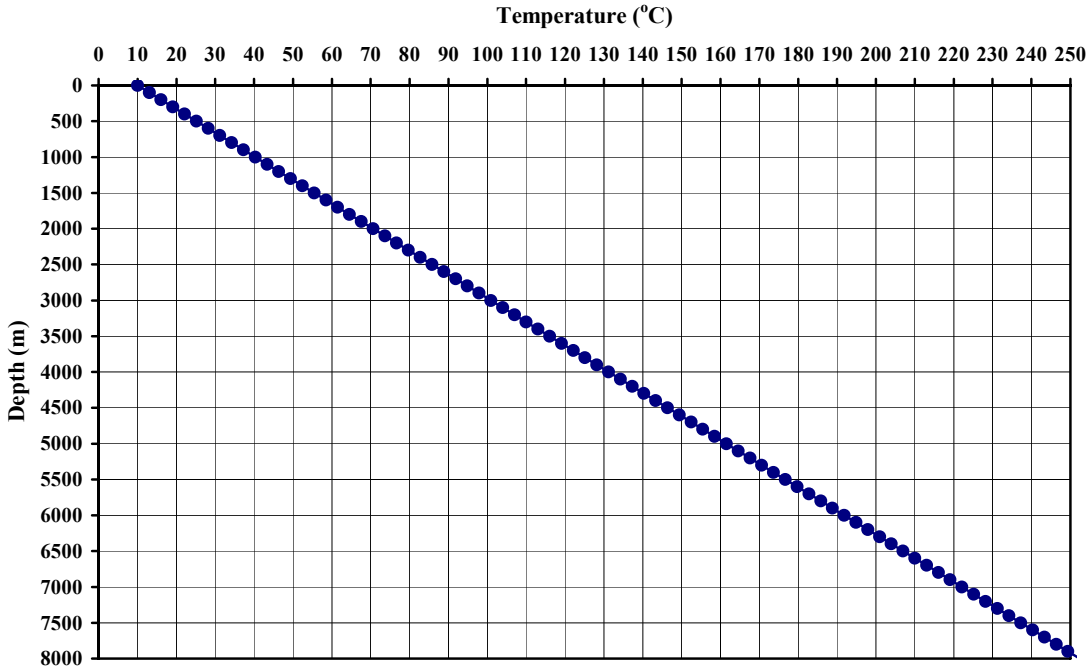

Figure 5.24: In-situ temperature gradient applicable for reservoir rock samples.

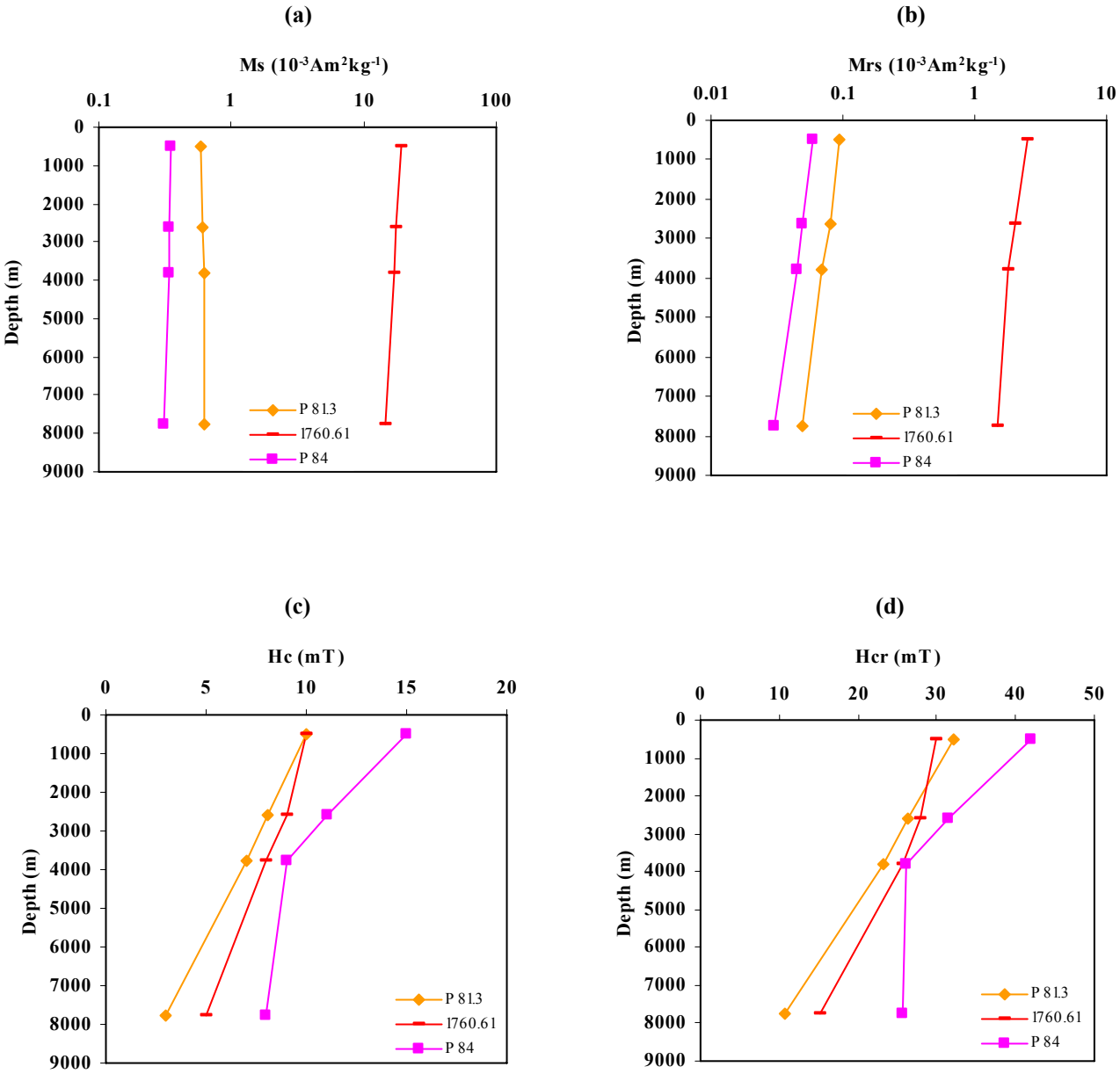

Figure 5.25: (a) and (b) represent the saturation magnetization (Ms) and saturation remanent magnetization (Mrs) for samples P81.3, 1760.61 and P84 respectively. (c) and (d) show the corresponding coercivity (Hc) and coercivity of remanence (Hcr) values for the three samples.

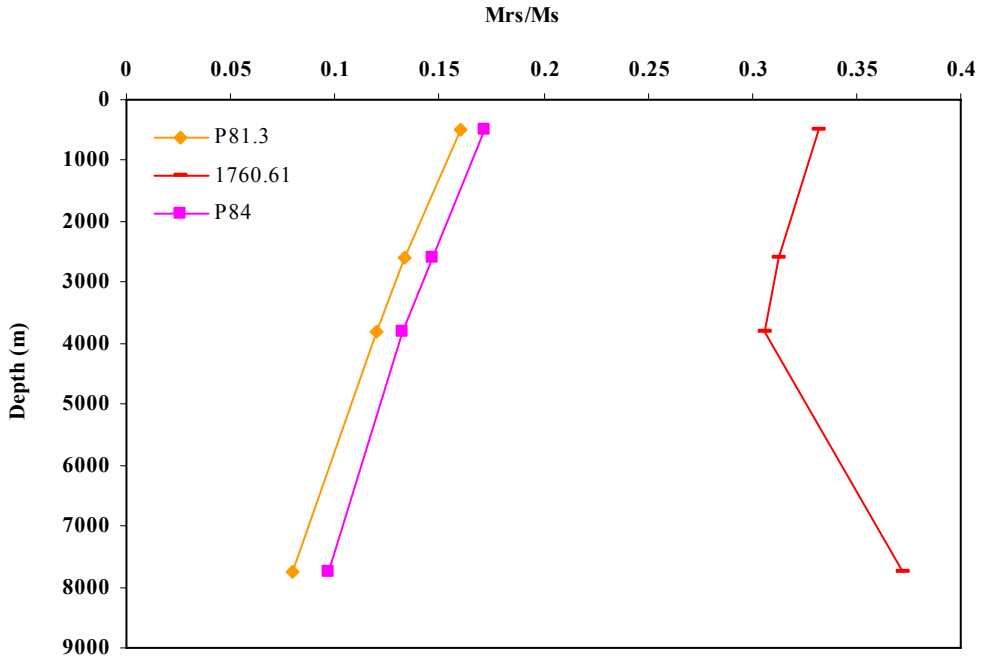

Figure 5.26: Dependence of remanence ratios with depth for samples P81.3, 1760.61 and P84.

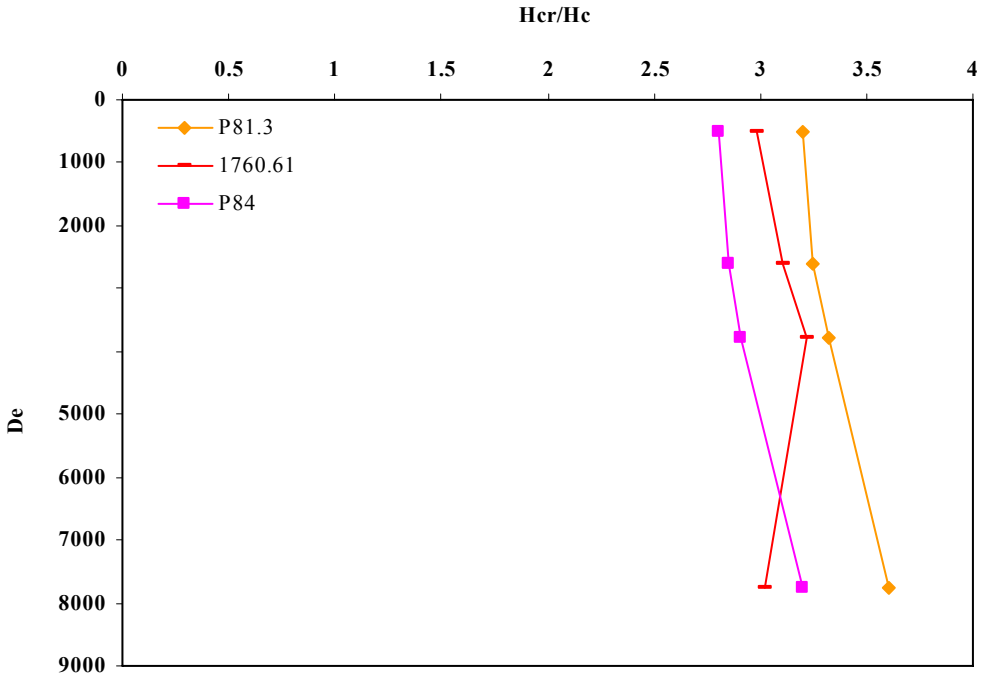

Figure 5.27: Dependence of coercivity ratios with depth for the representative sediment samples.

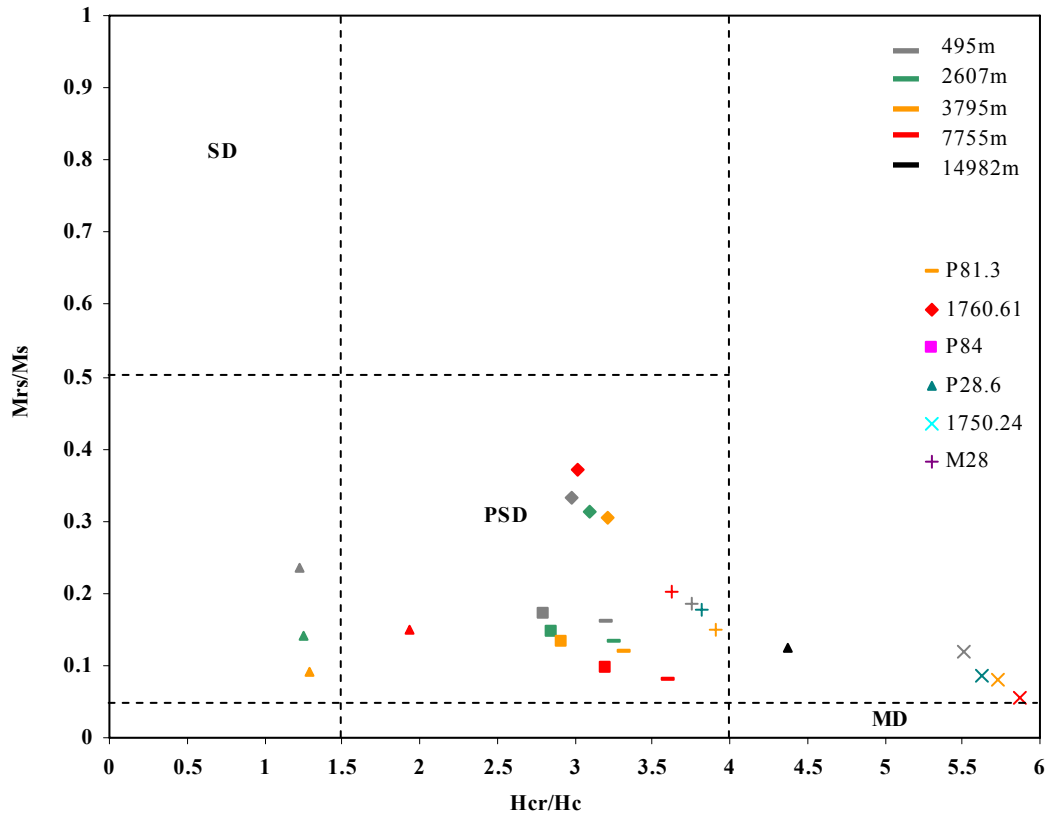

Figure 5.28: Coercivity ratio Hcr/Hc versus remanence ratio Mrs/Ms for respective temperature intervals for shoreface samples P81.3, P84, P28.6, HPHT sample M28, and turbidite samples 1750.24, 1760.61. Each sample is represented by a unique symbol and the various temperature intervals are represented by using different colour codes (blue colour corresponding to depth 14982m is only shown for sample P28.6 to indicate the formation of a new ferromagnetic component).

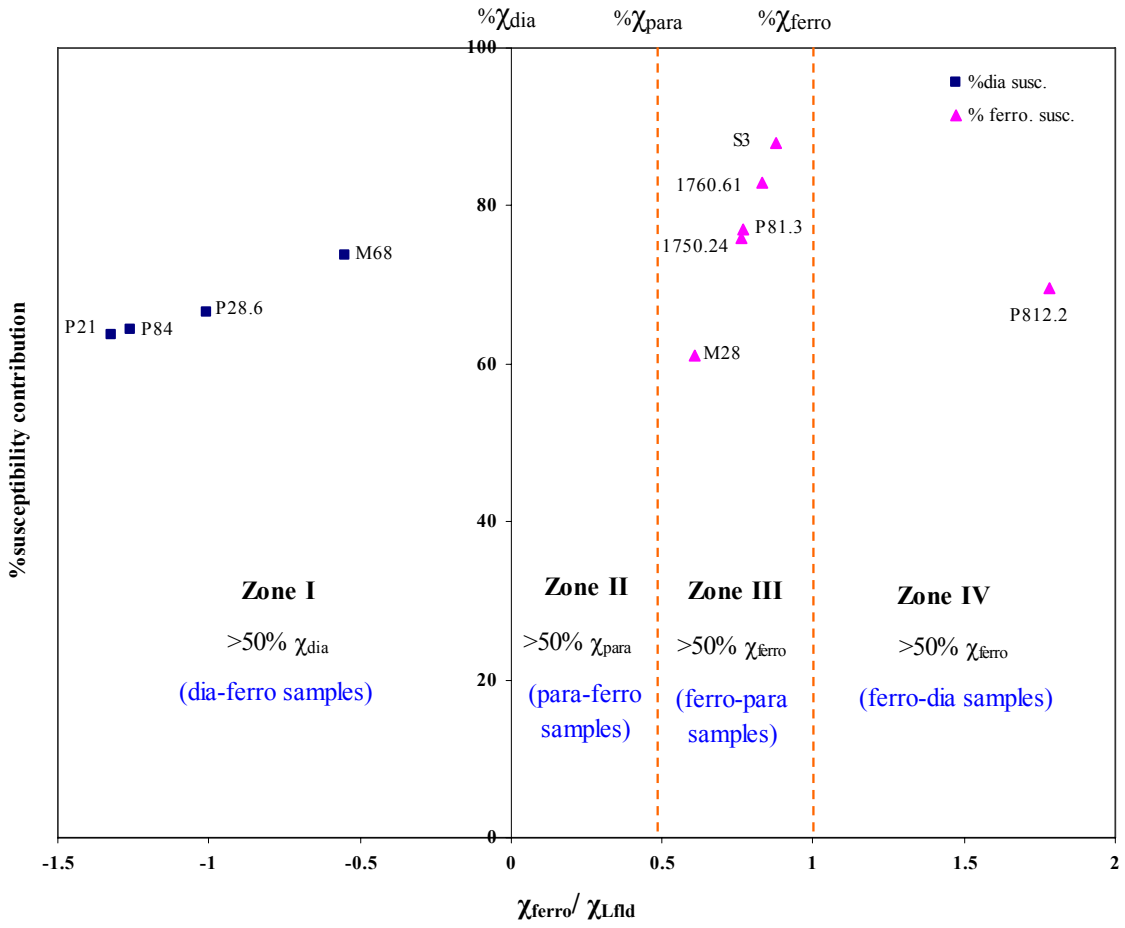

Figure 5.29: Relative susceptibility contribution (in percent) of individual minerals (diamagnetic, paramagnetic, ferromagnetic) towards total magnetic susceptibility (χ_{Lfld}) signal for all the studied reservoir samples. The samples are placed into four zones (I, II, III, IV) depending on the type of mineral that contributes the most towards low field (or total) magnetic susceptibility.

Chapter 6

Conclusions, Summary of Innovative Aspects and Recommendations

In this thesis, I have carried out system modelling and testing of a prototype magnetic susceptibility sonde capable of taking measurements in-situ downhole. The prototype was initially run on laboratory based model boreholes containing layers of different mineral mixtures (simulating different reservoirs). The effect of temperature on various reservoir rock samples was also analysed to model the effect of in-situ reservoir conditions on the magnetic susceptibility signal. This chapter summarises the main conclusions arising from this work, outlines the main innovations, and suggests recommendations for future work.

6.1 Conclusions

6.1.1 System modelling and testing of a magnetic susceptibility sonde system

The prototype magnetic susceptibility sonde system induces a time-varying magnetic field (also called primary magnetic field) into the formation material. The strength of the generated magnetic field is increased in the presence of paramagnetic/ferromagnetic minerals and is decreased in the presence of diamagnetic minerals. The resulting magnetic field at the pick up coil determines the magnetic susceptibility of the formation material, and to some extent identifies the mineralogy as well.

Model boreholes prepared in the laboratory can be used to run the prototype sonde and to process the data output from the sonde. The sonde is more sensitive for smaller diameter boreholes. In such cases, the magnetic susceptibility produced by magnetic minerals present within the formation material can be easily detected by the sonde.

The sonde sensitivity decreases with an increase in borehole diameter. Also, if there is a relatively less concentration of magnetic minerals within the formation material, eddy currents produced due to formation conductivity overcome susceptibility and the sonde shows a negative output. The conductivity of normally encountered borehole fluids will not, however, be sufficiently high to produce this effect.

The sonde presents several advantages over conventional wireline logging tools in terms of resolution, speed of measurement, analysis time etc. It can aid interpretation of image logs and standard wireline gamma ray logs. It also overcomes many limitations the present day logging tools have (summarised in Table 1.1), in particular in shaley formations. If used with the gamma ray tool, the magnetic susceptibility sonde can provide more information on mineral contents and petrophysical parameters. This is achieved by comparing the magnetic susceptibility signal with the data from gamma ray tool.

The sonde can operate at oil or gas reservoir temperatures (up to at least 110 °C) and pressures of around 6000-10000 psi (about 40-70 MPa). Since the laboratory based magnetic susceptibility measurements by other authors have shown strong correlations with fluid permeability, Q_v, and the flow zone indicator (FZI), this makes downhole in-situ measurements of magnetic susceptibility a strong candidate to become a routine part of a wireline logging string. It might also be incorporated in another form of downhole measurements, these being measurements while drilling (MWD) or logging while drilling (LWD).

6.1.2 Temperature dependence of the magnetic susceptibility of reservoir rocks

Increase in temperature causes the magnetic ordering of paramagnetic material to become more chaotic, leading to a slight decrease in χ_{Lfld} due to χ_{para} being reduced to some extent. This can be seen in Figure 5.13 where χ_{Lfld} is bigger than χ_{ferro} and χ_{Lfld} at low temperatures and less at higher temperatures.

Pure diamagnetic minerals exhibit a magnetic susceptibility that is independent of temperature (and therefore independent of depth in the reservoir). The fact that experimentally some predominantly “diamagnetic” reservoir samples (P84, P28.6) showed slight decreases in χ_{dia} with increasing temperature (Figure 5.16) suggested that there were small amounts of paramagnetic minerals in the samples.

Magnetic hysteresis measurements conducted at various temperatures can be used to identify relative concentrations and changes in magnetic mineralogies (para, dia and ferro). A greater decrease in high field slope with temperature would mean the presence of a higher amount of paramagnetic component in the sample. This is consistent with observations of decreases in χ_{para} for reservoir samples S3 and 1760.61 (Figure 5.14)

having an intrinsically higher paramagnetic content compared to the ferromagnetic content.

Subtracting the paramagnetic/diamagnetic component from the hysteresis loops, the resultant ferromagnetic hysteresis loops are indicative of the ferromagnetic concentration in the sample. The temperature analyses of ferromagnetic hysteresis loops provide information on the stability of the ferromagnetic component. From this, one can infer whether the sample is likely to undergo chemical changes at in-situ reservoir conditions. Information like saturation magnetisation, domain state and percent contribution of ferromagnetic minerals towards total susceptibility (χ_{Lfld}) is obtained from the ferromagnetic hysteresis loops.

Some idea of the domain state, single-domain (SD) or multidomain (MD), of the ferromagnetic carriers in the reservoir samples can be obtained by plotting relevant hysteresis parameters (Hcr/Hc versus Mrs/Ms) on a Day plot. Changes in the domain state with increasing temperatures were observed which either resulted from the formation of new ferromagnetic components and/or variations in grain size. For example, the shoreface sample P28.6 (Figure 5.28) plot in the SD region at room temperature. As the temperature was increased significantly, the sample shifts towards the pseudo-single-domain (PSD) and multidomain (MD) regions. This shift is due to the growth of newly formed MD magnetite which was also shown in Figure 5.20. Note, however, that for sample P28.6 the in-situ reservoir temperature (around 131 ^{o}C) is unlikely to cause significant changes in the domain state of the ferromagnetic component compared to room temperature conditions.

Dividing the susceptibility of the ferromagnetic component (χ_{ferro}) by the low field susceptibility (χ_{Lfld}) for any reservoir sample and plotting it against the percent susceptibility contribution of the dominant susceptibility carrying mineral, one can easily make interpretations about the magnetic nature of the matrix and other components within the sample. One can also determine the percent contribution each component brings to the total or low field magnetic susceptibility.

6.2 Summary of innovative aspects

This thesis had the following innovative aspects:

- Modelling the behaviour of the magnetic susceptibility of reservoir rocks at reservoir temperatures.

- Establishing a link between the temperature analyses of ferromagnetic hysteresis loops and the stability of their ferromagnetic components.

- Using magnetic hysteresis measurements conducted at various temperatures to identify relative concentrations of paramagnetic, diamagnetic and ferromagnetic minerals.

- Using the temperature dependent susceptibility (TDS) curves to identify the type of magnetic minerals present, their relative concentrations, phase transitions and changes in mineralogy.

- Establishing a link between changes in the domain state with an increase in temperature which either resulted from the formation of new ferromagnetic components and/or variations in grain size.

- System modelling and testing of a prototype magnetic susceptibility sonde capable of taking magnetic susceptibility measurements downhole.

- Testing a new sonde which has a potential to become a routine part of a wireline logging string. This sonde provides a decent upgrade over conventional logging tools in terms of its resolution, speed of measurement, analysis time etc. It can potentially save a huge amount of time and money to the oil and gas companies/operators.

6.3 Recommendations for future work

The following represent a (non-exhaustive) list of recommendations for further work:

- Increase the diameter of the prototype magnetic susceptibility sonde so that it can operate in larger diameter boreholes. The number of turns on the coils, their length and spacing should also be adjusted accordingly such that the sensitivity of the sonde doesn't deteriorate with an increase in its diameter.

- See the effect of a variation in the operating frequency of the sonde on its sensitivity. At the moment I have kept the operating frequency quite low such that the formation conductivity effects do not overcome the magnetic susceptibility. In real time logging runs and for larger diameter boreholes, the operating frequency would need readjustment.

- The logging runs of the sonde should be extended from laboratory based model boreholes to standard industry diameter boreholes. These real time logging runs should be carried out by initially running the sonde individually, and later as part of a wireline logging string.

- When run in real time conditions, the in-situ magnetic susceptibility data from the sonde should be compared with the laboratory based temperature dependent susceptibility (TDS) curves for the extracted plugs at the same depth, and comment if there are any differences. This would help in calibrating laboratory based thermomagnetic analyses on reservoir rocks to real time downhole measurements.

- Compile a comprehensive series of TDS curves for different mineral types and/or combinations of different reservoir minerals. These would become type curves for rapidly identifying and quantifying multiple mineralogies in real reservoir samples by just comparing their TDS measurements with the template curves.

- Study the variations in anisotropic magnetic properties of reservoir rocks, particularly anisotropy of magnetic susceptibility (AMS), at various reservoir temperatures in order to correlate with and ultimately predict other anisotropic petrophysical properties (such as permeability anisotropy). A change in AMS with temperature may correspond to a change in permeability anisotropy.

References

[1] http://projects.bre.co.uk/condiv/stonelist/stonelist.html#Anchor-c

Argyle, K. S., Dunlop, D. J., 1984. Theoretical domain structure in multidomain magnetite particles. Geophysical Research Letters, 11, 185-188.

Argyle, K. S., Dunlop, D. J., 1990. Low-temperature and high-temperature hysteresis of small multidomain magnetites (215–540 nm), J. Geophys. Res., 95(B5), 7069–7082.

Bagin, V. I., Ismail-zade, T. A., Malumyan, L. M., Pecherskiy, D. M., 1973. Magnetic studies of the sedimentary rocks of the productive formation in Azerbaijan. [Russian] [Magnitnye issledovaniya osadochnykh porod produktivnoy tolshchi Azerbaijana]. Proceedings of the IX conference: Problems of permanent geomagnetic field, magnetism of rocks and paleomagnetism. Part 2. Baku.

Bagin, V. I., Malumyan, L. M., 1976. Iron-containing minerals in oil-impregnated sedimentary rocks from a producing rock formation of Azerbaijan. [Russian] [Zhelezo-soderzhashchie mineraly v propitannykh neft'yu osadochnykh porodakh produktivnoy tolshchi Azerbaijana]. Proceedings of Academy of Sciences of the USSR. Physics of the Earth [Izvestiya Akademii Nauk SSSR. Fizika Zemli], 4, 73-79. English print.

Bagin, V. I., Malumyan, L. M., 1976. Iron-containing minerals in oil-impregnated sedimentary rocks from a producing rock mass of Azerbaidzhan. Translated from Russian by Georgia Moritz. Izvestiya Akademii Nauk SSSR. Fizika Zemli, 4, 273-277.

Bando, Y., Kiyama, M., Yamamoto, N., Takada, T., Shinjo, T., Takaki, H., 1965. Magnetic properties of Fe_2O_3 fine particles. Journal of the Physical Society of Japan, 20,2086.

Banerjee, S. K., 1971. New grain size limits for paleomagnetic stability in hematite. Nature, 232, 15-16.

Beget, J. E., Stone, D. B., Hawkins, D. B., 1990. Paleoclimatic forcing of magnetic susceptibility variations in Alaskan loess during the late Quaternary. Geology 18, 40–43.

Biot, M. A., 1962. Mechanics of deformation and acoustic propagation in porous media, J. Applied Physics, 33, 1482-1498.

Bleil, U., Petersen, N., 1982. Magnetic properties of rocks, in Landolt-Boernstein Numerical Data and Functional Relationships in Science and Technology (K.-H. Hellwege, eds.); New Series; Group V: Geophysical and Space Research, Vol. 1B, Physical Properties of Rocks, edited by G. Angenheister, Springer-Verlag Berlin, Heidelberg, New York, 308-432.

Borradaile, G.J., 1987. Anisotropy of magnetic susceptibility: rock composition versus strain. Tectonophysics 138, pp. 327-329.

Borradaile, G.J., 1988. Magnetic susceptibility, petrofabrics and strain. Tectonophysics 156, pp. 1–20

Borradaile, G. J., MacKenzie, A., Jensen E., 1990. Silicate versus trace mineral susceptibility in metamorphic rocks. Journal of Geophysical Research, Solid Earth, 95, 8447-8451.

Brace, W. F., 1965. Some new measurements of linear compressibility of rocks, J. Geophysics Res., 70, 391-398.

Butler, R. F., 1992. Paleomagnetism: Magnetic domains to geologic terranes. Originally published by Blackwell Scientific Publications, 234 pp..

Butler, R. F., Banerjee, S. K., 1975. Theoretical single-domain grain size range in magnetite and titanomagnetite. Journal of Geophysical Research, 80 (29). 4049-4058.

Carmichael, R. S., 1982. Practical Handbook of Physical Properties of Rocks, vol. II, CRC Press, Boca Raton, Fla.

Carmichael, R. S., eds., 1989. Practical handbook of physical properties of rocks and minerals. CRC Press, Boca Raton, 741 pp.

Cavanough, G. L., Holtham, P. N., 2001. Online measurement of magnetic susceptibility in titanium minerals processing. The AusIMM Proceedings 306 (2), 1–6.

Cavanough, G. L., Holtham, P. N., 2004. Rapid characterisation of magnetic separator feed stocks in titanium minerals processing, Physical Separation in Science and Engineering 13(3–4), Taylor & Francis, 141–152.

Cioppa, M. T., Al-Aasm, I. S., Symons, D. T. A., 2001. Paleomagnetic dating of diagenetic events in Paleozoic carbonate reservoirs of the Western Canada Sedimentary Basin. Conference of Rock the Foundation Convention, 18-22.

Cogoini, M., 1998. Determining the origin of soil magnetic susceptibility anomalies in hydrocarbon environments. AAPG Bulletin 11, 2160-2161.

Collinson, D. W., 1983. Methods in rock magnetism and paleomagnetism: Techniques and Instrumentation. Chapman and Hall, London, 503 pp.

Cooke, M. P., De Sa, A., 1981. A radio frequency method for the measurement of initial magnetic susceptibility, J. Phys. E: Sci. Instrum. 14 1192–1195.

Costanzo-Alvarez, V., Aldana, M., Aristeguieta, O., Marcano, M. C., Aconcha, E., 2000. Study of magnetic contrasts in the Guafita oil field (South-Western Venezuela). Physics and Chemistry of the Earth, Part A-Solid Earth and Geodesy, 25 (5), 437-445.

Cui, Y., Verosub, K. L., Roberts, A. P., 1994. The effect of low-temperature oxidation on large multi-domain magnetite, Geophys. Res. Lett., 21:757.

David, A. E., James, W. A., Ronald, B. C, 1981. The DOE/Simplec magnetic susceptibility logging system. SPWLA 22nd annual logging symposium, June 23-26.

Day, R., Fuller, M., Schmidt, V. A., 1977. Hysteresis properties of titanomagnetites: Grain-size and compositional dependence. Physics of the Earth and Planetary Interiors, 13, 260-267.

Dearing, J. A., 1999. Environmental magnetic susceptibility using the Bartington MS2 system.

Deer, W.A., Howie, R.A., Zussman, J., 1992. An introduction to the rock forming minerals, 2nd Ed. Longman Group UK Limited.

Donovan, T. J., Forgey, R. L., Roberts, A. A., 1979. Aeromagnetic detection of diagenetic magnetite over oil fields. AAPG Bulletin, 63, 245-248.

Dortman, N. B., 1976. Physical properties of rocks and minerals. [Russian]. Nedra, Moscow.

Drobace, D., Maronic, Z., 1999. Multipurpose measuring device based on AC susceptometer, Fizika A (Zagreb) 8 165–172.

Dunlop, D. J., 1973a. Superparamagnetic and single-domain threshold sizes in magnetite. Journal of Geophysical Research, 78, 1780-1793.

Dunlop, D. J., 1973b. Thermoremanent magnetization in submicroscopic magnetite. Journal of Geophysical Research, 78, 7602-7613.

Dunlop, D. J., 1981. The rock-magnetism of fine particles. Phys. Earth Planet. Inter. 26, 1–26.

Dunlop, D. J., 2002. Theory and application pf the Day plot (Mrs/Ms versus Hcr/Hc). Application to data for rocks, sediments, and soils. Journal of Geophysical Research, 107 (B3) doi:10.1029/2001JB000486.

Dunlop, D. J., Bina, M. M., 1977. The coercive force spectrum of magnetite at high temperatures: Evidence for thermal activation below the blocking temperature. Geophysical Journal of the Royal Astronomical Society, 51, 121-147.

Dunlop, D. J., Ozdemir, O., 1997. Rock magnetism: Fundamentals and frontiers. Cambridge University Press, Cambridge, 573 pp.

Enkin, R. J., Williams, W., 1994. Three-dimensional micromagnetic analysis of stability in fine magnetic grains. Journal of Geophysical Research, 99, 611-618.

Ergin, Y. V., 1983. Magnetic properties and structure of electrolyte solutions. [Russian], Nauka, Moscow, 183 pp.

Ergin, Y. V., Kostrova L. I., Subaev I. Kh., and Yarulin K. S., 1975. Magnetic properties of oils. [Russian]. Depositor of VINITI, N3265-75.

Ergin, Y. V., Yarulin, K. S., 1979. Magnetic properties of oils. [Russian], Nauka, Moscow, 200 pp.

Eventov, L., 1997. Application of magnetic methods in oil and gas exploration. The Leading Edge, 16 (5), 489-492.

Eventov, L., 2000. The nature and interpretation of geophysical and geochemical anomalies over oil and gas fields. The Leading Edge, 19 (5), 488-490.

Filippycheva, L. G., Burakov, A. I., Bogdanovich, A. I., Belyaev, I. P., Gutner, A. B., 2001. Downhole magnetic stratigraphy in solving problems of correlation of heterofacial strata, sequence-stratigraphy for oil fields modelling, technology of operations, instrumentation [CD Rom]. EAGE 63th Conference and Technical Exhibition, Amsterdam, 11-15 June, 643 pp.

Foex, G., Gorter, C. J., Smits, L. J., 1957. Constantes selectionees: Diamagnetisme et paramagtitisme; relaxation paramagnetique. [French], Union Internationale de Chimie, Vol. 7, Masson and Cie, Paris, 317 pp.

Foner, S., 1991. Review of magnetometry, IEEE Trans. Magn. 17 (6) 3358–3363.

Foner, S., McNiff E. J. Jr., 1968. Very low frequency integrating vibrating sample magnetometer (VLFVSM) with high differential sensitivity in high dc fields, Rev. Sci. Instrum. 39 171–179.

Fraser, D.C., 1973, Magnetite ore tonnage estimates from an aerial electromagnetic survey: Geoexploration, 11, 97-105.

Geiss, C. E., 1999. The development of rock magnetic proxies for paleoclimate reconstruction. Thesis, University of Minnesota, 254 pp.

Geiss, C. E., Heider, F., Soffel, H. C, 1996. Magnetic domain observations on magnetite and titanomaghemite grains (0.5 - 10 μm). Geophysical Journal International, 124, 75 – 88.

Gillen, K. P., Van der Voo, R., Thiessen, J. H., 1999. Late Cretaceous-early Tertiary remagnetization of the devonian Swan Hills Formation recorded in carbonate cores from the Caroline gas field, Alberta, Canada. AAPG Bulletin, 83 (8), 1223-1235.

Hailwood, E. A., Ding, F., 1995. Paleomagnetic reorientation of cores and the magnetic fabric of hydrocarbon reservoir sands. In: P. Turner and A. Turner, eds., Paleomagnetic application in hydrocarbon exploration and production. Geological Society Special Publication 98, 245-258.

Hall, S. A., Evans, I., 1995. Paleomagnetic and magnetic properties of hydrocarbon reservoir from the Permian basin, southeastern New Mexico, USA. In: P. Turner and A. Turner, eds. Paleomagnetic application in hydrocarbon exploration and production. Geological Society Special Publication 98, London, 79-95.

Hanson, L. S., Sauchuk, S. A., 1991, Field guide to the geology and geomorphology of the Carrabassett Formation and economic deposits in central Maine, in Fieldtrip Guide for the Summer Meeting of the Geological Society of Maine, 42 p.

Henry, B., Jordanova, N., Le Goff, M., 2005. Transformations of magnetic mineralogy in rocks revealed by difference of hysteresis loops measured after stepwise heating: theory and case studies: Geophysical Journal International, Vol. 162, 64-78.

Hill, R., 1963. Elastic properties of reinforced solids: Some theoretical principles, J. Mech. Physics. Solids, 11, 357-372.

Hill, R. W., 1982. Advanced student experiments in paramagnetism and antiferromagnetism, Eur. J. Phys., 3, 75-79.

Hoffmann, V., 1992. Greigite (Fe_3S_4): magnetic properties and first domain observations. Physics of the Earth and Planetary Interiors, 70, 288-301.

Hrouda, F., 1973. A determination of the symmetry of the ferromagnetic mineral fabric in rocks on the basis of the magnetic susceptibility anisotropy measurements. Gerl. Beitr. Geophys., 82, 390-396.

Hrouda, F., 1994. A technique for the measurement of thermal changes of magnetic susceptibility of weakly magnetic rocks by the CS-2 apparatus and KLY-2 Kappabridge. Geophys. J. Int., 118, 604-612.

Hrouda, F., 2002. Low-field variation of magnetic susceptibility and its effect on the anisotropy of magnetic susceptibility of rocks. Geophys. J. Int., 150, 1-9.

Hrouda, F., 2003. Indices for numerical characterization of the alteration processes of magnetic minerals taking place during investigation of temperature variation of magnetic susceptibility. Stud. Geophys. Geod., 47, 847-861.

Hunt, C. P., Moskowitz, B. M., Banerjee, S. K, 1995. Rock physics and phase relations: a handbook of physical constants. AGU Reference Shelf 3. Magnetic Properties of Rocks and Minerals, 189-203.

Isokangas, E.A., 1996. Aspects of process control in mineral sands dry plant, PhD thesis in Department of Mining and Metallurgical Engineering, University of Queensland, Brisbane.

Ivakhnenko, O.P., Potter, D.K., 2006. The use of magnetic hysteresis and remanence measurements in rapidly and nondestructively characterising reservoir rocks and fluids. Society of Core Analysts held in Trondheim, Norway 12-16.

Ivakhnenko, O.P., Potter, D.K., 2008. The use of magnetic hysteresis and remanence measurements for rapidly and non-destructively characterizing reservoir rocks and fluids. Journal of Petrophysics, 49 (1), 47-56.

Jackson, M., Worm, H. U., Banerjee, S. K., 1990. Fourier analysis of digital hysteresis data: Rock magnetic applications, Phys. Earth Planet. Int., 65-78.

Jeffrey, E. L., William, H. L., Karl, J. E., 2007. An Introduction to Using Surface Geophysics to Characterize Sand and Gravel Deposits. U.S. Geological Survey, Reston, Virginia.

Kapička, A., Hoffmann, V., Petrovsky, E., 2003. Pressure instability of magnetic susceptibility of pyrrhotite bearing rocks from the KTB borehole. Studia Geophysica et Geodaetica, 47 (2), 381-391.

Kelso, P., Tikoff, B., Jackson, M., Sun, W., 2002. A new method for the separation of paramagnetic and ferromagnetic susceptibility anisotropy using low-field and high-field methods, Geophysical Journal International 151, 345–359.

Kennedy, T., 1985. Long range order in the anisotropic quantum ferromagnetic Heisenberg model, Commun. Math. Phys. (100) pp 447.

Kittel, C., 1949. Physical theory of ferromagnetic domains. Reviews of Modern Physics, 21 (4), 541–583.

Kittel, C., 1996. Introduction to solid state physics, 7th edition, John Wiley.

Langevin, P., 1905. La physique des electrons. Revue générale des sciences pures et appliqués. [French], 16, 257–276.

Leonardon, E.G., 1961. Logging, Sampling and Testing. History of Petroleum Engineering, API, New York City 495 pp.

Lewis, R. T., Foner, S., 1976. Letters to the editor: 1. Sensitivity of two magnetometers 2. Comments on Lewis's letter: "Sensitivity of two magnetometers", Rev. Sci. Instrum. 47, 519–522.

Liu, Q.H., Chew, W.C., Taherian, M.R., Safinya, K.A., 1989. A modelling study of electromagnetic propagation tool in complicated borehole environments. Log. Anal., 30(1) 424-436.

Liu, Q. S., Liu, S. G., 1999. Magnetic and mineralogical characteristics of reservoir rocks in the Yakela oil field, northern Tarim Basin and their implications for magnetic detection of oil and gas accumulations. Chinese Science Bulletin, 44 (2), 174-177.

Liu, Q. S., Xu, W. K., Deing, S. F., Wang, X. F., 1996. A study for relationship between hydrocarbon migration and soil magnetism above oil and gas fields in China. Acta Geophysica Sinica, 39 (6), 804-812.

Liu, Q., Banerjee, S. K., Jackson, M. J., Zhu, R., Pan, Y., 2002. Effects of low-temperature oxidation on natural remanent magnetization of Chinese loess. Chinese science bulletin, 47 (24), 2100-2105.

Matteson, A., Tomanic, J. P., Herron, M. M., Allen, D. F., Kenyon, W. E., 2000. NMR relaxation of clay/brine mixtures. SPE Reservoir Evaluation and Engineering, 3 (5), 408-413.

Mayer-Gurr A., 1976. Petroleum Engineering. Geology of Petroleum. Vol. 3, Pitman Publishing, 208 pp.

McAndrew, J., 1957. Calibration of a Frantz isodynamic separator and its application to mineral separation, Proc. Aus. IMM 181 59–73.

McNab, T. K., Fox, R. A., Boyle, A. J. F, 1968. Some magnetic properties of magnetite (Fe3O4) crystals. Journal of Applied Physics, 39, 5703-5711.

Mee, C., Daniel, E., 1988. Magnetic recording, Vol - III, McGraw Hill.

Melnikov, N. W., Rshewski, W. W., Prodotjakonov, M. M, 1975. Handbook of physical properties of rocks. Nedra, Moscow.

Merrill, R. T., McElhinny, M., McFadden, P., 1996. The magnetic field of the Earth: Paleomagnetism, the Core and the Deep Mantle. Academic Press.

Moskowitz, B. M., 1980. Theoretical grain size limits for single-domain, pseudo-single-domain and multi-domain behaviour in titanomagnetite (x = 0.6) as a function of low-temperature oxidation, Earth Planet. Sci. Lett., 47:285.

Moskowitz, B. M., 1991. Hitchhiker's guide to magnetism. Institute of Rock Magnetism, Environmental Magnetism Workshop, 48 pp.

Moskowitz, B. M., Frankel, R. B., Walton, S. A., Dickson, D. P. E., Wong, K. K. W., Douglas, T., Mann, S., 1997. Determination of the preexponential frequency factor for superparamagnetic maghemite particles in magnetoferritin. Journal of Geophysical Research, 102, 22671-22680.

Mullins, C. E., 1977. Magnetic susceptibility of the soil and its significance to soil science: a review. Journal Soil Science, 28, 233-246.

Nesset, E., Finch, J. E., 1980. Determination of magnetic parameters for field-dependent susceptibility minerals by Frantz isodynamic magnetic separator, Trans. IMM Sect. C 89 161–166.

Spaldin, N.A., 2003. Magnetic materials: fundamentals and device applications. Cambridge University press. 37 pp.

O'Reilly, W., 1984. Rock and mineral magnetism. Blackie, Glasgow, 220 pp.

Parasnis, D. S., 1979. Principles of Applied Geophysics. 3rd eds., Chapman and Hall, London, 275 pp.

Petersen, E. U., Friesen, R. G. 1982. Metamorphism of the Geco massive sulphide deposit, Manitouwadge, Ontario. Geol. Assoc. Can./Mnieral. Assoc. Can. Program Abstr. 7, 73.

Petersen, N., 1985. Gesteinsmagnetismus. In: F. Bender, eds., Angewandte Geowissenschaften. [German], Vol. 2, Ferd. Enke Verlag, Stuttgart.

Petty, M.C., 2007. Molecular electronics: From principles to practice (Wiley series in materials for electronic and optoelectronic applications). WileyBlackwell, 208 pp.

Potter, D. K., 2004a. Magnetic susceptibility as a rapid petrophysical tool for a permeability prediction. EAGE 66th Conference and Technical Exhibition, Paris, 7-10 June 2004. Extended Abstracts, Vol. 1, Paper D018.

Potter, D. K., 2004b. Downhole magnetic susceptibility: potential applications of an environmentally friendly technique. European Geosciences Union, 1st General Assembly, Nice, France, 25-30 April. Geophysical Research Abstracts, 6, 04935.

Potter, D. K., Corbett, P. W. M., Barclay, S. A., Haszeldine, R. S, 2004. Quantification of illite content in sedimentary rocks using magnetic susceptibility - A rapid complement or alternative to X-ray diffraction. Journal of Sedimentary Research, 74 (5), 730-735.

Potter, D. K., 2005. Magnetic susceptibility as a rapid non-destructive technique for improved RCAL and SCAL parameter prediction. 2005 International Symposium of the Society of Core Analysts, Toronto, Canada. Paper SCA2005-02, 13 pp.

Potter, D. K., 2007. Magnetic susceptibility as a rapid, non-destructive technique for improved petrophysical parameter prediction. Journal of Petrophysics, 48 (3), 191-201.

Potter, D.K., Ivakhnenko, O.P., 2008. Clay typing - Sensitive quantification and anisotropy in synthetic and natural reservoir samples using low- and high-field magnetic susceptibility for improved petrophysical appraisals. Journal of Petrophysics, 49 (1), 57-66.

Richter, C., van der Pluijm, B.A., 1994. Separation of paramagnetic and ferromagnetic susceptibilities using low temperature magnetic susceptibilities and comparison with high field methods, Physics of the Earth and Planetary Interiors, 82, 113-123.

Robin, P., Bordas le Floch, N., Roure, F., Frizon, de Lamotte, D., 2000. Magnetic fabric analysis and deformation in sandstone reservoir. Geophysical Research Abstracts, Vol. 2.

Rosenblum, S., Brownfield, K., 1999. Magnetic susceptibility of minerals. USGS open-file report 99-529. [On-line] http://pubs.usgs.gov.

Selwood, P. W., 1956. Magnetochemistry. 2nd edition. Interscience publishers, New York, 435 pp.

Sepulveda, N., Thomas, I., Wikswo, J., 1994. Magnetic susceptibility tomography for a three dimensional imaging of diamagnetic and paramagnetic objects, IEEE Trans. Magn. 30 5062–5069.

Sharma, P. V., 1986. Geophysical Methods in Geology. 2nd edition, Elsevier, New York, 442 pp.

Soffel, H. C., 1971. The singledomain-multidomain transition in natural intermediate titanomagnetites. Zeitschrift fuer Geophysik, 37, 451-470.

Soffel, H. C., 1977. Pseudo-single-domain effects and single-domain - multidomain transition in natural pyrrhotite deduced from domain structure observations. Journal of Geophysics, 42, 351-359.

Soffel, H. C., 1991. Paläomagnetismus und archäomagnetismus. [German], Springer, Berlin, Heidelberg, 276 pp.

Stephenson, A., De Sa, A., 1970. A simple method for the measurement of the temperature variation of initial magnetic susceptibility between 77 and 1000 K, J. Phys. E 3 59–61.

Stradling, A, 1991. Mathematical models of dry high-intensity magnetic separators, PhD thesis in Department of Mineral and Metallurgical Engineering, University of Queensland, Brisbane.

Symons, D. T. A., Enkin, R. J., Cioppa, M. T., 1999. Paleomagnetism in the Western Canada Sedimentary Basin: Dating fluid flow and deformation events. Bulletin of Canadian Petroleum Geology, 47 (4), 534-547.

Syngaevsky, P., 2000. Shaly Sand Models: a Review. Louisiana State University.

Tarling, D. H., 1983. Palaeomagnetism: principles and applications in geology, geophysics and archaeology. Chapman and Hall Ltd., London, 379 pp.

Tarling, D. H., Hrouda, F., 1993. The magnetic anisotropy of rocks. Chapman and Hall, London, 217 pp.

Tauxe, L., 1993. Sedimentary records of relative palaeointensity of the Geomagnetic field: Theory and Practice. Reviews of Geophysics, 31 (3), 319-354.

Telford, W. M., Geldart, L. P., Sheriff, R. E., 1990. Applied Geophysics. 2nd eds., Cambridge University Press, New York, 770 pp.

Thompson, R., Oldfield, F., 1986. Environment magnetism. Allen and Unwin, 227 pp.

Torquato, S., 1991. Random heterogeneous media: Microstructure and improved ounds on effective properties, Applied Mech. Rev., 44, 37-76.

Vasudeva, D. N., 1966. Fundamentals of Magnetism and Electricity, 7th edition, S.Chand and Co., 443-448.

Vulfson, S. G., 1998. Molecular magnetochemistry. Overseas Publishers Association, Amsterdam. Originally published in Russian in 1991. Nauka Publisher. Moscow. 474 pp.

Watt, J. P., 1988. Elastic properties of polycrystalline minerals: Comparison of theory and experiment, Phys. Chem. Minerals, 15, 579-587.

Wilson, H., Brooks, A. G., 2001. Wellbore position errors caused by drilling fluid contamination. SPE Publication 71400, 8 pp.

Wyllie, M. R. J., Gregory, A. R., Gardner, G. H. F., 1958. An experimental investigation of factors affecting elastic wave velocities in porous media, Geophysics, 23, 459-493.

Yeremin, V. N., Molostovskiy, E. A., Pervushova, Ye, V., Chernyaeva, A. F., 1986. Magnetic zonation of sedimentary rocks and the spatial distribution of authigenic iron minerals in hydrocarbon halos. [Russian] [Magnitnaya zonal'nost' osadochnykh porod i prostranstvennoye raspredeleniye autigennykh mineralov zheleza v zonakh vliyaniya UV]. Geology of oil and gas [Geologiya Nefti i Gaza], 4, 38-44. English print. Yeremin, V. N., Molostovskiy, E. A., Pervushova, Ye, V., Chernyaeva, A. F., 1986. Magnetic zonation of sedimentary rocks and the spatial distribution of authigenic iron minerals in hydrocarbon halos. International Geology Review, 28, 734-739.